Microwave Breast Imaging Techniques in Two and Three Dimensions

by

Anastasia Baran

A Thesis submitted to the Faculty of Graduate Studies of
The University of Manitoba
in partial fulfilment of the requirements of the degree of
Doctor of Philosophy

Department of Electrical and Computer Engineering
University of Manitoba
Winnipeg, Manitoba, Canada

Abstract

Biomedical imaging at microwave frequencies has shown potential for breast cancer detection and monitoring. The advantages of microwave imaging over current imaging techniques are that it is relatively inexpensive, and uses low-energy, non-ionizing radiation. It also provides a quantitative measurement of the dielectric properties of tissues, which offers the ability to characterize tissue types.

Microwave imaging also comes with significant drawbacks. The resolution is poor compared to other imaging modalities, which presents challenges when trying to resolve fine structures. It is also not very sensitive to low contrast objects, and the accuracy of recovered tissue properties can be poor.

This thesis shows that the use of prior information in microwave imaging inversion algorithms greatly improves the resulting images by minimizing mathematical difficulties in reconstruction that are due to the ill-posed nature of the inverse problem. The focus of this work is to explore novel methods to obtain and use prior information in the microwave breast imaging problem. We make use of finite element contrast source inversion (FEM-CSI) software formulated in two and three dimensions (2D, 3D). This software has the ability to incorporate prior information as an inhomogeneous numerical background medium.

We motivate the usefulness of prior information by developing a simulated annealing technique that segments experimental human forearm images into tissue regions. Tissue types are identified and the resulting map of dielectric properties is used as prior information for the 2D FEM-CSI code. This results in improvements to the reconstructions, demonstrating the ability of prior information to improve breast im-

ages.

We develop a combined microwave tomography/radar algorithm, and demonstrate that it is able to reconstruct images of superior quality, compared to either technique used alone. The algorithm is applied to data from phantoms containing tumours of decreasing size and can accurately monitor the changes.

The combined algorithm is shown to be robust to the choice of immersion medium. This property allows us to design an immersion medium-independent algorithm, in which a numerical background can be used to reduce the contrast. We also develop a novel march-on-background technique that reconstructs high quality images using data collected in multiple immersion media.

Acknowledgements

I would like to thank my academic advisor, Dr. Joe LoVetri, for his guidance and support over the course of my PhD. His honesty, encouragement and work ethic have imparted on me the skills and perseverance necessary to complete this final stage of my graduate education.

Thank you to my co-advisor, Dr. Vladimir Okhmatovski, PhD committee, Drs. Sherif Sherif and Idris Elbakri, and external examiner Dr. Milica Popović.

To my friends and colleagues at the Electromagnetic Imaging Laboratory, Dr. Amer Zakaria, Dr. Mohammad Asefi, Dr. Ian Jeffrey, Dr. Majid OstadRahimi, Kyle Nemez, Cameron Kaye, Pedram Mojabi, Nasim Abdollahi and Gabriel Faucher - thank you for providing an interesting, fun and productive work environment where collaboration and discussion are encouraged.

I would like to acknowledge the guidance and dedication of collaborators Dr. Elise Fear and Dr. Douglas Kurrant at the University of Calgary.

Finally, the continuous support from my parents, Diane and Roman Baran, partner Jason Fiege, and friends, has been paramount in the completion of this work.

This work has largely been made possible by support from The Canadian Breast Cancer Foundation.

Dedicated to Gerald Gale Slusar (Uncle Ger)

February 16, 1940 - December 10, 2014

Contributions

This thesis focuses on the development of microwave breast imaging techniques in two and three dimensions. The work relies heavily on software that implements different versions of a finite element contrast source inversion (FEM-CSI) algorithm, which is not my own. However, my specific contributions to the field presented in this work are as follows:

- The development of a simulated annealing algorithm for microwave imaging, which is designed to detect regional information in blind microwave tomography reconstructions. These regions are incorporated into FEM-CSI as prior information and are used to improve the reconstructed images. The contribution focuses on experimental forearm images, but the algorithm can also be applied to any blind reconstruction as long as the user has basic knowledge of the structure being imaged.

- The development of a novel combined radar-microwave tomography (MWT) algorithm for breast cancer imaging. This algorithm was tested using realistic 2D numerical breast phantoms. The combined algorithm significantly improves reconstructions compared to standard CSI.

- The extension of the combined method to 3D MRI-based phantoms and the use of 3D FEM-CSI on high contrast numerical breast phantoms. Results show an enhanced ability to detect tumours when using the combined method.

- An analysis of the effect of different types of prior information on 2D and 3D breast reconstructions.

- The application of the combined radar-MWT imaging algorithm to tumour size monitoring during cancer treatment. Results demonstrate the algorithms ability to accurately detect changes over time.

- The development and demonstration of a novel technique for 2D immersion medium independent microwave imaging.

- The development of a novel march-on-background technique, which uses data collected in multiple immersion media to reconstruct a single object of interest.

- The introduction of FEM-CSI as a tool for microwave imaging using electric and magnetic contrast sources. The algorithm's unique inhomogeneous background feature is ideal for this application, as it can utilize data collected before and after the injection of contrast agents. *As this thread of research is tangential to the main theme of this thesis, it has been included as an appendix for the reader's interest.*

Table of Contents

List of Tables

List of Figures

Notations, Symbols and Acronyms

Symbol	Description (quantities are unitless unless otherwise stated)
$\hat{x}, \hat{y}, \hat{z}$	unit vectors
$\mathbb{R}$	Set of real numbers
$\mathbb{C}$	Set of complex numbers
∇	Gradient operator
c	Speed of light $(\mathrm{m} \cdot \mathrm{s}^{-1})$
λ	Wavelength (m)
ϵ	Permittivity $(\mathrm{F} \cdot \mathrm{m}^{-1})$
ϵ_b	Relative permittivity of background medium
ϵ_n	Relative permittivity of numerical background
ϵ_r	Relative permittivity
μ	Permeability $(\mathrm{H} \cdot \mathrm{m}^{-1})$
μ_r	Relative permeability
σ	Conductivity $(\mathrm{S} \cdot \mathrm{m}^{-1})$
χ	Contrast
w	Contrast sources $(\mathrm{V} \cdot \mathrm{m}^{-1})$
U	Potential Energy (J)
T	Temperature (K)
s	Covariance
k_{boltz}	Boltzmann's constant $(\mathrm{m}^2 \cdot \mathrm{kg} \cdot \mathrm{s}^{-2} \cdot \mathrm{K}^{-1})$
k_b	Background wave number (m^{-1})
k_n	Numerical background wave number (m^{-1})
σ_{dev}	Standard deviation
E_t^{inc}	Incident electric field $(\mathrm{V} \cdot \mathrm{m}^{-1})$
E_t^{sct}	Scattered electric field $(\mathrm{V} \cdot \mathrm{m}^{-1})$
E_t^{tot}	Total electric field $(\mathrm{V} \cdot \mathrm{m}^{-1})$
f	Frequency (Hz)

Γ	Problem boundary
Ω	Computational domain
$\mathcal{D}$	Imaging domain
$\mathcal{S}$	Measurement surface
$Ł_2$	Vector error norm

Abbreviation	Description
1D	One Dimensional
2D	Two Dimensional
3D	Three Dimensional
ABC	Absorbing Boundary Condition
DBIM	Distorted Born Iterative Method
CSI	Contrast-Source Inversion
CT	Computed Tomography
CTR	Correct Tumour Reconstructed
EIL	Electromagnetic Imaging Laboratory
FDTD	Finite-Difference Time-Domain
FEM	Finite Element Method
FEM-CSI	Finite-Element Contrast-Source Inversion Method
GA	Genetic Algorithms
GHz	Giga Hertz
GNI	Gauss-Newton Inversion
GUI	Graphical User Interface
MR	Multiplicative Regularization
MRI	Magnetic Resonance Imaging
MWI	Microwave Imaging
MWT	Microwave Tomography
OI	Object of Interest
PEC	Perfect Electric Conductor
PSO	Particle Swarm Optimizers
PTR	Proportion of Tumour Reconstructed
SA	Simulated Annealing
SNR	Signal-to-noise ratio
TE	Transverse Electric
TM	Transverse Magnetic
UC	University of Calgary

UM	University of Manitoba
US	Ultrasound
UST	Ultrasound Tomography
UWB	Ultra-wideband

Chapter 1

Introduction

Biological imaging at microwave frequencies has become a prominent research topic because of the ability of microwaves to interrogate biological objects of interest (OI) while posing very little risk to patients [1–4]. Microwaves are low-energy and non-ionizing, making this harmless imaging modality particularly attractive for breast cancer detection and monitoring. Microwave Imaging (MWI) systems can also be built at a fraction of the cost of current imaging systems, and are highly portable. Making MWI commonplace in clinics and hospitals would mean increased comfort for patients, and it could have a particular impact on regions of the world where prohibitively expensive imaging equipment prevents many from receiving adequate care. Breast cancer detection and treatment monitoring has been identified as an important niche for this type of technology [2–18] and will be the main focus of this thesis, but there have also been investigations into imaging extremities (which will be discussed) [19], brain imaging [20], lung cancer diagnosis [21] and cardiac imaging [22]. This thesis will focus mainly on breast cancer imaging using microwave tomography (MWT), but will also discuss combining MWT with microwave radar techniques.

Human tissues exhibit distinct, complex dielectric properties at microwave frequencies. These properties, known as the complex permittivity, are shown for a realistic numerical breast phantom in Figure 1.1, where the colour bar represents the real and imaginary parts of the permittivity of certain tissues. Numerical breast phantoms for MWI algorithm testing are typically derived from a combination of magnetic resonance imaging (MRI) scans that provide the location of the different tissues, and dielectric properties obtained from a large-scale study of breast tissue described in [4]. This study, which measured the properties of freshly excized breast tissue, revealed that the dielectric difference between a malignant tumour and healthy fibroglandular tissue can be less than 10% - making it a challenge to detect tumours at microwave frequencies. In order to take advantage of the aforementioned benefits of MWI, techniques must be developed to detect tumours despite this small difference. Microwave tomography (MWT) is the method of choice when attempting to quantitatively reconstruct the permittivity of breast tissues.

In a typical microwave tomography system, the breast is submerged in an immersion liquid with a known permittivity. This liquid is chosen to maximize interrogation energy into the breast by matching its average permittivity [2], but it can also be used to optimize antenna performance and data collection inside the imaging system by changing the wavelength of the incident radiation. The breast is illuminated with narrow-band energy and data is collected at several receiver locations surrounding the breast. This typical MWT setup is shown for two and three dimensions (2D, 3D) in Figure 1.3. Here the OI represents a breast inside the imaging chamber. In this scenario, we refer to the electric field in the chamber without an OI as the incident field E^{inc}, the field collected at the receiver points when the OI is present as the total field E^{tot} and the scattered field as $E^{sct} = E^{tot} - E^{inc}$.

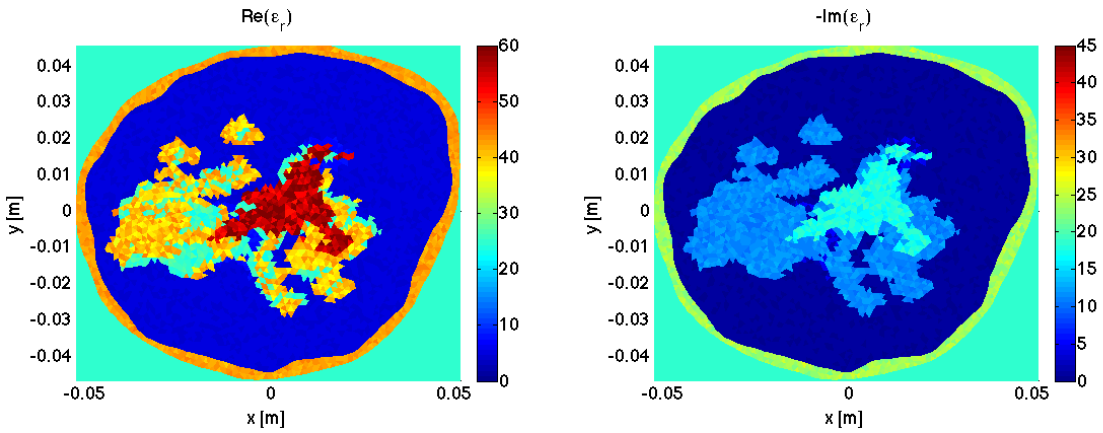

Figure 1.1: Real (left) and imaginary (right) 2D coronal slice of a realistic numerical breast phantom, showing the range of complex dielectric properties in breast tissue at 1GHz. From lowest to highest magnitude, the figure shows fat, fibroglandular, and tumour tissue, with a skin layer around the exterior.

The total field or scattered field at the data points can be used, along with a model of the imaging system, to solve a large non-linear inversion problem and reconstruct a quantitative map of the breast tissues, including any tumours or anomalies. The MWT work herein uses a 2D and 3D finite element contrast source inversion (FEM-CSI) algorithm written by Dr. Amer Zakaria at the Electromagnetic Imaging Laboratory (EIL) at the University of Manitoba (UM) [23]. The finite element formulation of this inversion algorithm makes it particularly useful for modelling the irregular shapes that are often characteristic of biological tissues, as well as any irregular boundaries in the imaging chamber itself. It also allows for non-uniform discretization of the problem, which can be useful when considering the changes in wavelength resolution for tissues with different permittivities. Figure 1.2 shows a FEM discretization of a 2D breast that has been segmented into regions by tissue type. The meshes used in this thesis work were generated by the Gmsh mesh generator [24].

An additional commonly used MWI method is radar-based imaging. Radar-based imaging is a qualitative method used to detect regions of increased scattering due to

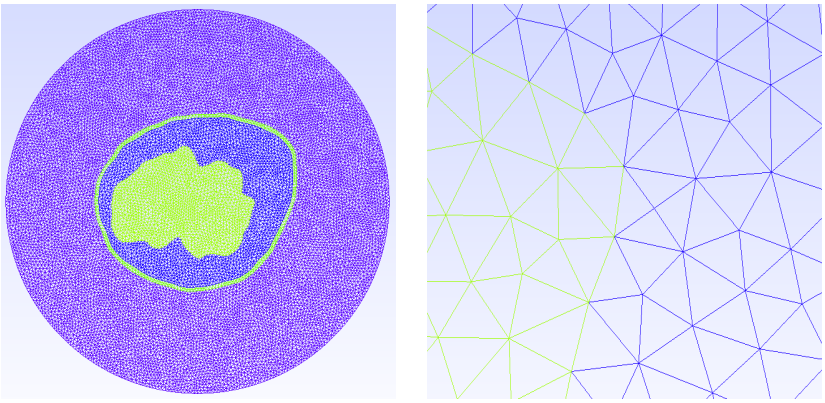

Figure 1.2: 2D finite element mesh used for representing irregular shapes of biological tissues. Right: breast tissue regions represented in the mesh. Left: zoomed in view of the region interface.

abrupt changes in dielectric properties. The transition between normal healthy breast tissue and a malignant tumour would represent such an area. In radar-based imaging the breast is illuminated with a time-domain wide-band pulse. The backscattered field is measured using one or more receivers (monostatic and multistatic) and can be used to determine the location of scatterers. Radar-based imaging is advantageous because of its speed and efficiency. The reconstruction algorithms are not as complicated as in the MWT case as they do not require solving a large inverse problem [25].

Both of these MWI techniques come with some significant drawbacks. There are limitations in the *(i)* resolution of fine structures, *(ii)* sensitivity to small and low contrast objects, and *(iii)* accuracy of recovered tissue properties [7, 25–27]. This thesis outlines techniques that help to overcome these drawbacks in order to take advantage of the benefits of MWI.

1.1 Inverse Scattering in Microwave Tomography

While radar-based imaging is an integral part of this work, MWT will be the primary imaging method used in this thesis. The techniques introduced will help to limit problems that arise due to the complexities introduced by the inverse problem. This inverse scattering problem can be modelled as an optimization problem in which the electrical properties of the breast tissues are the unknowns.

The problem is non-linear and ill-posed, meaning that *(i)* the solution is not unique, in general. The non-uniqueness of the solution arises from the fact that the scattered fields from an object, in this case a breast, are non-linearly related to its dielectric inhomogeneities - making more than one permittivity distribution possible for a given data set. The non-linearity is a result of multiple scattering in the object and is a function of the frequency of the incident field. As frequency increases, or when an dielectric contrast increases, this multiple scattering effect is more pronounced. Also, *(ii)* the solution can be unstable. Instability presents itself as large changes in the reconstructed solution when small changes are made to either the data, or the constraints on the problem. Lack of stability also increases the inversion algorithm's sensitivity to noise in the collected data, and constraints on the problem [28–30].

1.1.1 Finite Element Contrast Source Inversion

In order to find a solution to these non-linear, ill-posed problems, an appropriate inversion algorithm must be used. Our FEM-CSI algorithm features the ability to invert synthetic and measured data for two dimensional transverse magnetic (TM), transverse electric (TE), and full three dimensional cases [23, 31].

When using FEM-CSI, the MWT setup as shown in Figure 1.3 includes the OI being imaged, which is located within a bounded chamber. The boundary of the

problem is represented by Γ, and the domain of the computational problem by Ω. The imaging domain in which the OI is reconstructed is $\mathcal{D}$. The antennas which illuminate the breast, and collect E^{tot} are located on the surface $\mathcal{S}$.

FEM-CSI solves for the unknown contrast variables in the problem. The contrast is typically defined as:

$$\chi(\vec{r}) = \frac{\epsilon_r(\vec{r}) - \epsilon_b}{\epsilon_b}, \tag{1.1}$$

where ϵ_r is the relative permittivity and ϵ_b is the relative background permittivity. In this formulation, the background permittivity is that of the homogeneous immersion medium in which the breast is submerged. However, this FEM-CSI algorithm allows for the use of a relative numerical inhomogeneous background, $\epsilon_n(\vec{r})$, redefining the contrast as

$$\chi(\vec{r}) = \frac{\epsilon_r(\vec{r}) - \epsilon_n(\vec{r})}{\epsilon_n(\vec{r})}. \tag{1.2}$$

This new definition, which is now a function of position, allows us to incorporate known information about the electrical and geometric properties of our object of interest into the inverse problem, helping to reduce the ill-posedness and improve our reconstructions by numerically reducing the contrast. Other easily obtainable prior information, such as restricting the imaging domain $\mathcal{D}$ to the object itself, does the same, improving results by removing unknowns from the problem. It is worth noting that the inhomogeneous background is not an initial guess of the solution, but remains in the contrast formulation throughout the optimization process as a numerical background permittivity. The mathematical formulation of the scattering problem is provided in Appendix: B.

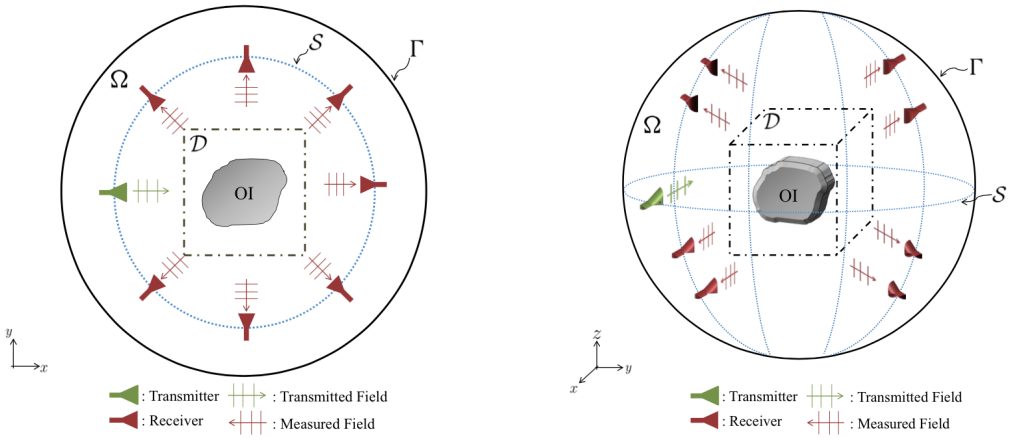

Figure 1.3: Left: two-dimensional and right: three dimensional models of the imaging problem. Here the OI is the object of interest being imaged, Ω is the problem domain, $\mathcal{D}$ is the imaging domain, Γ is the problem boundary and $\mathcal{S}$ is the surface where the receivers and transmitters are positioned. This image has been used with permission from Dr. Amer Zakaria.

The FEM-CSI algorithm solves for the contrast of an OI from scattered field data, by minimizing the following cost functional:

$$\mathcal{F}^{\text{CSI}}(\underline{\chi}, \underline{w}_t) = \mathcal{F}^{\mathcal{S}}(\underline{w}_t) + \mathcal{F}^{\mathcal{D}}(\underline{\chi}, \underline{w}_t), \tag{1.3}$$

where

$$\mathcal{F}^{\mathcal{S}}(\underline{w}_t) = \frac{\sum_t \left\| \underline{E}_t^{\text{sct,meas}} - \boldsymbol{\mathcal{M}}_{\mathcal{S}} \boldsymbol{\mathcal{L}}[\underline{w}_t] \right\|_{\mathcal{S}}^2}{\sum_t \left\| \underline{E}_t^{\text{sct,meas}} \right\|_{\mathcal{S}}^2}, \tag{1.4}$$

and

$$\mathcal{F}^{\mathcal{D}}(\underline{\chi}, \underline{w}_t) = \frac{\sum_t \left\| \underline{\chi} \odot \underline{E}_t^{\text{inc}} - \underline{w}_t + \underline{\chi} \odot \boldsymbol{\mathcal{M}}_{\mathcal{D}} \boldsymbol{\mathcal{L}}[\underline{w}_t] \right\|_{\mathcal{D}}^2}{\sum_t \left\| \underline{\chi} \odot \underline{E}_t^{\text{inc}} \right\|_{\mathcal{D}}^2} \tag{1.5}$$

are updated sequentially. Here $\underline{E}_t^{\text{sct,meas}} \in \mathbb{C}^R$ is the measured data at R receiver locations per transmitter, $\underline{w}_t \in \mathbb{C}^I$ is the contrast source values at I locations inside the domain $\mathcal{D}$, $\underline{\chi} \in \mathbb{C}^I$ are the contrast values at I locations inside the imaging domain $\mathcal{D}$ and $\underline{E}_t^{\text{inc}} \in \mathbb{C}^I$ is the incident field inside $\mathcal{D}$. The matrix operator $\boldsymbol{\mathcal{M}}_{\mathcal{S}} \in \mathbb{C}^{R \times N}$

transforms scattered field values in Ω to R receiver points per transmitter on $\mathcal{S}$, $\boldsymbol{\mathcal{M}}_{\mathcal{D}} \in \mathbb{C}^{I \times N}$ transforms nodal values in Ω to I nodes in the imaging domain $\mathcal{D}$, and $\boldsymbol{\mathcal{L}} \in \mathbb{C}^{N \times I}$ is the inverse FEM operator which transforms $\underline{w}_t$ in $\mathcal{D}$ to $\underline{E}^{\text{sct}}_{t,\Omega}$.

The ill-posedness of the inverse problem can be mitigated using the algorithm's optional multiplicative regularization (MR) feature. The regularization has been shown to enhance the quality of reconstructions due to its edge preserving characteristics and its ability to suppress noise in experimental data. Complete details and a derivation of this algorithm can be found in [32].

1.1.2 Prior Information

Non-linearity and ill-posedness are moderated using various techniques. One such technique is the incorporation of prior information into the inversion [33–35]. For example, [2] discusses using a patient-specific matching fluid, which is based on the known properties of the patient's breast, to optimize the amount of interrogation energy. In this case, the prior information is the known, patient specific, electrical properties of the breast. [27] uses the known upper and lower bounds of the electrical properties of breast tissue in order to constrain the imaging algorithm. This information is obtained from a set of literature values outlining the dielectric properties of breast tissues at microwave frequencies, and is not patient specific [4]. A regularization technique that derives patient specific prior information from MRI and computed tomography (CT) images is discussed in [33].

This thesis outlines ways in which we can take advantage of this particular FEM-CSI algorithm's ability to use a numerical inhomogeneous background, and applies new techniques to synthetic and experimental biological OIs. Initially, methods are developed to use prior information about the OI as a numerical background per-

mittivity, but this evolves into a method to use a general numerical background to regularize the problem that is independent of immersion medium or known electrical properties of the OI.

In order to incorporate the chosen numerical background into FEM-CSI, a numerical incident field, E_n^{inc}, is computed. This incident field is equivalent to the total field collected from the numerical background as a scatterer. The scattered field data used for inversion in the prior information case is then $E^{sct} = E^{tot} - E_n^{inc}$.

1.1.3 Inverse Crime

The term "Inverse Crime" describes a situation in which synthetic data is generated using a forward solver which is inherent in the inverse solver, and a mesh that is the same in the forward and inverse problems [36]. The 2D and 3D FEM forward and inverse solvers used in this thesis share the same theoretical formulation [32]. Therefore, in order to avoid an inverse crime, synthetic data is generated on a mesh that is distinct from the inverse mesh. Additionally, noise is added to all of the fields used for inversions. Due to the unique requirements of the 2D and 3D codes, the addition of noise is treated differently in the 2D and 3D cases.

In 2D, noise is added such that:

$$\underline{E}^{\text{sct}}_{\text{noisy}} = \underline{E}^{\text{sct}} + ||\underline{E}^{\text{sct}}||_{\infty} \frac{\eta}{\sqrt{2}} (\tau_1 + j\tau_2) \tag{1.6}$$

where $\underline{E}^{\text{sct}}$ is the scattered field data vector, which is synthetically generated on a unique mesh on the domain $\mathcal{S}$, $||\underline{E}^{\text{sct}}||_{\infty}$ is the maximum magnitude of the complex values of $\underline{E}^{\text{sct}}$, τ_1 and τ_2 are uniformly distributed random numbers between -1 and 1, and η is the desired noise level. In this thesis we typically choose to contaminate our synthetic data with 5% noise, therefore typically $\eta = 0.05$.

The addition of noise can be complicated by the addition of prior information as numerical background. For example, in 2D, the FEM forward solver generates synthetic data, which is then passed to CSI. If prior information is introduced, the scattered field data must be appropriately adjusted to account for the new numerical incident field. Noise is added to the scattered field before any adjustment is made. Therefore, the noise percentage is applied to the scattered field from the entire OI.

In 3D, the data collected has been shown to demonstrate some dependence on the mesh being used. Computational restrictions prevent the elimination of this dependence by further refining the mesh. Therefore in order to incorporate a numerical background, the background permittivities are introduced into the forward solver. The scattered field output from this process can be quite different from the scattered field of the entire OI, and so the noise addition process must be adjusted accordingly. This is accomplished by adding the equivalent amount of noise to the total field, and then subtracting the noiseless incident field data from the introduced numerical background.

1.1.4 Reconstruction Evaluation

When using simulated data, the quality of the reconstructed images can be evaluated by comparing them to the profile of the numerical phantom from which the data was collected. Various metrics can be used to assess the quality of an image, some of which will be discussed in more detail in Chapter 4. However for the majority of this thesis image evaluation will be performed using the L_2 vector error-norm given by

$$L_2 = \frac{||\epsilon_{\text{phantom}}(\mathbf{r}) - \epsilon_{\text{recon}}(\mathbf{r})||_2}{||\epsilon_{\text{phantom}}(\mathbf{r})||_2}, \tag{1.7}$$

where $\epsilon_{\text{phantom}}$ and ϵ_{recon} are the complex permittivities of the phantom and the recon-

struction, and **r** is inside the phantom. These norms are calculated by interpolating the compared images onto uniform square grids of decreasing cell size until the norms converge - a method described in [23]. The error norms for reconstructions of synthetic data sets are presented in each chapter in tabular form.

1.2 Outline

In Chapter 2, a simulated annealing (SA) algorithm is described, which is designed to detect prior information regions in reconstructed images of a human forearms. This SA algorithm utilizes data obtained from a human trial in which volunteers forearms were imaged using a 2D dipole array array in a saltwater immersion medium. FEM-CSI is used to reconstruct a 2D image of the volunteer's forearm, and the SA algorithm uses this image to search for regions of fat and muscle tissue. These regions are used as a numerical background and FEM-CSI is run again, resulting in an improvement on the original image [37].

Chapter 3 introduces a hybrid radar-MWT algorithm for breast cancer imaging using clinically (anatomically) realistic, MRI-based 2D numerical breast phantoms. The combined algorithm is developed for 2D imaging in a lossy glycerin immersion medium. Inversions are performed at various frequencies and show that the combined algorithm improves the quality of the reconstructions over either technique used alone. It also stabilizes inversions that converged to spurious solutions using the traditional FEM-CSI approach [38]. This method is extended to 3D numerical phantoms. Robustness to prior information, frequency, and boundary type is discussed.

The combined algorithm discussed in Chapter 3 has been identified as a potential tool for monitoring tumour size changes during cancer treatment. In Chapter 4, this application is explored using simulations using 2D and 3D numerical breast

phantoms that feature tumours of different sizes, representing various stages during cancer treatment. The results show that the increased sensitivity provided by the combined method allows for a reliable monitoring of size changes in the tumour.

The use of an appropriate immersion medium has been thought to be instrumental in reconstructing a high quality breast image for cancer detection. However, Chapter 5 shows that the FEM-CSI algorithm does not depend on immersion medium. The contrast can be reduced by defining a numerical background, and detailed reconstructions of the breast interior can be obtained in many different immersion media. The independence of the reconstruction algorithm to the immersion medium demonstrates the flexibility of choosing imaging system parameters based on considerations such as the wavelength in the surrounding medium, which affects the size and number of sensors that can occupy the imaging system.

The thesis is concluded in Chapter 6, with a summary of the impact of this research and a discussion of future work.

Chapter 2

Estimation of Prior Information Regions Using Simulated Annealing

In this chapter, a simulated annealing (SA) algorithm is used to detect prior information regions in reconstructed forearm images. The algorithm is applied to experimental data collected from a group of volunteers using a 2D dipole array pictured in Fig. 2.1. Reconstructions were performed using the 2D TM formulation of FEM-CSI. The SA algorithm works on the reconstructed images, detecting a number of discrete regions within the image. These regions are identified as fat and muscle tissue, and their location and electrical properties are reintroduced into FEM-CSI as prior information in the form of an inhomogeneous numerical background. The resulting reconstructions are an improvement on the original images. Comparisons are made to an ad-hoc method in which prior information regions are obtained visually from the imaginary part of the original reconstructed image.

2.1 Introduction to Human Forearm Study

While the focus of this thesis is breast cancer imaging, the forearm study described here was the EIL's first experimental test to image human volunteers. This study allowed for the testing of reconstruction algorithms on data obtained from biological tissues and set the stage for future clinical trials. The forearms of five volunteers were imaged using a 2D array of 24 dipole antennas that were submerged in a saltwater immersion medium with a permittivity of $\epsilon_b \approx 77 - j15$. The data were collected inside a metallic chamber with a radius of 22.4 cm. The antennas were positioned 9.4 cm from the centre of the chamber and polarized along the z-coordinate.

We show images obtained from three volunteers, labelled volunteer 1, volunteer 2, and volunteer 3. While this method was used on data collected from other volunteers, these were chosen because they display a diverse fat tissue thickness as shown by an MRI scan, providing an ideal testbed for the designed imaging method. Collected data was inverted using 2D TM MR FEM-CSI using a square imaging domain $\mathcal{D}$, chosen to contain the arm and minimize the number of unknowns being reconstructed in the immersion medium. The resulting images, which we typically refer to as "blind" images because they are the result of a reconstruction that uses little or no prior information, are shown in Figs. 2.5, 2.6, 2.7, a and b. The term "blind" reconstruction will be carried throughout this thesis. A blind inversion may use minimal prior information such as restricting the upper and lower bounds of the unknowns to the known dielectric limits of biological tissues, or restricting the imaging domain to eliminate unknowns that are known to be within the immersion medium. A blind inversion will not use a numerical background or initial guess that is based on known properties of the OI.

FEM-CSI is able to reconstruct a reasonable image of volunteer 1's forearm. How-

ever the bones are not apparent in the reconstructions for volunteer 2 and 3. There is also a considerable amount of blurring around the exterior of the arm, making it difficult to determine its exact location, and the variability in the fat layer is poorly reconstructed. These blind images provide us with the motivation to use prior information about the volunteers forearm to improve the reconstruction.

An ad-hoc method designed by Zakaria is described in [37]. However this method requires the user to estimate the fat layer by eye, and manually input regions of immersion medium, fat tissue, and muscle tissue into the inhomogeneous background. This method is undeniably user dependent, and an automated method was designed to overcome this dependency. This method, which is based on a simulated annealing optimization algorithm, is described in the following section.

2.2 Simulated Annealing

Simulated annealing (SA) is a stochastic global optimization technique that minimizes a cost functional that may have several local minima. The basic idea is that the distribution of energy states remains close to statistical equilibrium if the cooling is slow, such that the global ground state can be achieved as the temperature approaches zero. A well-annealed metal contains large crystals and few defects, such that the Gibb's free energy is near the theoretical minimum. The configuration of atoms in the material should be arranged such that the size of the crystals is large, and the material contains minimal defects. The characteristics of the solid depend on the Gibbs free energy. Therefore the defined cost functional has the form of an energy function. Random perturbations in the variables change the value of the energy function, and the probability of acceptance of this new state is weighted by the Boltzmann probability factor $\exp(-\Delta U/k_{boltz}T)$ where ΔU is the change in the en-

(a) (b)

Figure 2.1: (a) Dipole antenna for 1GHz incident field transmission in saltwater immersion medium. (b) Data being collected from volunteer's forearm.

ergy configuration, k_{boltz} is Boltzmann's constant, redefined here to avoid confusion with background wave number, and T is the temperature. A cooling schedule is defined for T. Perturbations that increase energy are common near the start of an SA run, but become less common as the temperature decreases [39].

When the SA run reaches it's final "frozen" state, it is at a minimum energy configuration. In SA, the search space is discrete, making it a good tool for finding distinct tissue regions in an image. The algorithm is also fast, and because 2D TM FEM-CSI is not particularly sensitive to small variations in prior information regions, finding an acceptable global minimum is sufficient if it can be found quickly [40].

In this formulation, the cost functional or energy function is the statistical correlation coefficient between a vectorized image of the reconstructed forearm D_n, and a segmented image and parameter set S_n, It is defined as

$$U = \frac{s_{DS}}{\sigma_{dev,D}\sigma_{dev,S}}, \tag{2.1}$$

where s_{DS} is the covariance between D and S, and $\sigma_{dev,D}$ and $\sigma_{dev,S}$ are the standard deviations of D and S respectively.

We define $M = 6$ distinct dielectric regions to represent tissue types in the forearm, and transitions between tissue boundaries that FEM-CSI may reconstruct as artifacts. The number of dielectric regions is chosen by the user. It assumes some knowledge of how dielectric regions present themselves in a blind reconstruction. For example, the boundary between the arm and the immersion media may not necessarily be reconstructed as sharp, but as a gradual progression between the properties of muscle tissue and immersion medium. A dielectric region should be chosen to account for this transitional layer, and any others that may present themselves in the blind image. The regions are assigned integer values $m = 1, 2, \ldots, M$. The algorithm initializes N pixels in a segmented image S_n, with a random value from the parameter set $S_n \in \{1, 2, \ldots, M\}$, where $n \in \{1, 2, \ldots, N\}$.

At each iteration, the algorithm randomly perturbs one of the parameters of S_n, creating a new segmented image $S_n^{'}$, and a new energy $U^{'}$ is calculated. The probability of $U^{'}$ being accepted as the new state given by

$$P(U^{'}) = \begin{cases} 1 & \text{if } U^{'} \leq U \\ \exp(-(U^{'} - U/)T_k) & \text{if } U^{'} > U \end{cases}$$

The temperature at iteration k, T_k, is initialized at infinity, but after every 100 iterations is defined as the standard deviation of the previous 99 energies. The optimization is terminated when a convergence criteria is met, defined as when perturbing a single pixel does not change the energy more than a defined amount that is regarded as negligible [40].

This algorithm was initially tested on data collected from a 2D numerical forearm

phantom. Fig. 2.2 a, b and c, show the SA algorithm applied to the blind reconstruction of the numerical phantom, at various stages of convergence. The overlayed contour plots show the regional variations in the blind reconstruction.

2.3 Fat Region Creation and Refinement

The converged segmented images with contours of the blind image superimposed are shown in Figure 2.2 c. Here, the colour bar shows the segmentation levels. In order to obtain accurate prior information about the fat layer and interior of the forearm, the regions corresponding to areas outside of the arm must be removed. First, the pixels in the highest integer state are set to zero, as this state is located outside of the arm in the immersion medium. The next highest corresponds to the transitional area between the arm and the immersion medium, and is also set to zero. The remaining states are set to one, creating a binary image of the arm location that can be utilized by the function *edge*. This function, which is found in the MATLAB image processing toolbox, returns an image of the edge of the non-zero pixels. A two pixel dilation towards the centre of the edge is used in order to avoid an overly thin estimation of the fat layer. The dielectric values are assigned according to Table 2.1, where the interior is assigned the permittivity of muscle and the outer layer the permittivity of fat tissue. The remaining region is assigned the permittivity of the immersion medium. The prior information regions determined from the numerical phantom reconstruction are shown in Figure 2.2 d. Prior information regions from the actual biological targets is shown in Figure 2.3 and Figure 2.4.

Further refinement of the region is applied using the CSI algorithm. If the size of the arm is overestimated, the reconstruction shows a saturation of the maximum allowed permittivity in the immersion medium. This instability is a result of inac-

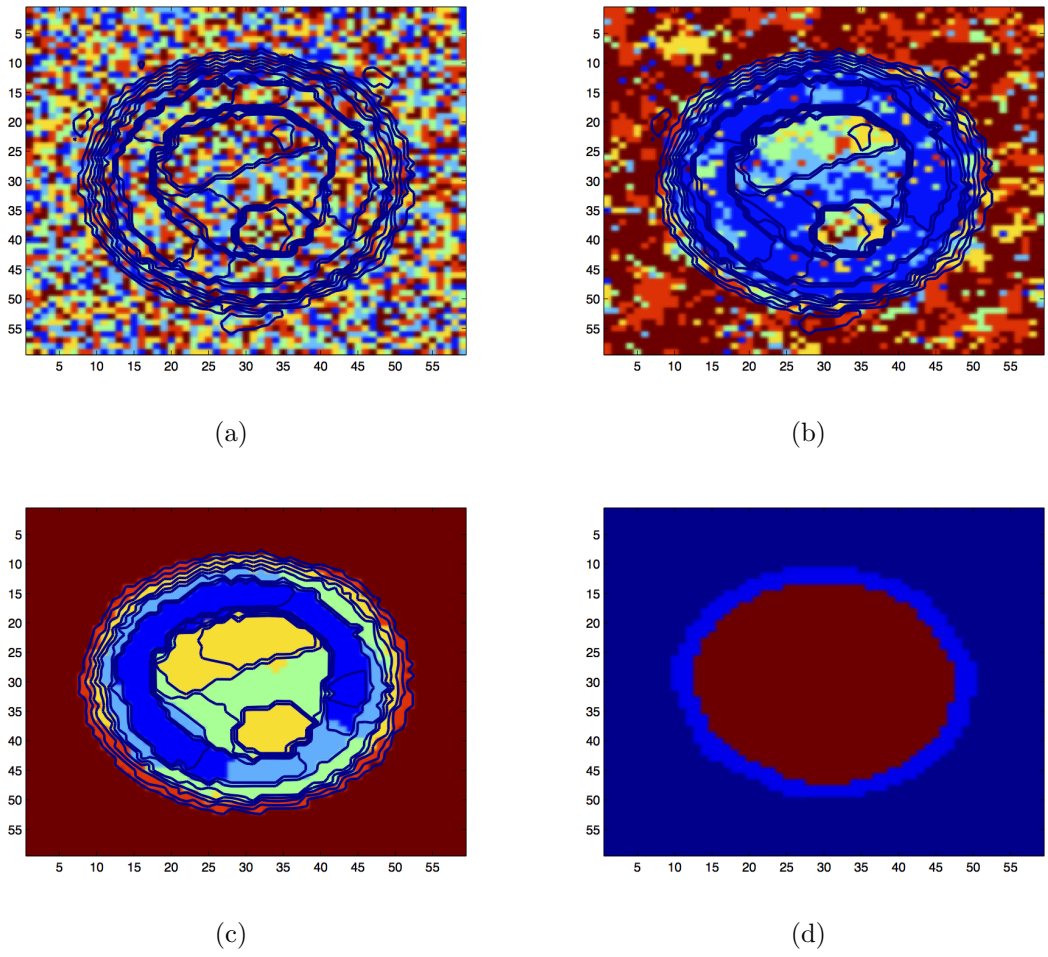

Figure 2.2: Simulated annealing algorithm run on synthetic data after (a) random initialization, (b) 8000 iterations, (c) convergence and (d) after the fat layer is determined.

Imaging Region	Permittivity
Immersion Medium	77-j15
Fat Layer	10-j1
Muscle Interior	50-j20

Table 2.1: Inhomogeneous numerical background permittivities for human forearm tissue [1].

curately constraining the background permittivity values as fat tissue, increasing the contrast in a region that should have the properties of saltwater. The number of saturated pixels in the immersion medium decreases as the size of the arm region is reduced and approaches the true size. In order to minimize this effect and accurately reconstruct the arm, the size of the forearm prior information region is uniformly reduced, and chosen as the size at which the permittivity saturation begins to stop, and the immersion medium is accurately reconstructed.

2.4 Reconstructions Using Prior Information

Figures 2.5, 2.6, 2.7 c and d show reconstruction results using the manual method, in which the fat tissue region is drawn by eye. Figures 2.5, 2.6, 2.7 e and f show results using the automated method.

Both the manual and the automated methods show a large improvement over the blind images. The bones are distinguishable in all of the reconstructions, and the muscle layer becomes more uniform after the inclusion of prior information. The blurring of features is significantly reduced, creating sharper boundaries between tissue types and creating a more diagnostically useful image.

A drawback of the automated method is that although it can find the location of the fat layer, it could not assign it a variable thickness - a more realistic scenario accounted for in the manual method. However, the manual method can suffer from user inconsistency. Visually, it is difficult to distinguish any quality difference between the manual and SA methods when considering the interiors of the arms. MRI images of the volunteer's forearms are available for comparison in [41]. Note that these images were not used in either method to derive prior information, but are provided for a visual comparison only. Image registration limitations prevent a direct comparison

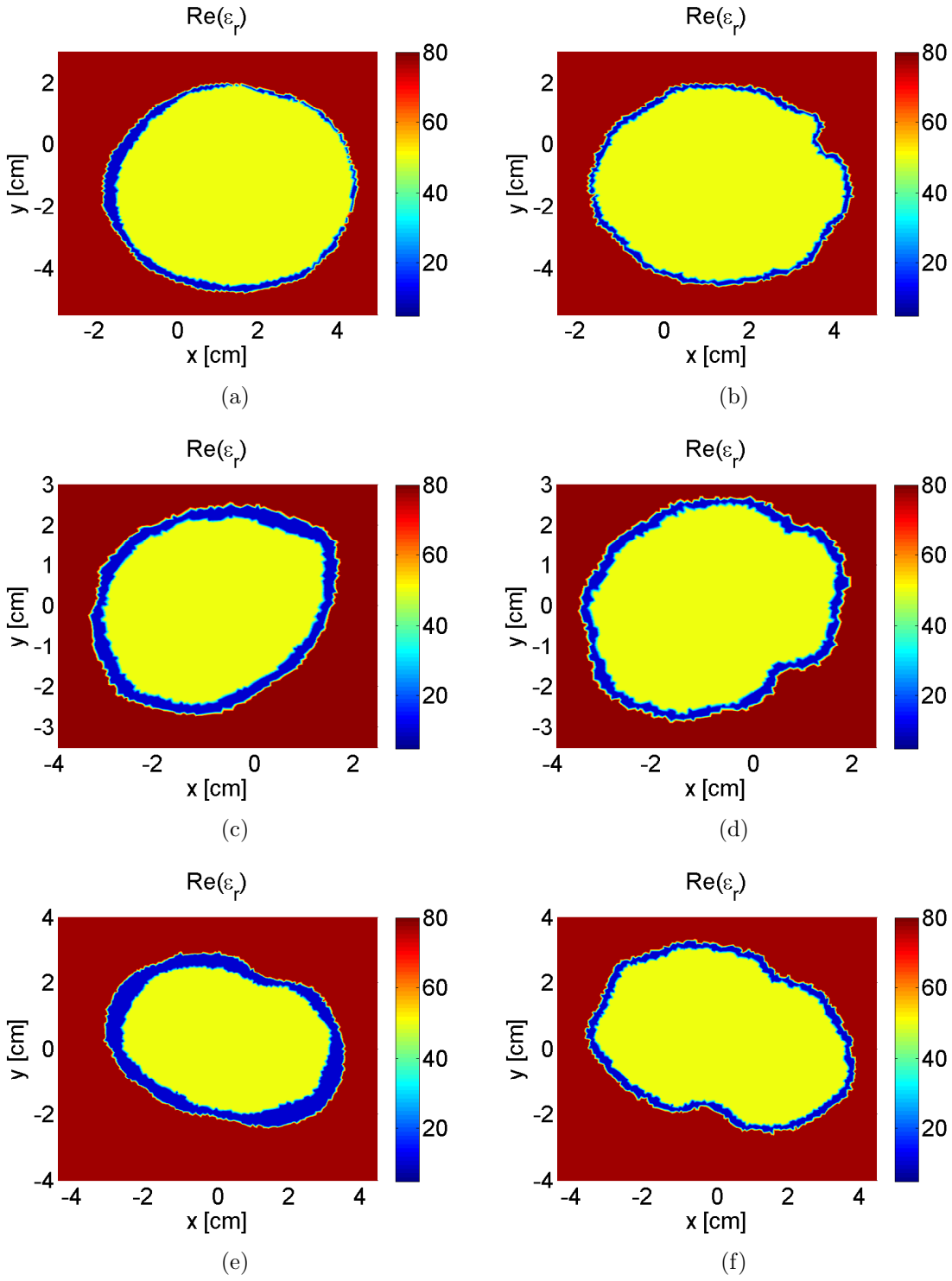

Figure 2.3: Real part of prior information: (a) Ad-hoc and (b) SA methods prior information regions for volunteer 1. (c) Ad-hoc and (d) SA methods prior information regions for volunteer 2. (e) Ad-hoc and (f) SA methods prior information regions for volunteer 3. Some images appear in [37]. © 2012 IEEE. Used with permission.

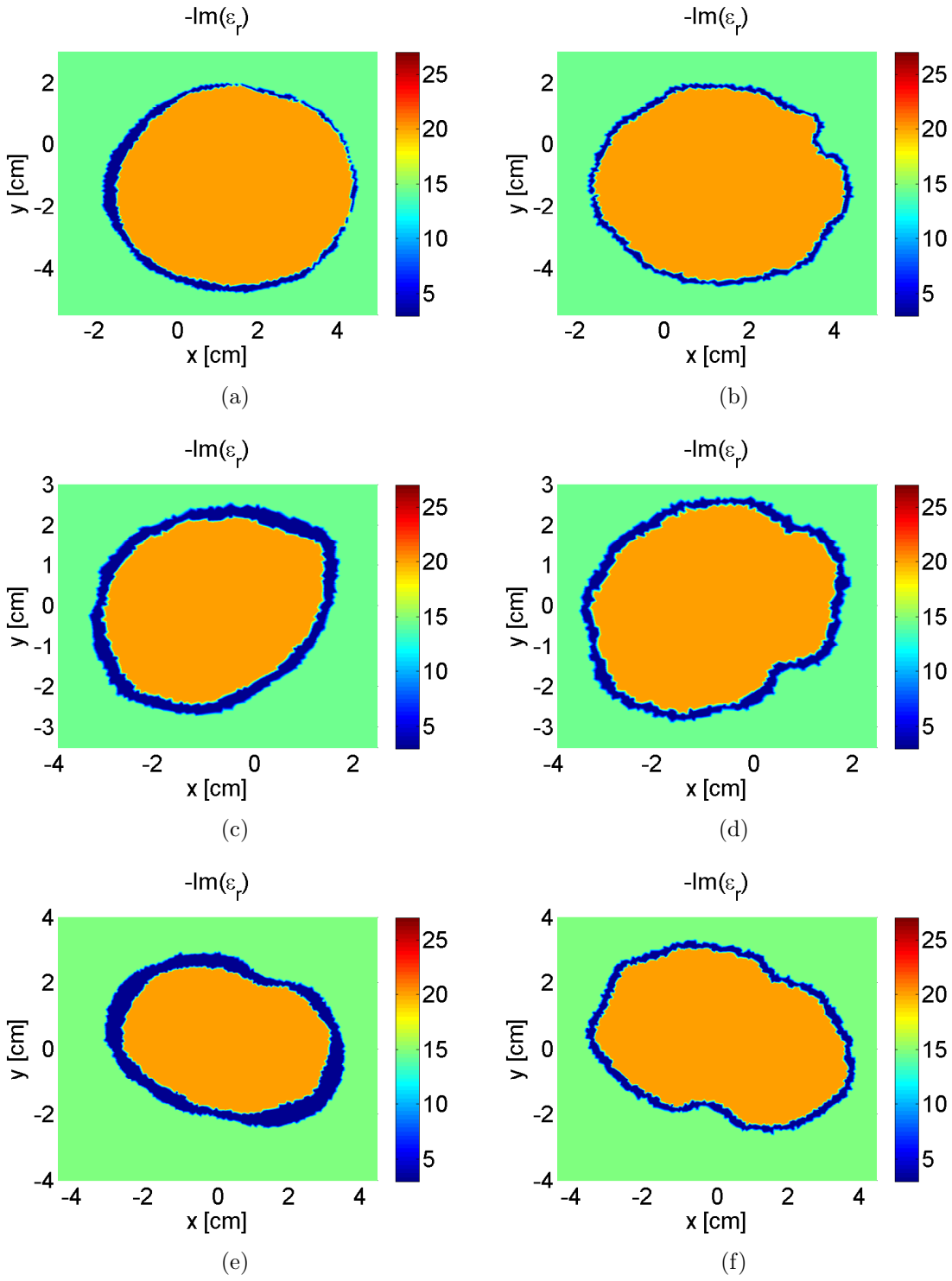

Figure 2.4: Imaginary part of prior information: (a) Ad-hoc and (b) SA methods prior information regions for volunteer 1. (c) Ad-hoc and (d) SA methods prior information regions for volunteer 2. (e) Ad-hoc and (f) SA methods prior information regions for volunteer 3. Some images appear in [37]. © 2012 IEEE. Used with permission.

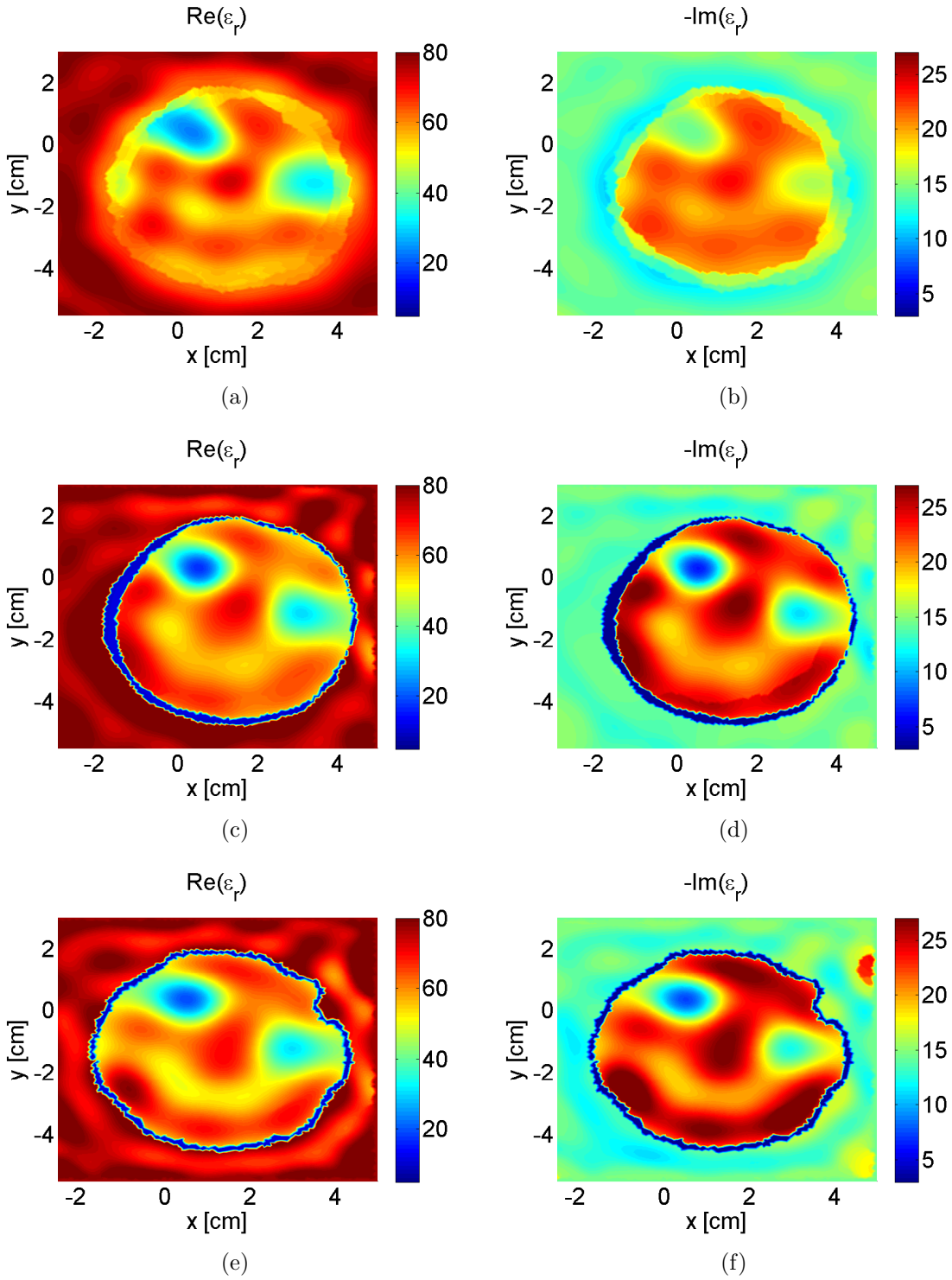

Figure 2.5: Volunteer 1: (a), (b) Real and imaginary blind reconstructions of forearm. (c), (d) Real and imaginary reconstructions using prior information derived using the ad-hoc method. (e), (f) Real and imaginary reconstructions using prior information derived from SA method. Some images appear in [37].

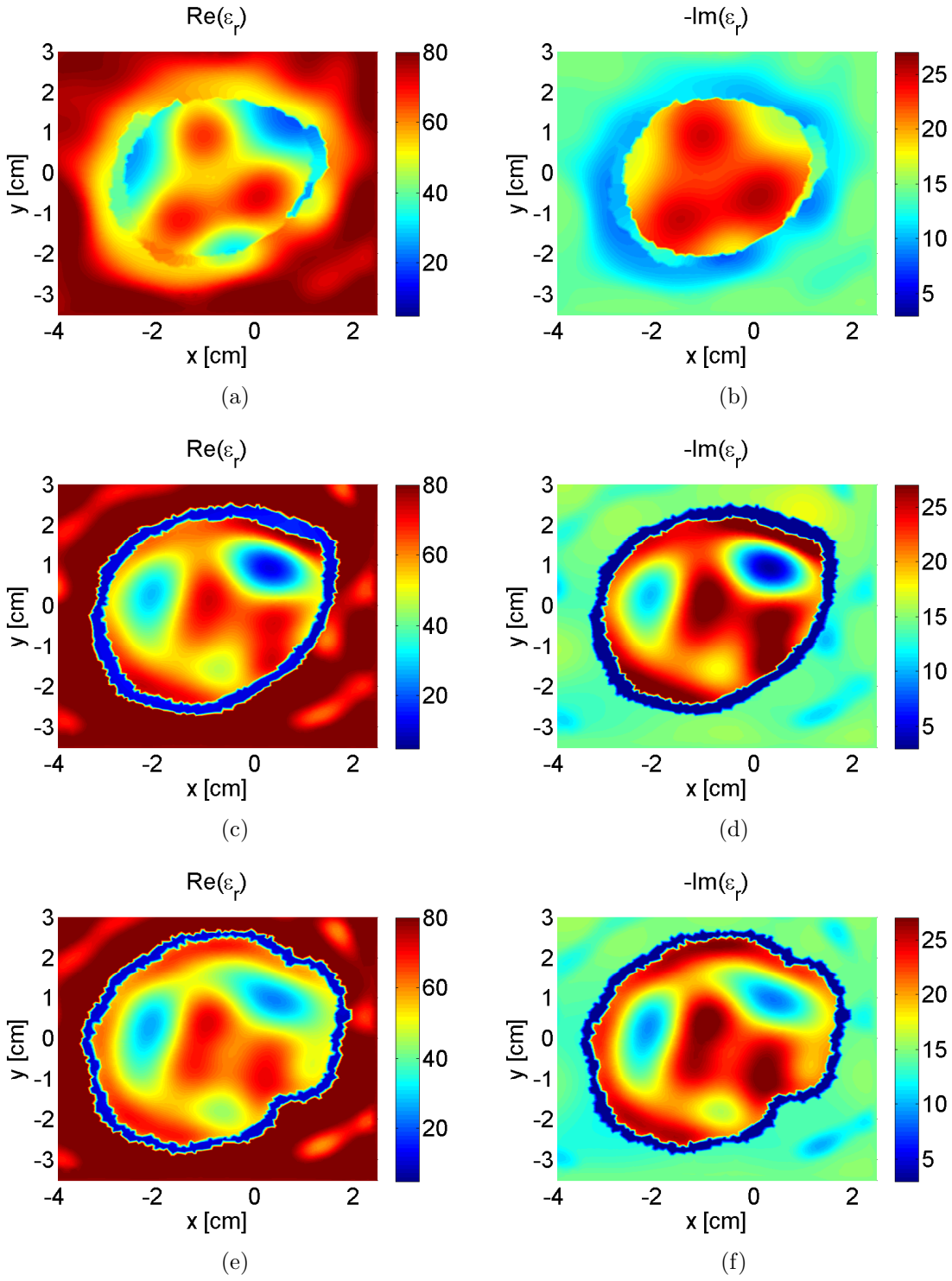

Figure 2.6: Volunteer 2: (a), (b) Real and imaginary blind reconstructions of forearm. (c), (d) Real and imaginary reconstructions using prior information derived using the ad-hoc method. (e), (f) Real and imaginary reconstructions using prior information derived from SA method. Some images appear in [37].

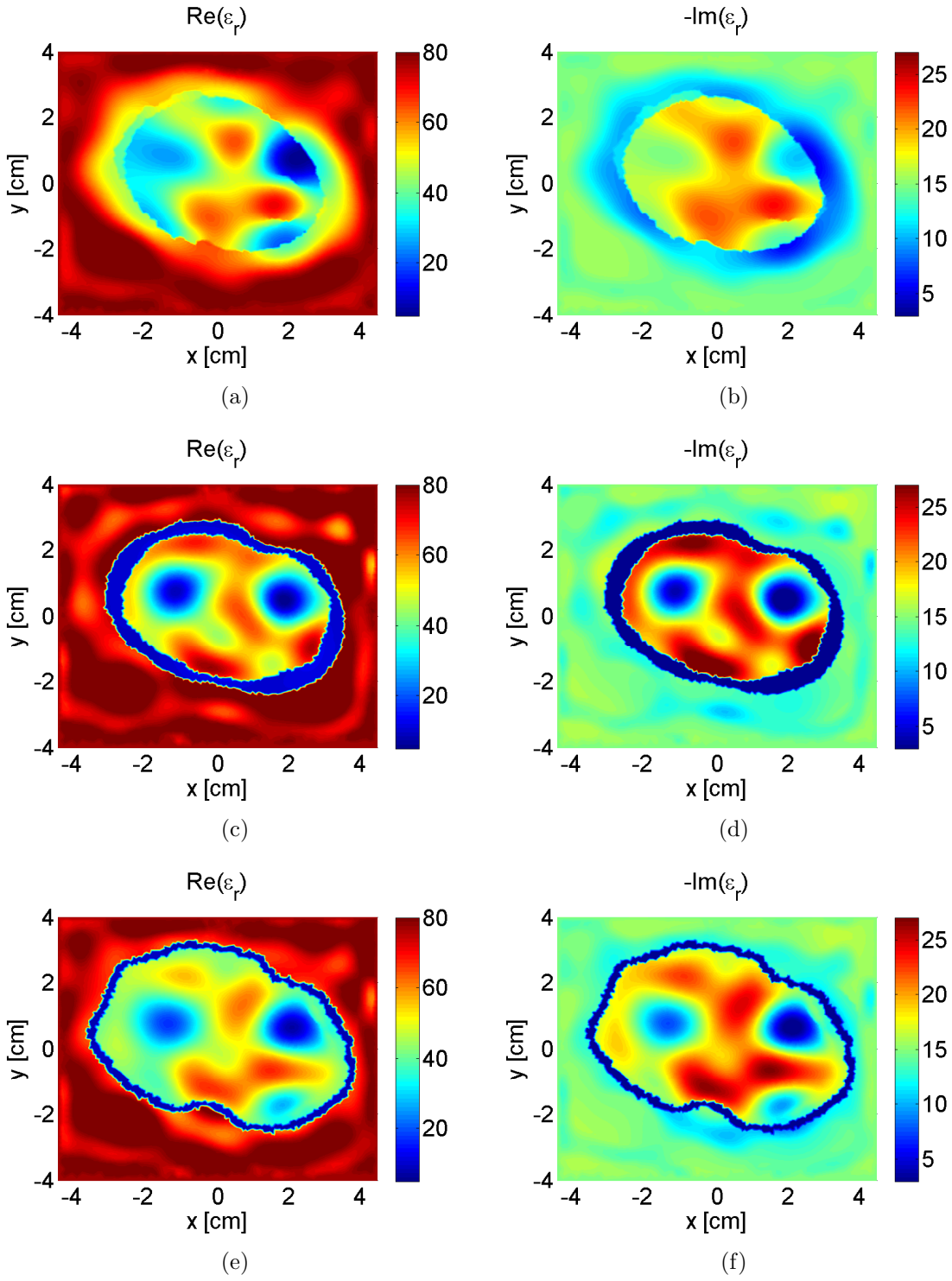

Figure 2.7: Volunteer 3: (a), (b) Real and imaginary blind reconstructions of forearm. (c), (d) Real and imaginary reconstructions using prior information derived using the ad-hoc method. (e), (f) Real and imaginary reconstructions using prior information derived from SA method. Some images appear in [37].

between the estimated and actual thickness of the fat layers.

This initial human volunteer study influenced decisions for building the current breast imaging systems being used by the EIL and also advanced our understanding of how important prior information is when attempting to solve ill-posed problems in MWI. While the SA method has only been tested on forearm images, it could be applied to any biological reconstructions that are known to contain an inhomogeneous dielectric profile.

The conclusion of this forearm study marked the beginning of a three year Canadian Breast Cancer Foundation funded collaboration between the University of Manitoba and the University of Calgary. The work from this collaboration, which will be discussed in upcoming chapters, shifted our focus to ways of obtaining prior information using the imaging system itself, rather than using post-processing techniques such as the SA algorithm.

Chapter 3

Combined Radar/Microwave Tomography Algorithm

This chapter outlines a method that combines MWT and radar techniques. MWT and a MW radar tissue region estimation method are combined in a novel algorithm with potential application to breast tumour detection, and the monitoring of tumour size during treatment. The radar technique is used to derive a patient specific regional tissue map, which is incorporated into FEM-CSI as a numerical inhomogeneous background. The regional tissue map contains regions of skin, fat and fibroglandular tissue, the dielectric properties of which are estimated by an intermediate inverse solver. Results from 2D realistic numerical phantoms are used to demonstrate this algorithm, which is then verified in 3D using numerical phantoms and 3D tomography and radar algorithms.

3.1 Using Radar-Derived Regional Maps as Prior Information in MWT

Two imaging techniques that utilize energy at microwave frequencies are radar imaging and microwave tomography. Radar imaging provides low resolution information about an object's electrical and physical structure by taking advantage of the time of arrival and amplitude of backscattered fields that arise due to dielectric contrasts. In a typical setup, a single antenna is used to transmit an ulrawideband (UWB) pulse that penetrates into the breast and is scattered by any tissues that exhibit a dielectric difference. A tumour is a significant scatterer that can be detected using this technique. However difficulties arise when that tumour is embedded in dense fibroglandular tissue that produces its own reflections and reduces the interrogation energy due to its high loss.

The radar technique used in this combined algorithm is not subject to these limitations since the intention is not to produce a high resolution image to detect a tumour, but to determine the breasts basic structure and generate a regional map of breast tissues that can be used in FEM-CSI [42].

Before the technique is applied, 2D realistic phantoms are generated from a coronal slice of high-resolution MRI data. They are constructed by mapping the MRI pixel intensity values to the dielectric property intervals shown in Table 3.1. Details on the mapping procedure can be found in [43]. The phantoms from which radar and tomography data are collected are shown in Figures 3.4 - 3.7 a and b.

The radar technique, developed by Dr. Douglas Kurrant at the University of Calgary, uses reflection data collected with a monostatic, co-located transmitter/receiver, that is rotated to equally spaced points surrounding the breast. The transmit-

ter/receiver positions are shown in Figure 3.1 a. The breast is illuminated with a -3 dB UWB differentiated Gaussian pulse with a bandwidth of 4.14 GHz, and a frequency range of 1.45-5.59 GHz. These specifications are based on the range of the antennas used in the University of Calgary's experimental system [25]. The data are obtained using the finite difference time domain (FDTD) technique, where noise is added to the backscattered fields such that the signal-to-noise (SNR) ratio is 20 dB. Here the time domain SNR is defined as the ratio of scattered field energy to the energy of the added noise.

Each region is first approximated using points, shown in Figure 3.1 b, which are located along the tissue interfaces. A 2 mm uniform skin layer is assumed, as the location of the skin is easily determined clinically by using a laser. The remaining regions are estimated by fitting contours to the radar interface points. An example of the segmented regions, which represent skin, fat, and fibroglandular tissues are shown for a particular phantom in Figure 3.2.

Once the spatial properties are determined, the average dielectric properties of the segmented regions must be found. This is accomplished using the distorted Born iterative method (DBIM), where the unknowns are the three tissue regions. The result is a patient specific spatial map of breast tissues, shown for two different numerical phantoms in Figures 3.4-3.7 e and f. This map is incorporated into FEM-CSI as a

Tissue Type,	Re$\{\epsilon\}$	Im$\{\epsilon\}$
Fibroglandular-high	(36.41,47.45]	(10.95,15.32]
Fibroglandular-medium	(34.91,36.41]	(10.22,10.95]
Fibroglandular-low	(21.55,34.91]	(10.13,10.22]
Fat - high	(4.73,8.19]	(0.78,9.49]
Fat - medium	(4.07,4.73]	(0.5,0.78]
Fat - low	[2.42,4.07]	[0.06,0.50]

Table 3.1: Breast dielectric property ranges at 1GHz [4].

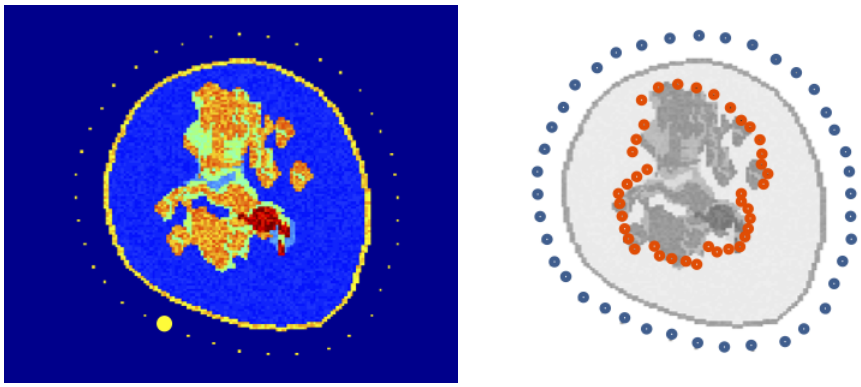

(a) (b)

Figure 3.1: *Radar regional algorithm*: (a) Transmitter receiver positions with respect to breast phantom. (b) Regional interface points. Images used with permission from Dr. Douglas Kurrant, University of Calgary.

(a) (b) (c)

Figure 3.2: *Segmented radar regions*: (a) Skin (b) fat and (c) fibroglandular tissues. Images used with permission from Dr. Douglas Kurrant, University of Calgary

numerical inhomogeneous background.

The MWT component of this algorithm collects single-frequency, TM polarized scattered field data from the 2D numerical phantoms. Data are collected with 24 receiving and transmitting antennas in a circular configuration around the breast. The technique is demonstrated using a glycerin solution immersion medium with a permittivity of $\epsilon_b = 23.3 - j23.4$ at 1GHz and a medium with a permittivity of $\epsilon_b = 38 - j13$ at 2 GHz. These two different immersion media are not optimized for the phantoms being imaged, but are intended to show the techniques robustness to frequency and background permittivity. For example, while the glycerin solution immersion medium is used for breast imaging [26], the second medium was based on one used for a brain imaging study described in [44]. Note that the radar data are collected using air as an immersion medium, but the same results can be obtained in any medium. Absorbing boundary conditions are assigned to the boundaries of the MWT imaging chamber. Note that these parameters are specific to the simulation results that are being presented, but in practice, and in other simulations, we are not restricted to this particular polarization, antenna configuration, immersion medium, frequency or boundary condition.

An "inverse crime" is avoided by collecting the forward data on a different mesh than the one used in in the inversion. Additionally, the scattered field tomography data is contaminated with 5% noise. This corresponds to an SNR equivalent to the 20 dB used in the radar data collection.

The tomography data are first inverted using 2D TM MR FEM-CSI without the radar regional information. The result is a blind reconstruction of the complex permittivity of the breast phantoms, shown for each of the two cases in Figures 3.4 - 3.7 c and d. The reconstructions are of poor quality. However they are presented in

order to compare traditional MWT results with those using the combined radar-MWT approach.

When using the combined method, the radar regional map is incorporated into the contrast function given in Equation 1.2 as a numerical inhomogeneous background $\epsilon_n(r)$. The results using the combined method are shown in Figures 3.4 - 3.7 g and h. A flowchart describing the traditional and combined techniques is shown in Figure 3.3. Note that the results are labelled by case, where the leading number represents the phantom being imaged, and the following number represents the frequency of the incident field.

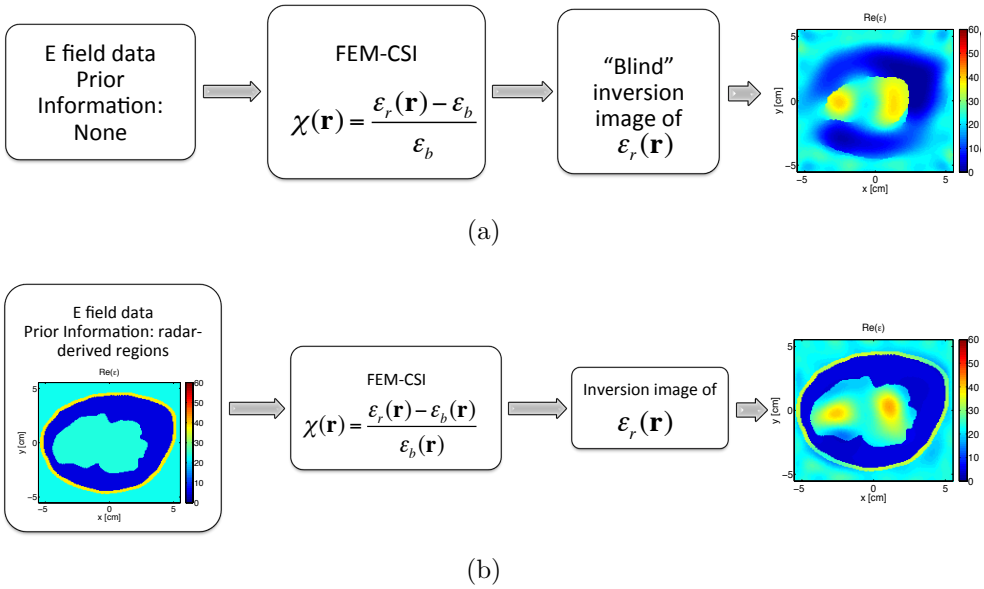

Figure 3.3: *Algorithm Flowchart*: (a) Standard FEM-CSI algorithm progression. (b) FEM-CSI algorithm including radar derived prior information.

3.2 Analysis of Reconstruction Improvement

Visually, there is a noticeable improvement in the reconstructions when using the combined method. The improvement of the combined approach over the blind

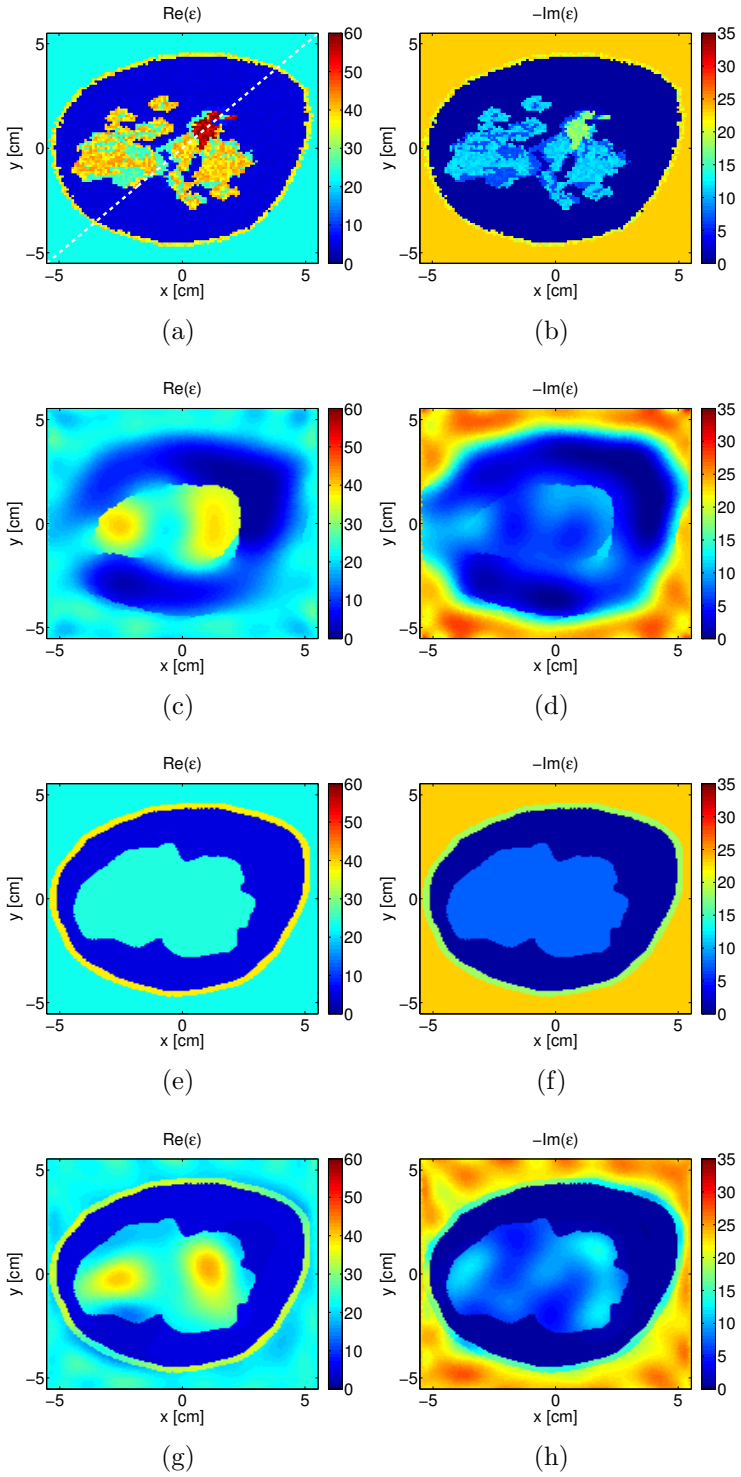

Figure 3.4: *Case 1-1, 1 GHz incident field*: (a) and (b): Real and imaginary parts of breast phantom. (c) and (d): Real and imaginary parts of FEM-CSI reconstruction without prior information. (e) and (f): Real and imaginary parts of prior information obtained from radar-based imaging. (g) and (h): Real and imaginary parts of FEM-CSI reconstruction with prior information. Images appear in [38]. Used with permission.

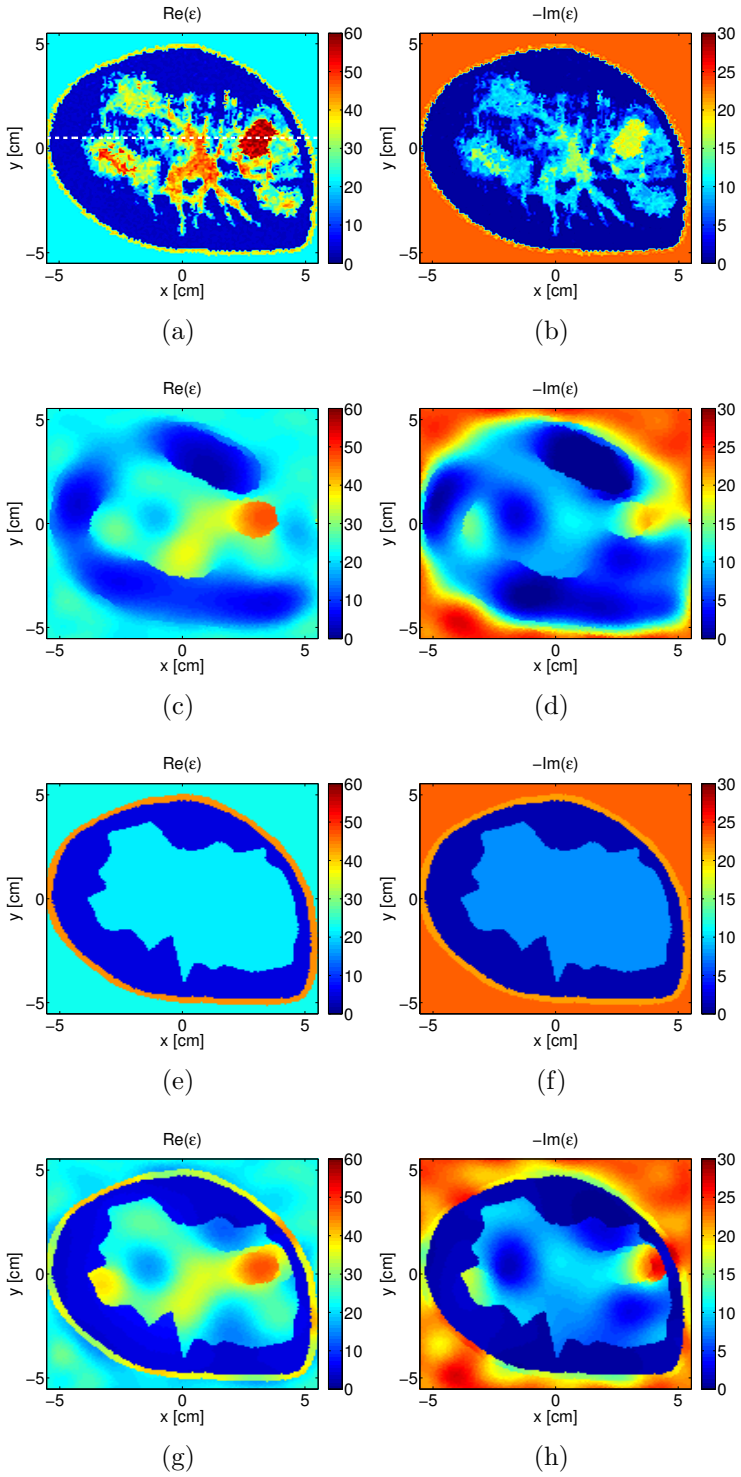

Figure 3.5: *Case 1-2, 1 GHz incident field*: (a) and (b): Real and imaginary parts of breast phantom. (c) and (d): Real and imaginary parts of FEM-CSI reconstruction without prior information. (e) and (f): Real and imaginary parts of prior information obtained from radar-based imaging. (g) and (h): Real and imaginary parts of FEM-CSI reconstruction with prior information. Images appear in [38]. Used with permission.

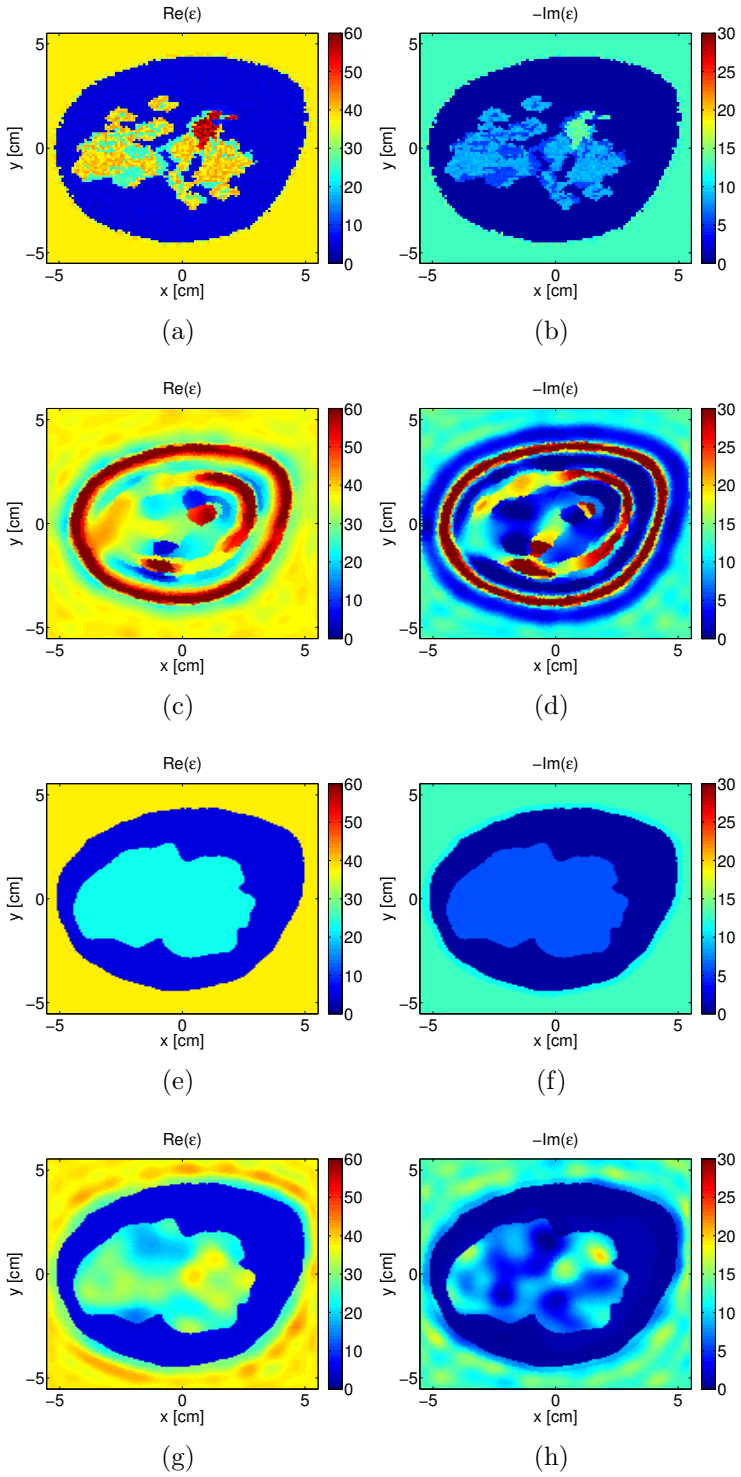

Figure 3.6: *Case 2-1, 2 GHz incident field*: (a) and (b): Real and imaginary parts of breast phantom. (c) and (d): Real and imaginary parts of FEM-CSI reconstruction without prior information. (e) and (f): Real and imaginary parts of prior information obtained from radar-based imaging. (g) and (h): Real and imaginary parts of FEM-CSI reconstruction with prior information. Images appear in [38]. Used with permission.

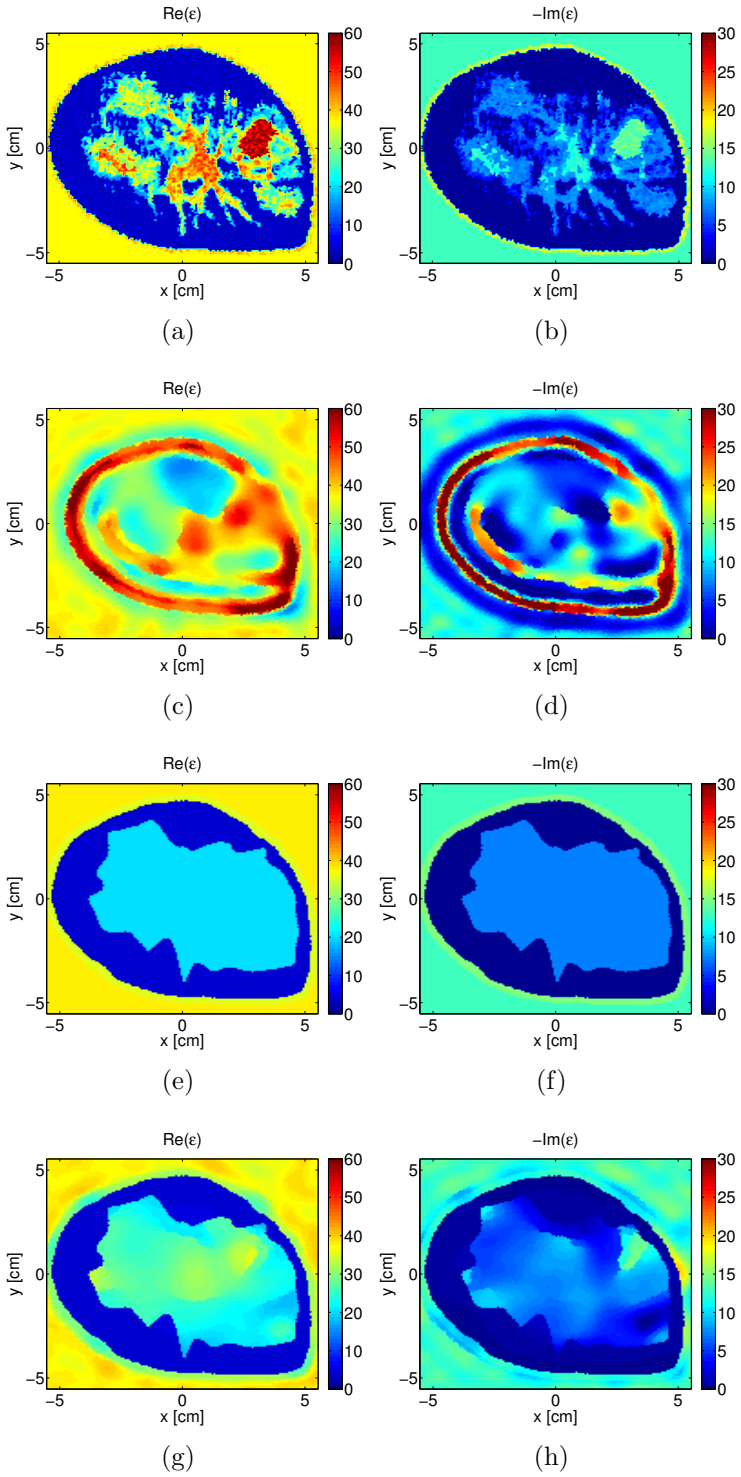

Figure 3.7: *Case 2-2, 2 GHz incident field*: (a) and (b): Real and imaginary parts of breast phantom. (c) and (d): Real and imaginary parts of FEM-CSI reconstruction without prior information. (e) and (f): Real and imaginary parts of prior information obtained from radar-based imaging. (g) and (h): Real and imaginary parts of FEM-CSI reconstruction with prior information. Images appear in [38]. Used with permission.

inversion is also quantified by calculating the L_2 norms, which are listed in Table 3.2.

Cross sectional plots, in which the cross section bisects the tumour are shown in Figure 3.8. The position of this cross section on the phantom can be seen as a dashed white line in Figures 3.4 a and 3.5 a. The results show an improvement in our ability to detect details, such as potential tumours, within the fibroglandular region of the breast. The regional maps created by the radar-based technique provide a context for the potential tumour detections, showing that they have been located, as expected, in the fibroglandular region. This context validates the detection, as we do not expect to see tumours in the fat tissue. All of the results, with the exception of Case 1-2, show a quantifiable improvement when using the combined method. This case is unique in that the quality of the blind reconstruction is high and already provides some useful diagnostic information.

Using the radar regional maps also provides the regularization required in the inverse problem to stabilize previously unstable solutions. This is particularly evident in the 2 GHz cases, where the blind reconstruction converged to an inaccurate solution saturated by the maximum allowed dielectric value. The regional map also provides balancing of the real and imaginary variables. It is typical in MWT reconstructions to have difficulty reconstructing the imaginary part of the image because it is much smaller than the real part, and therefore has much less of an impact on the objective

Model Number	L_2 Blind Inversion	L_2 Prior Information
1-1, 1GHz	55.7%	49.6%
1-2, 1GHz	65.3%	71.3%
2-1, 2GHz	154.1%	48.7%
2-2, 2GHz	114.1%	72.5%

Table 3.2: L_2 norms for FEM-CSI reconstructions with and without radar-derived prior information.

function. This is evident in the imaginary parts of the blind reconstructions, which are blurry and show no potential tumour detection. Once the regional map is introduced, the quality of the imaginary reconstruction is increased, and we begin to see the correlation that we expect between the real and imaginary parts of the permittivity.

Case 1-1 shows details in the fibroglandular region that are similar to the known structure of the phantom. The reconstruction is improved in the combined method, since it recovers the properties of the different tissue types more accurately than the blind reconstruction. The regional transitions are also more defined. Case 1-2 shows an increase in L_2 using the combined method, which is likely due to the overestimation of the imaginary part of tumour. Regardless, the combined method still provides useful information. The tumour is located at the edge of the fibroglandular region, supporting its classification as a tumour.

Case 2-1 and Case 2-2 both show the regularization feature that is associated with adding high quality prior information to our problem. The blind reconstruction shows a completely unstable solution that contains no useful diagnostic information. Once the regional map is used, the solution is stabilized in both cases. The tumour and detailed variations within the fibroglandular region also appear in Case 2-1. Unfortunately, although the solution is stabilized in Case 2-2, no useful details are reconstructed within the breast.

3.3 3D Combined Algorithm

In this section we extend the methods presented in the 2D simulations to a complete 3D scenario. The phantom used for this study, shown in Figures 3.13 - 3.15 a and b, is a simplified version of the realistic MRI phantoms used in the 2D case. The dielectric properties of the tissue regions shown in Table. 3.3 are realistic, but

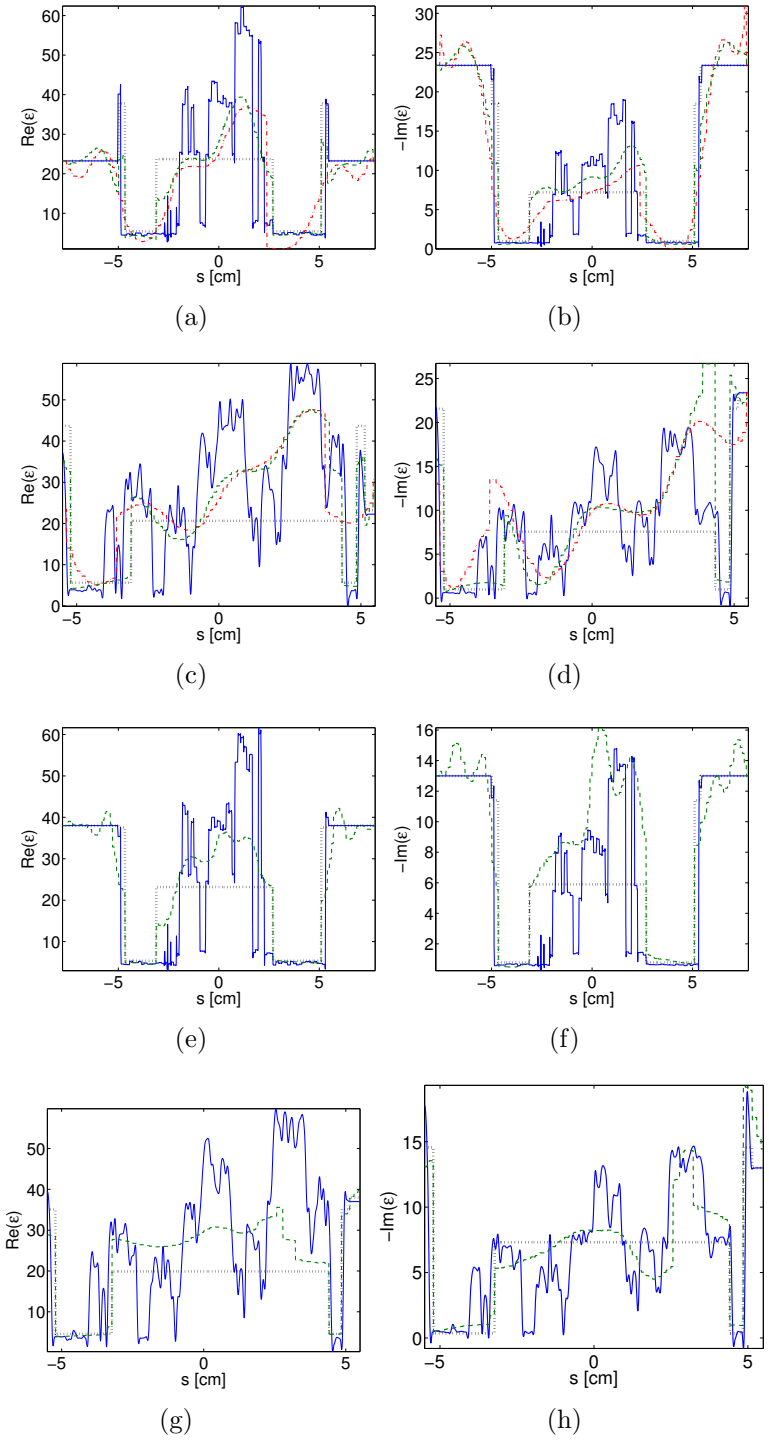

Figure 3.8: *Cross Sections*: Real and imaginary cross sections of Case 1-1 ((a) and (b)), Case 1-2 ((c) and (d)), Case 2-1 ((e) and (f)) and Case 2-2 ((g) and (h)) of images that bisect the tumour. Here s is the distance in cm, the blue solid line represents the phantom, the black line represented by bars is the regional reconstruction, the red line represented by '-.' is the blind inversion and the green dashed line is the reconstruction with prior information. Note the blind inversions are not included at 2 GHz as they are unstable. Images appear in [38]. Used with permission.

uniform. The phantom consists of a skin layer, a fat region, and a fibroglandular region in which a spherical tumour with a 1.5 cm diameter is embedded. The tumour is centred at (1.3 cm, 0.0 cm, 4.4 cm). The 3D phantoms are interpolated on to a 3D tetrahedral mesh, which is used by a 3D FEM forward solver to collect data. These phantoms are simpler than the ones used in the 2D code, because this is the EIL's first pursuit of imaging high contrast biological-type objects in 3D. This 3D phantom is also a numerical representation of a physical phantom at the University of Calgary, and simulation results will be useful in the planning of future experiments.

The 3D radar regional algorithm operates similarly to its 2D analogue. The main difference in the 3D case is that the points that are detected along 2D tissue interfaces form a 3D point cloud to which a closed surface is fit. These surfaces divide the breast into fibroglandular and fat tissue regions, with an assumed uniform skin layer. The dielectric properties of these three regions are approximated using DBIM, where each tissue region is treated as an unknown. The resulting permittivity values of the 3D radar regions are shown in Table 3.4.

3.3.1 3D Tomography Data Collection

When using a first order finite element code, errors can arise due to mesh dependence when collecting forward data. Mesh dependence implies that the mesh

Region	Permittivity
Immersion Medium	24-j1.13
Skin	43.81-j16.11
Fat	4.73-j0.78
Glandular	36.41-j10.13
Tumour	56.62-j17.56

Table 3.3: 3D phantom properties at 1.2GHz.

Region	Permittivity
Immersion Medium	24-j1.13
Skin	42.87-j15.06
Fat	5.67-j0.94
Glandular	28.68-j7.38

Table 3.4: 3D numerical background properties at 1.2GHz.

discretization is not sufficiently fine, and as a result, forward data collected from the same object on a different mesh will produce two unique data sets. This is especially apparent when using a numerical background, because the numerical incident field must be subtracted from the total field, and may be collected on a different mesh. The 3D FEM forward solver is able to collect data from numerical phantoms in two ways. The first is by reading a forward mesh that contains the contours of the dielectric regions of the OI. Each of these regions is assigned a physics number in Gmsh, which is present in the mesh file read by the forward solver. Each physics region is assigned a dielectric property of OI, and a numerical background permittivity. With this option, the physics numbers of the OI and the numerical background must both be present on the forward mesh.

The second option involves a preprocessing step in which both the properties of the phantom and the numerical background can be interpolated on to a general mesh that does not contain any contours. The permittivity values for the phantom and background are sorted in order of mesh elements and read by the forward solver. This is the method used for the 3D breast reconstruction study because this option is less prone to inverse crime and mesh dependency errors.

Although these errors are present in the 2D code, they do not affect data collection and inversion in a significant way. For example, consider the meshes given in Figure 3.9. Mesh (a) contains the OI from which data will be collected, and mesh

(b) contains the numerical background to be incorporated into the inversion as prior information. When inverting with prior information in the 2D case, data are collected from the OI on mesh (a), and then inverted on mesh (b). The incident field is calculated on mesh b. That is, $E_a^{sct} = E_a^{tot} - E_b^{inc}$. These data can be inverted successfully using 2D FEM-CSI in both TM and TE cases with negligible error.

Tomography simulations become considerably more complicated when moving to 3D. The first order 3D FEM code being used to collect forward data can be sensitive to changes in the mesh. As a result, if the approach taken to data collection is the same as in 2D, the scattered field signal required for inversion is substantially lower in magnitude than the noise generated by subtracting data collected on two different meshes. In order to overcome this problem, the OI in mesh (a) and the numerical background in mesh (b) are interpolated on to a general mesh (c), shown in Figure 3.9.

Sensitivity to loss in the immersion medium also increases in 3D. For example, as shown in Figure 3.10, the lossy glycerin-water solution immersion medium that was used in 2D produces a very low received scattered field signal. When solving for 200,000 unknowns in 3D (as compared to 15,000 in 2D), this field magnitude is no longer sufficient to reconstruct the breast properties. This problem is addressed by both reducing the loss in the immersion medium to a complex permittivity of $\epsilon_b = 24 - j1.13$ and imaging the breast inside a perfect electric conductor (PEC) enclosure to eliminate loss due to absorption at the boundaries [45]. The field magnitudes with the low-loss immersion medium, inside the metallic enclosure, are plotted in Figure 3.11 for various frequencies. The plot shows that the received signal is considerably higher than in the high-loss case. The highest magnitude of the scattered field signal occurs at 1.2 GHz. Therefore data is collected and inverted at this frequency to ensure reconstructions with the maximum amount of scattered field information. Although

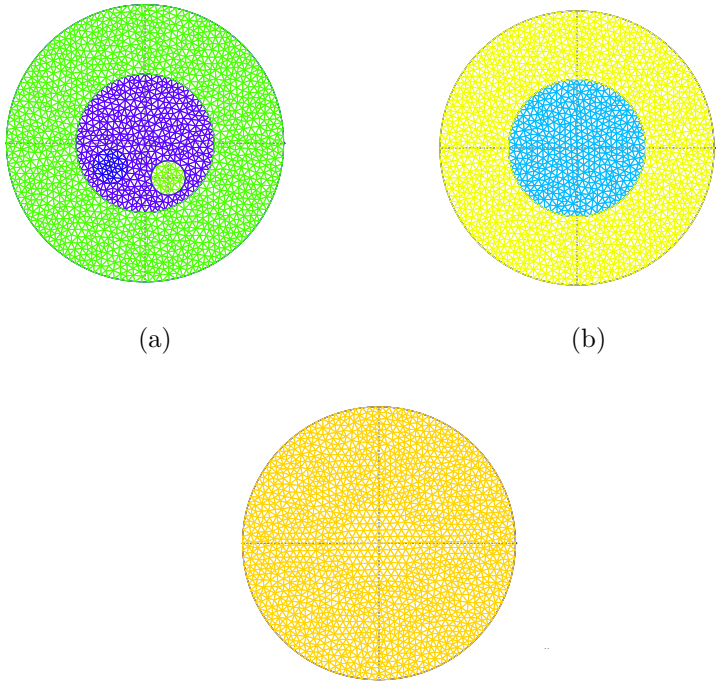

(a) (b)

(c)

Figure 3.9: *Forward problem mesh examples:* The mesh containing the (a) OI and (b) the numerical background are interpolated onto a (c) general mesh in order to reduce errors associated with calculating the incident field on two different meshes.

imaging using absorbing boundary conditions is possible, receiver locations must be carefully considered and related to the OI being imaged. To generalize the imaging chamber, all of the 3D results presented will be for data collected and inverted inside a metallic chamber.

The 3D cylindrical PEC imaging chamber contains 80 receivers and transmitters. The antenna position and polarization are shown in Figure 3.12. The antennas are placed in a circular configuration at a 6.5 cm radius within a 8.0 cm cylindrical metallic chamber in which the top and bottom are also PEC. The circular arrays are placed in 5 layers of 16 antennas with z-coordinates of $z = [-7.00, -5.75, -4.50, -3.25, -2.00]$ cm, where $z = 0$ is the top of the imaging chamber. A z-polarized 3D point source transmits a 1.2 GHz field and the x, y and z field components are received at the antenna locations. The equivalent of 5% noise in the scattered field of the OI, is added to the total field data collected, and a noiseless incident field is subtracted.

3.3.2 3D Inversion and Results

The z component of the data is inverted using 3D FEM-CSI. For this reconstruction, no MR is used. Much like the 2D code, a numerical inhomogeneous background can be incorporated by the user. The numerical background used in the inversion must match the one used in the forward solution. As in the forward solver, this can either be done by assigning the permittivity of the background to physics numbers in the mesh, or from a permittivity map to related to individual mesh elements.

Figures 3.13 - 3.15 c and d show the result of the blind reconstruction in a cylindrical imaging domain. In the images, the black dashed line shows the location of the tumour. The blind reconstructions, which have $L_2 = 37.32\%$, provide no useful diagnostic information. However the algorithm is able to detect some centrally lo-

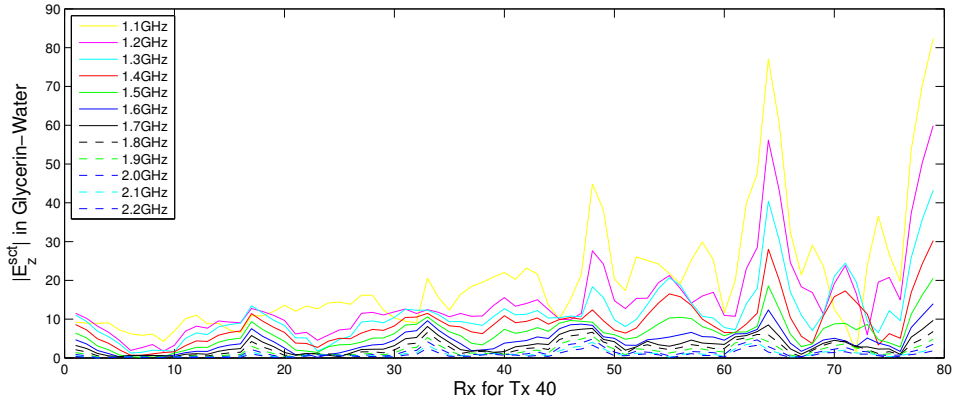

Figure 3.10: Magnitude of E_z^{sct} for multiple frequencies in a lossy glycerin-water solution. Shown here for all receivers of transmitter number 40.

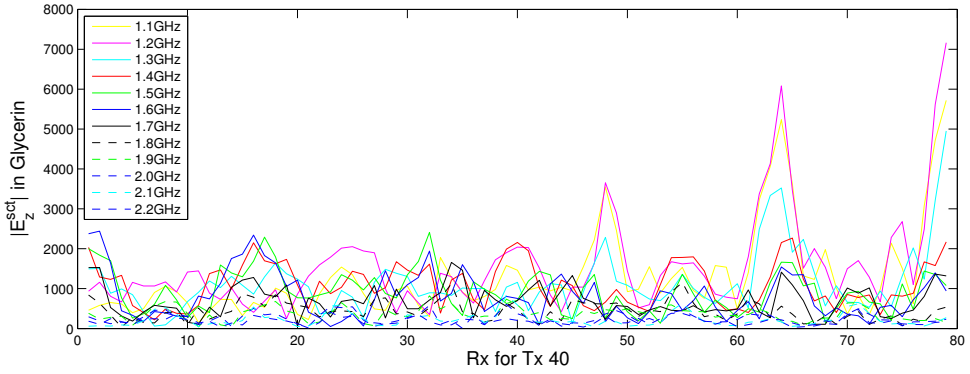

Figure 3.11: Magnitude of E_z^{sct} for multiple frequencies in a low-loss glycerin solution. Shown here for all receivers of transmitter number 40.

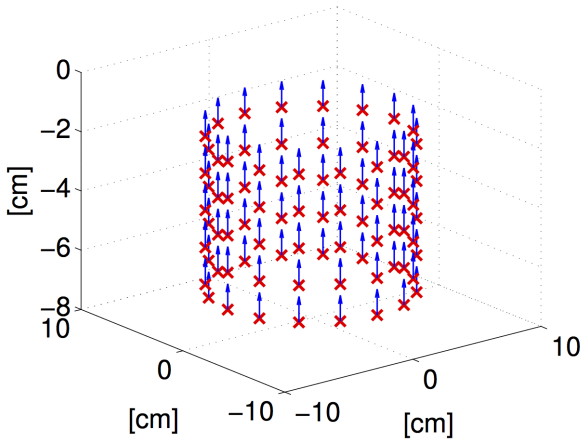

Figure 3.12: Antenna positions and polarizations in 3D chamber.

cated region of high permittivity tissue, possibly corresponding to the fibroglandular region. The outside of the breast is discernible in the image. There are stability problems with the imaginary part of the reconstruction, which present themselves as an ellipsoidal ring of the highest allowed permittivity value (a user defined algorithm constraint). Similar problems with imaginary reconstructions are common in 2D when prior information or regularization is poor.

The radar regions are shown in Figures 3.13 - 3.15 e and f and Table 3.4. The result of using the combined algorithm, which has $L_2 = 25.94\%$, is shown in Figs. 3.13

Actual	Numerical Background	χ_{real}	χ_{imag}
Fat	Fat	-0.1659	0.0007
Fat	Fibroglandular	-0.83	0.01
Fat	Skin	-0.89	0.01
Fibroglandular	Fibroglandular	0.275	-0.020
Fibroglandular	Fat	5.53	0.7
Tumour	Fibroglandular	0.99	0.09
Skin	Skin	0.02	0.01
Skin	Fat	6.97	1.51

Table 3.5: Actual regional contrast values in radar numerical background scenario.

- 3.15 g and h. The real part of the reconstruction is able to detect the location of the tumour. The imaginary part of the reconstruction is not as reliable, since it appears to contain significant imaging artifacts, especially in the skin region. This can once again be attributed a lack of balancing between the real and imaginary variables. The tumour reconstruction results are verified by running the same experiment on a phantom without a tumour. In this case, our results demonstrate that we correctly no longer detect the tumour. The reconstructions, which show the absence of the tumour, are shown in Figure 3.16.

Difficulty reconstructing 3D breast images can be partially attributed to the large number of unknowns in areas of high contrast. Table 3.3.2 shows the actual contrast values for the 3D phantom and the radar numerical background regions. The table shows that errors in the numerical background corresponding to over- or under- estimation of the radar regions result in high contrasts. For example, if the radar region overestimates the fibroglandular region, the algorithm must reconstruct a contrast of $\chi = -0.89 + 0.01$, and if the radar technique underestimates the fibroglandular region, the algorithm must reconstruct a contrast of $\chi = 5.53 + 0.70$. These large contrast values can be difficult for the algorithm to reconstruct, and can divert the solution from one that properly reconstructs the tumour.

3.3.3 Introduction to Tumour Detection Methods

As described for the forearm case in Chapter 2, automated methods for determining tissue regions remove user bias from the detection process. This is also true of tumour detection and monitoring methods. This section describes a basic tumour detection method using the 3D radar region reconstructions, which identifies artifacts in the reconstructions and separates them from the tumour.

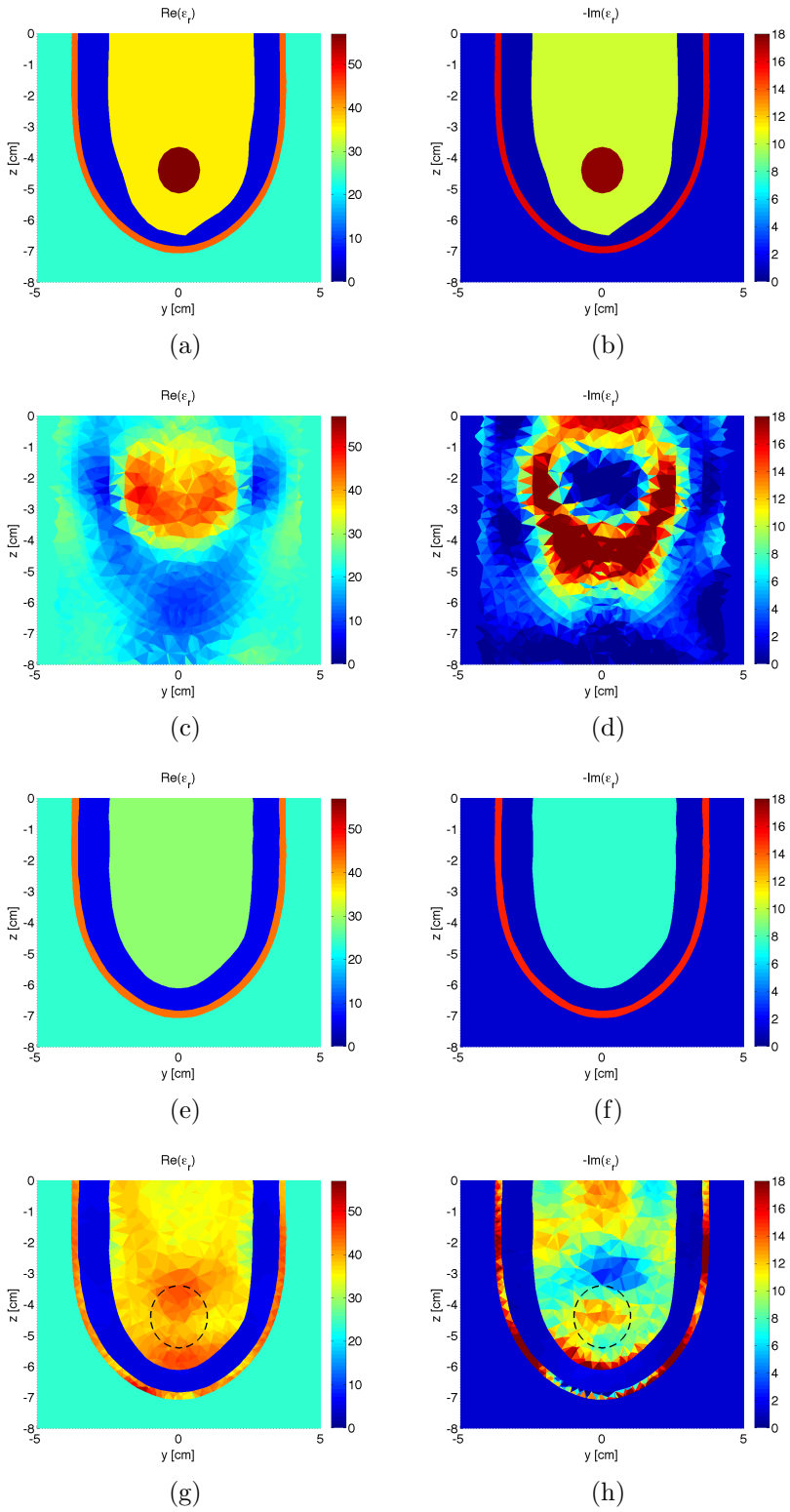

Figure 3.13: *3D Breast Phantom x-slice* (a) and (b): Breast phantom. (c) and (d): Blind reconstruction (e) and (f): Prior information regions obtained from radar-based imaging. (g) and (h): Reconstruction with prior information.

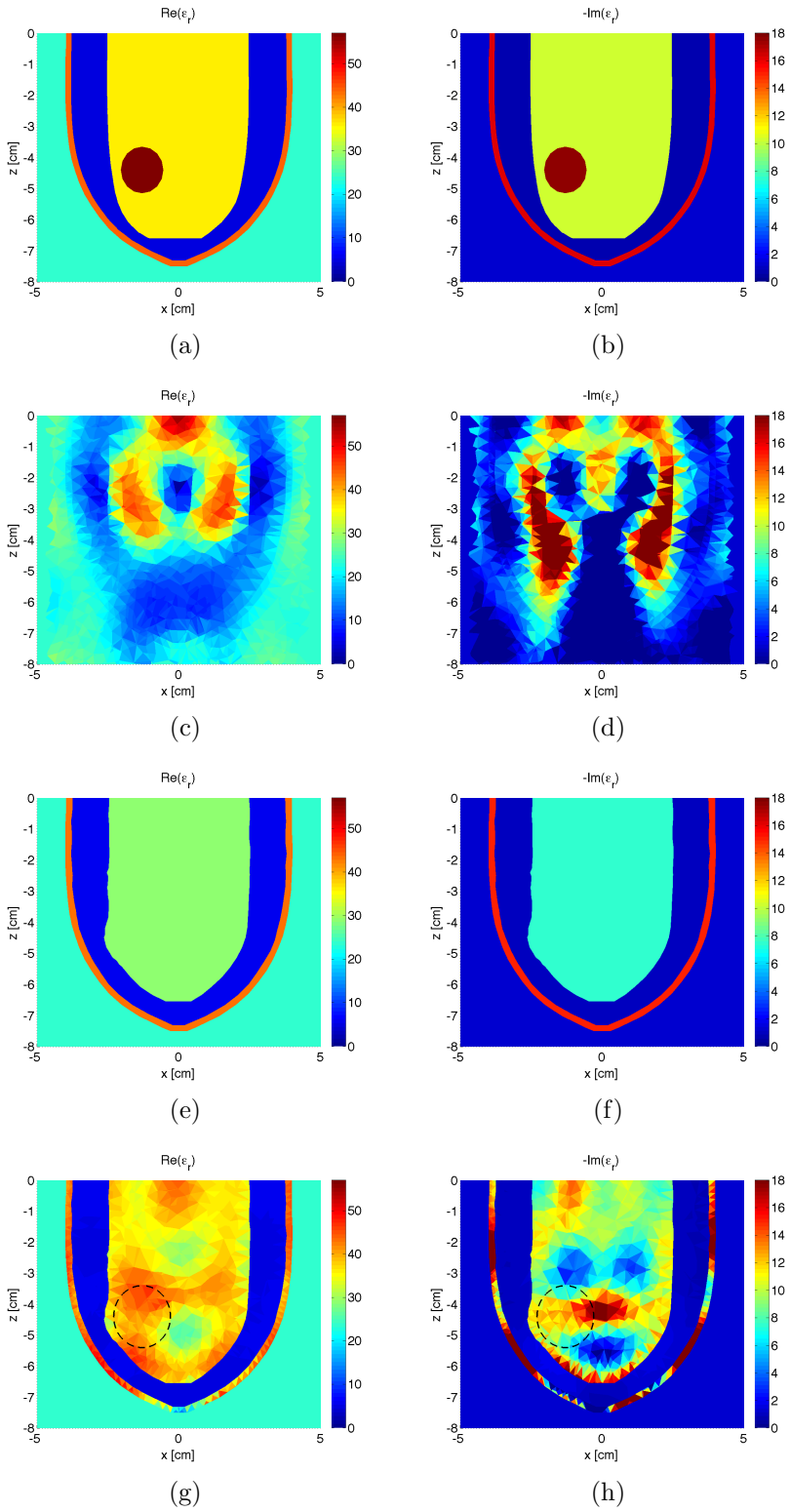

Figure 3.14: *3D Breast Phantom y-slice* (a) and (b): Breast phantom. (c) and (d): Blind reconstruction (e) and (f): Prior information regions obtained from radar-based imaging. (g) and (h): Reconstruction with prior information.

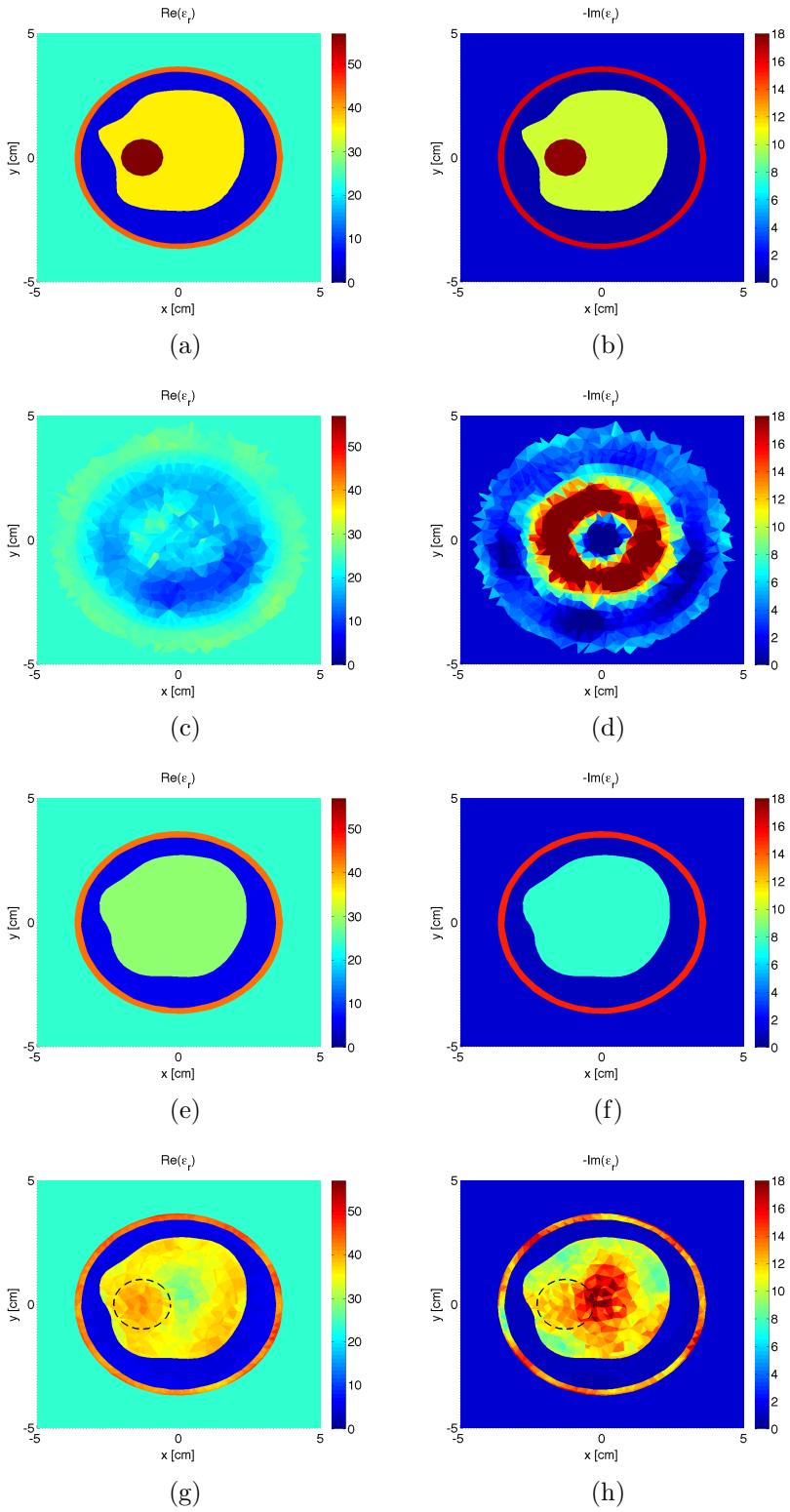

Figure 3.15: *3D Breast Phantom z-slice* (a) and (b): Breast phantom. (c) and (d): Blind reconstruction (e) and (f): Prior information regions obtained from radar-based imaging. (g) and (h): Reconstruction with prior information.

Phantom with tumour and corresponding reconstruction:

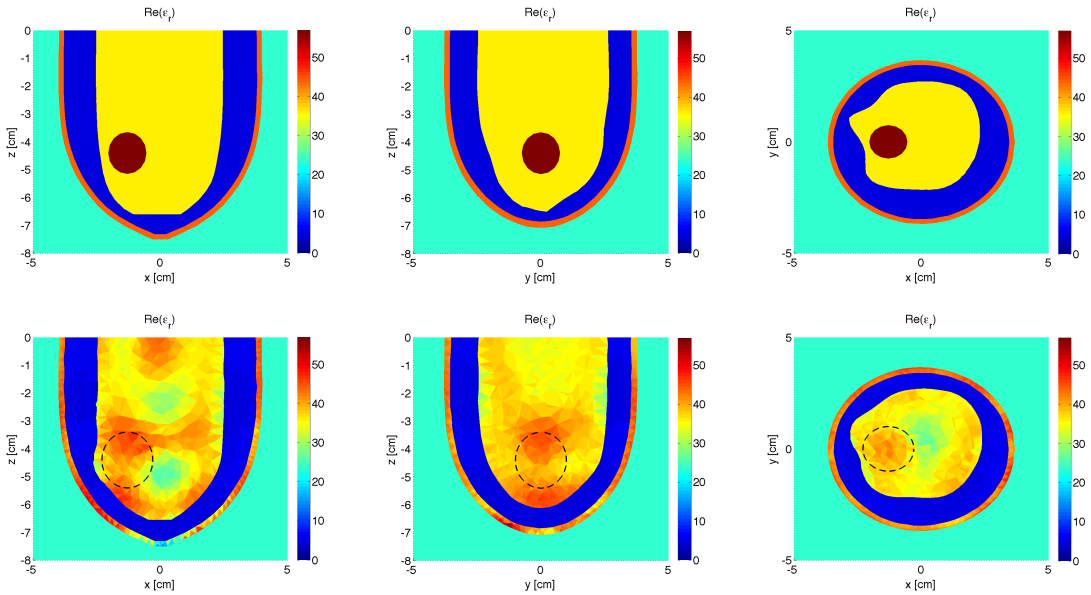

Phantom without tumour and corresponding reconstruction:

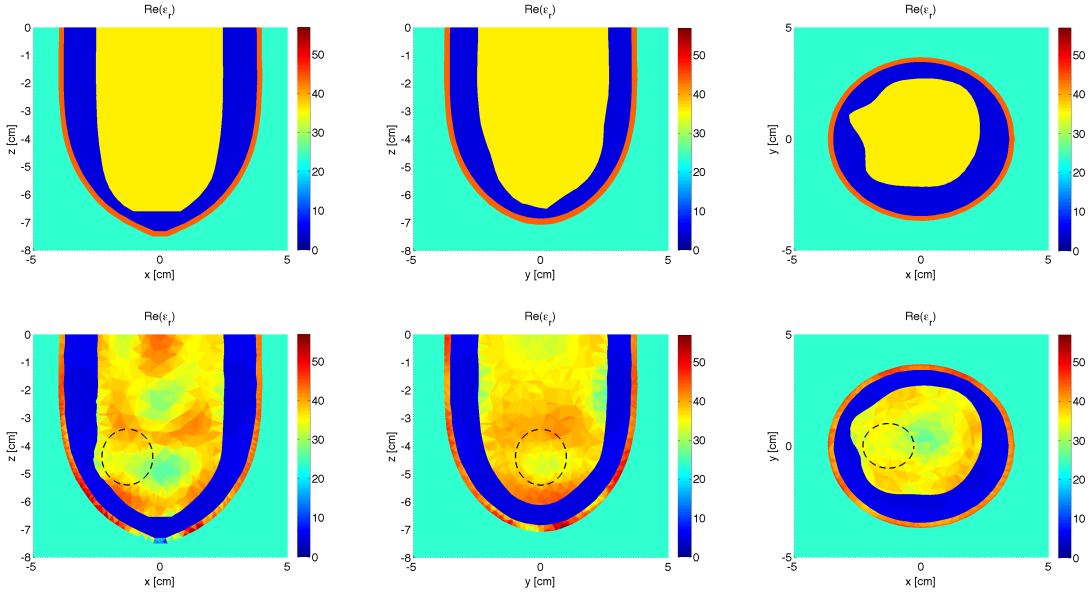

Figure 3.16: *Tumour Detection Confirmation*: Comparison of reconstructions in which the phantom contains and tumour and when it does not. Results show that the detection in the vicinity of the tumour is a positive response and not an imaging artifact.

Using quantitative microwave tomography methods to reconstruct breast images has an advantage in that we know that the largest permittivity value in a breast corresponds to a tumour, if it is present [4]. Even if there are errors in the reconstruction, for example, if the tumour value reconstructed does not reach its known permittivity value, we can conclude that the highest value in the reconstruction likely belongs to the tumour. Unfortunately, imaging artifacts typically present in the higher range of permittivities in the reconstruction also, so when utilizing techniques like thresholding to detect a tumour, these artifacts might appear as a false positive.

Image post-processing procedures can be used to reduce these artifacts and determine the location of the tumour. In this basic technique, the contrast reconstruction is used for detection. Typically, the permittivity is the only quantity displayed when analyzing reconstructions from microwave imaging. However, because CSI is being used, the contrast images can also be viewed, as they provide a unique visualization of the reconstruction. It could be argued that the contrast reconstructions for this breast phantom, shown in Figure 3.17, are more visually useful for tumour detection because the range of the values enhances the tumour more than in the permittivity images. The artifacts are still present in these images, particularly around the lower parts of the fat/fibroglandular interface.

For this detection method, we consider the real part of the contrast image. The first step in the detection process is to determine a reasonable range in which we should find the tumour. As shown in Table 3.3.2, our highest expected contrast value, with the exception of regional errors, should be the tumour. A range within 25% of the maximum contrast values are selected as tumour candidates. These values are displayed as an isosurface in Figure 3.18 a. This figure shows a surface that overlaps with the position of the tumour. However there is also a significant extended

detection below the tumour. This could be confused with a positive response if being used diagnostically. Therefore, a reasonable elimination process must be created to remove this artifact.

To isolate the artifacts, the MATLAB image processing toolbox function *bwlabeln* is used to determine 26-connected regions. Pixel regions that are 26-connected are neighbours to every pixel that touches their face, edge or corner. This tool should locate tumour regions and any extended artifacts. The function determined there were two regions with this connectivity. The MATLAB function *regionprops* is used to analyze the two regions identified by *bwlabel* as potential tumours. The *regionprops* function allows the user to extract the dimensions of a box bounding each of the regions. A bounding box around each object is analyzed, and shows that the object corresponding to the artifact is elongated in the x and y direction, but very short in z. This would not be the feature of a tumour, which has a relatively square bounding box. Figure 3.18 b shows the tumour response in red and the eliminated artifact in blue. Methods to confirm the tumour response are currently being developed and tumour detection using 3D microwave breast reconstructions will be investigated as future work. Diagnostic tools for tumour detection will help make this technology more attractive to clinicians.

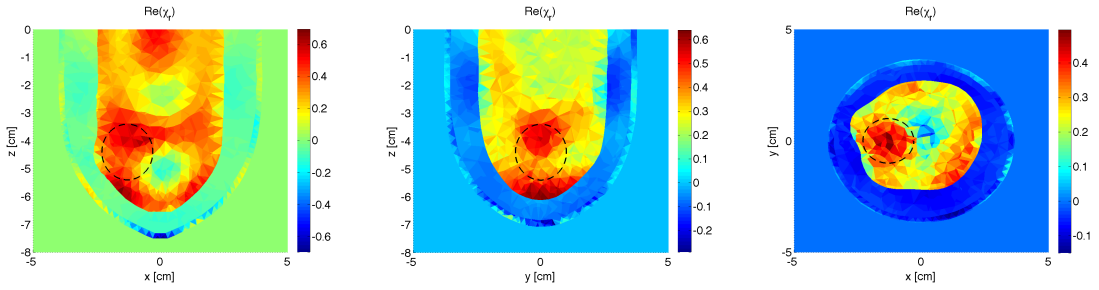

Figure 3.17: Real part of contrast reconstruction used for tumour detection.

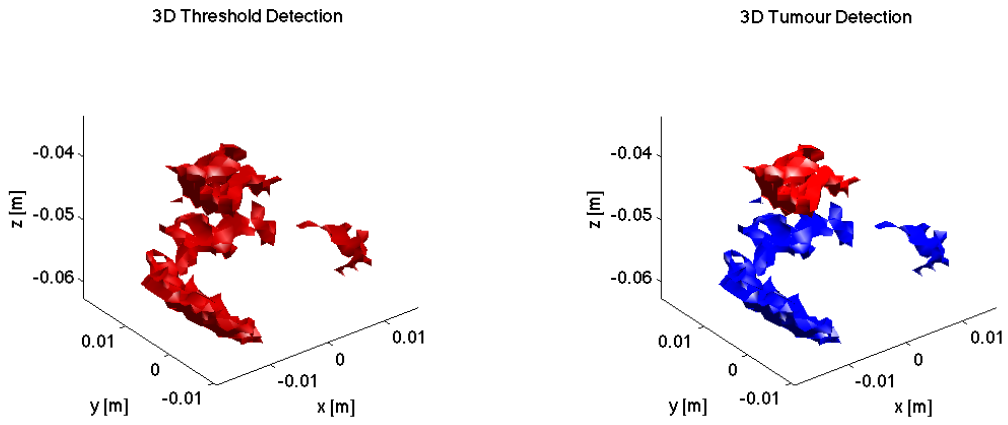

Figure 3.18: Tumour detection isosurfaces using (a) thresholding methods and (b) basic tumour detection.

Chapter 4

Analysis and Applications of Radar/MWT Breast Imaging Algorithm

In this chapter, the potential of the combined algorithm for tumour monitoring during cancer treatment is assessed. Before investigating this application, an evaluation of the role of prior information in FEM-CSI inversions is first performed in 2D and 3D to ensure that using the combined method provides the most accurate reconstructions. Simulated data collected from phantoms with varying tumour sizes are inverted to determine the extent to which tumour size changes can be evaluated.

4.1 Prior Information Study

As mentioned in Section 1.1.2, there have been several ways in which prior information has been used in MWI in order to improve reconstructions and detect

potential tumours. The effect of prior information on FEM-CSI reconstructions is analyzed in a recently submitted paper by D. Kurrant, A. Baran, J. LoVetri and E. Fear titled " Impact of detail in prior information on microwave tomography image quality". Section 4.1.1 summarizes the 2D results from this paper so that they may be expanded on for use in tumour monitoring applications.

4.1.1 Effect of Prior Information on 2D Reconstructions

The impact that prior information has on image quality was first evaluated in 2D using models 1 and 2, introduced in Chapter 3. The goal of the study is to be able to assess structural changes within the breast and detect malignant tumour tissue if it is present. Reconstructions are assessed for four different types of prior information. First, a blind image was reconstructed. Then, prior information cases that included the average properties of the interior, the skin regions and average properties of the interior, and the radar derived regional maps. In the last three cases the imaging domain was restricted to the breast region.

Image Analysis Tools

For this study, a convergence criterion was introduced into FEM-CSI to determine the impact of prior information on algorithm convergence. The inversion algorithm is terminated when the change in the domain cost functional between two successive iterations is less than 0.1%. That is,

$$\% \text{ change in } \mathcal{F}^{\mathcal{D}} = \frac{|\mathcal{F}_i^{\mathcal{D}} - \mathcal{F}_{i-1}^{\mathcal{D}}|}{\mathcal{F}_i^{\mathcal{D}}}, \tag{4.1}$$

where $\mathcal{F}^{\mathcal{D}}$ is the domain cost functional and i is the iteration number.

In order to determine how image quality changes with added prior information,

the breast phantoms and reconstructions were segmented into fat, fibroglandular and tumour tissue regions. The skin was not used for this analysis because it provides little diagnostic information. These regions were segmented using the dielectric property intervals given in Table. 3.1. These segmented regions were used as a binary reference mask for reconstruction analysis. The FEM-CSI reconstructions were also segmented into binary masks using the same regional thresholding technique. We defined the masks as **refmask** and **recmask** respectively. The following metrics were used to evaluate the quality of the image:

The accuracy of the reconstructed geometric properties were qualified using the geometric cross correlation, which is defined as

$$xref_{mask}(\mathbf{refmask}, \mathbf{recmask}) = \frac{(\mathbf{refmask}^T \mathbf{recmask})}{||\mathbf{refmask}||_2 ||\mathbf{recmask}||_2}, \tag{4.2}$$

The geometric cross correlation is a value between 0 and 1, where 0 represents no similarity between the phantom and the reconstructions, and 1 represents a perfect correlation. This metric was used to evaluate the fat and glandular regions.

The proportion of tumour reconstructed (PTR) in the reference mask is given by,

$$PTR(\mathbf{refmask}, \mathbf{recmask}) = \frac{|\mathbf{refmask} \cap \mathbf{recmask}|}{|\mathbf{refmask}|}, \tag{4.3}$$

The PTR is a number between 0 and 1, where 0 is no tumour reconstructed in the known tumour and region, and 1 is a perfect reconstruction.

The correct tumour reconstructed (CTR) measures correctly reconstructed tumour tissue,

$$CTR(\mathbf{refmask}, \mathbf{recmask}) = 1 - \frac{|\mathbf{recmask}| - |\mathbf{refmask} \cap \mathbf{recmask}|}{|\mathbf{refmask}|}. \quad (4.4)$$

The CTR metric is a value between $-\infty$ and 1, where the low end of the scale represents most tumour tissue reconstructed outside of the tumour region, and one represents all of the tumour tissue reconstructed within the tumour region.

Results

The convergence behaviour of the algorithm by iteration (up to 500 iterations) is shown in Figure 4.1 for models 1 and 2, and the iteration at which the convergence criteria is met is shown in Table 4.1. The table shows that with increasing prior information, the convergence criteria was met with fewer iterations. Therefore, increasing the quality of prior information reduces computational time to a solution.

Figure 4.2 shows a plot of CTV vs. PTR for the real and imaginary tumour reconstructions for models 1 and 2. The range of the plots for model 1 and model 2 are different because artifacts are more apparent in model 2. The CTR for the real part of the tumour quantifies the improvement when using the radar regional maps. For example, the real part of the tumour region increases from 0 to 0.96 for model 1 and 0 to 0.95 for model 2. Negative CTR values are observed in the imaginary

Prior Information	Model 1	Model 2
Blind	1200	1150
Average Properties	450	300
Skin Known	500	400
Radar Derived Regions	300	175

Table 4.1: Number of iterations required to satisfy convergence criteria.

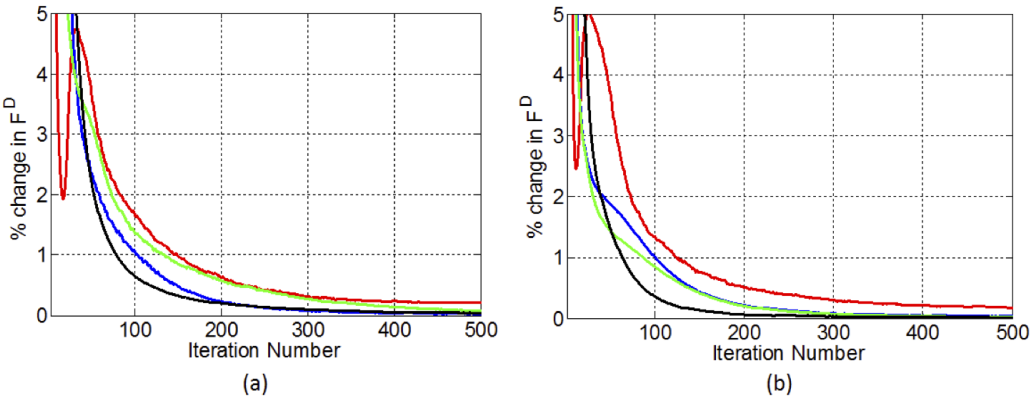

Figure 4.1: Percent change in FD for: Blind reconstruction (red), skin surface regional map (blue), skin region regional map (green), and internal structure regional map (black) for (a) Model 1, and (b) Model 2. Image used with permission from Dr. Douglas Kurrant, University of Calgary.

part, as artifacts present as tumour reconstruction outside of the actual area of the tumour.

Figure 4.3 shows the geometric cross correlation for the real and imaginary parts of models 1 and 2. With this measure, the quality of the reconstruction within the fat and fibroglandular regions is quantified. These results also confirm that the increase in prior information leads to a better reconstruction.

Overall the results from this paper support the use of radar-derived prior information for tumour monitoring applications. In a paper currently in preparation, it was further determined that in 2D reconstructions, it is beneficial to expand the fibroglandular prior information towards the sensors when incorporating the radar regional maps as prior information. This expansion reduces artifacts in the reconstruction and reduces false positives. The effect of this expansion is shown in Figure 4.4. The expanded fibroglandular regions are used for the 2D tumour monitoring application.

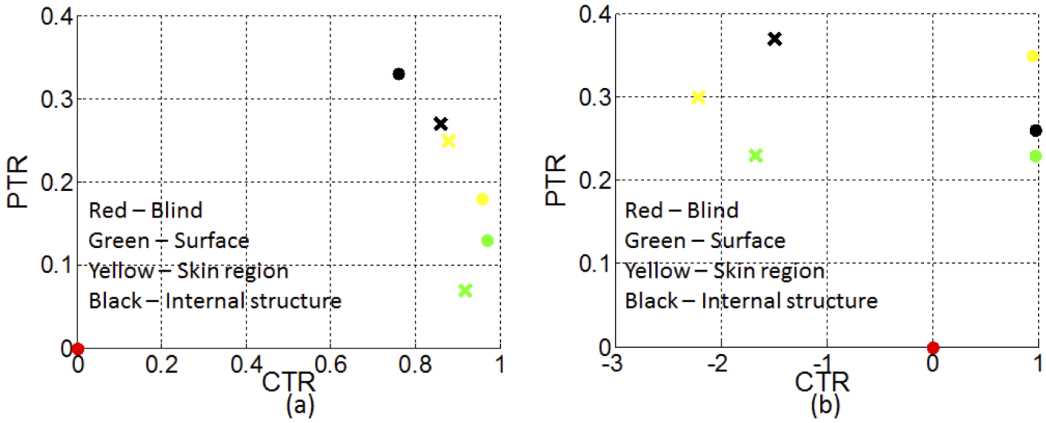

Figure 4.2: CTR-PTR scatter plot of real (circle) and imaginary (cross) part of reconstructed tumour region using different amounts of prior information for (a) model 1 and (b) model 2. Image used with permission from Dr. Douglas Kurrant, University of Calgary.

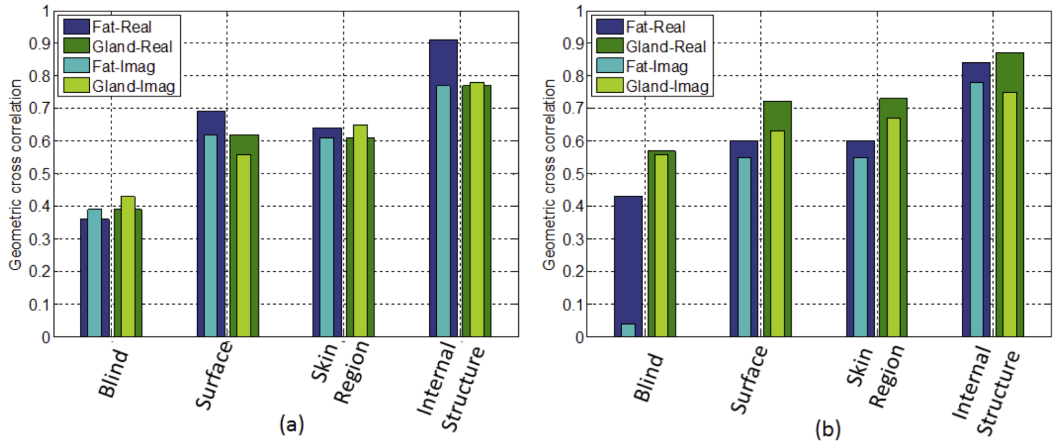

Figure 4.3: Geometric cross correlation of real and imaginary fat (blue/light blue) and glandular (green/light green) tissue regions for models 1 (a) and 2 (b). Image used with permission from Dr. Douglas Kurrant, University of Calgary.

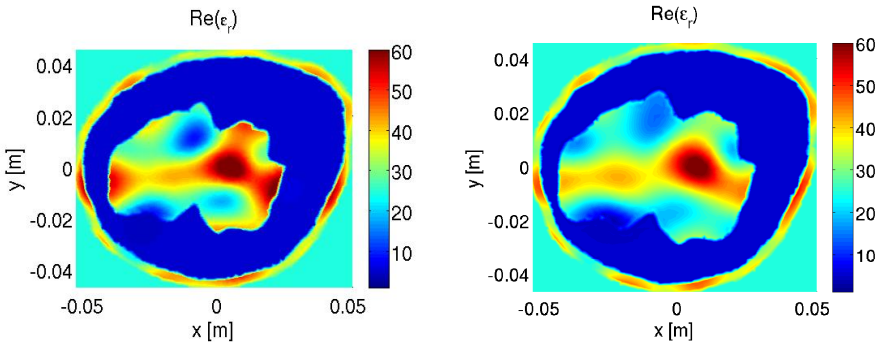

(a) (b)

Figure 4.4: (a) Radar region reconstruction containing artifacts and (b) expanded fibroglandular region reconstruction used to reduce artifacts.

4.2 Tumour Monitoring Using the 2D Combined Method

Physical exams, ultrasound, mammography and MRI are currently used to both detect tumours and assess their size. However, these techniques are not ideal for the monitoring of tumour progress over the course of a chemotherapy treatment. Microwave imaging for tumour monitoring has been described in some reports, and the combined radar/MWT algorithm was investigated for this purpose [26].

Figures 4.5, 4.6, 4.8 and 4.9 show the model 1 and model 2 phantoms with varying tumours sizes, representing what might happen to a tumour over the course of cancer treatment. These figures also show the corresponding blind reconstruction, and the reconstruction with prior information. As the images and the previous section have shown, using prior information from the radar regional map provides a superior reconstruction to blind images or those using lesser prior information. Therefore, this study investigated the clinical use of the radar prior information with expanded fibroglandular regions.

We use the real part of the reconstruction for tumour monitoring purposes. While the imaginary part of the reconstruction is greatly improved when using the radar prior information, the real part is more reliable as it has a greater contribution to the FEM-CSI objective function. In order to detect a tumour, a threshold value of $Re\{\epsilon_{tumour}\} > 43.92$ was applied to the phantom and to the reconstruction. This value is based on tumour dielectric properties provided in [4]. As this technique is being investigated for tumour monitoring during treatment, we can assume that the patient has had high resolution imaging to determine the location of the tumour. Thus, it is valid to assume that the tumour location is known. Therefore, skin tissue and artifacts, which typically have a permittivity above this threshold can be removed due to their location.

Figures 4.7 and 4.10 show the real part of the phantom, the radar prior reconstruction, and an overlap plot of the phantom tumour and the reconstructed tumour. In the tumour plots, light grey represents the actual tumour, grey is the reconstructed tumour, and black is the region of overlap. The figure shows that the reconstructions are able to track the location of the tumour. Although it is not always exact, there is significant overlap between the actual tumour and the reconstruction. The figure also shows that the size of the reconstructed tumour decreases with the size of the actual tumour. This is further supported by Table 4.2, which shows the areas of the actual tumour, reconstructed tumour, and the overlap region. These areas also show that there is a significant overlap between the phantom and the reconstructed tumour, and that changes in size are detectable. There is no false positive detection for either of the models in the case in which the tumour has disappeared. This shows that if prior knowledge of the tumour location is known, the method is not prone to artifacts that can be mistaken for false positives. It should be noted that the tumour recon-

structions do not meet the threshold criteria when this tumour analysis technique is applied to blind images.

4.2.1 Effect of Prior Information on 3D Reconstructions

In 3D, a the effects of increasing the amount of prior information are investigated by examining four cases. First, we examine a blind reconstruction in which no dielectric prior information is provided and the imaging domain is a cylinder, as described in Chapter 3. In the next case the average properties of the interior are known. Then, the skin region and average dielectric properties are known. In the last case, the radar region scenario given in Chapter 3 was used. In the last three cases the imaging domain was restricted to the breast region.

The 3D results show a trend that is similar to the one found for the 2D results, where we found that the results improve as more prior information is added. The real part of the 3D reconstruction results, which show the improvement as more prior information is added, are presented in Figure 4.12 and 4.13. This improvement is supported by the L_2 norms given in Table 4.3, and the geometric cross correlation given in Figure 4.11.

Phantom	Actual Area (cm^2)	Reconstruction Area (cm^2)	Overlap Area (cm^2)
1-1	4.62	1.91	1.73
1-2	2.54	1.66	1.29
1-3	1.10	0.37	0.09
1-4	0	0	0
2-1	6.026	3.47	3.10
2-2	1.93	1.64	1.39
2-3	0.88	0.79	0.61
2-4	0	0	0

Table 4.2: Areas of actual, reconstructed and overlap of tumours using thresholding method.

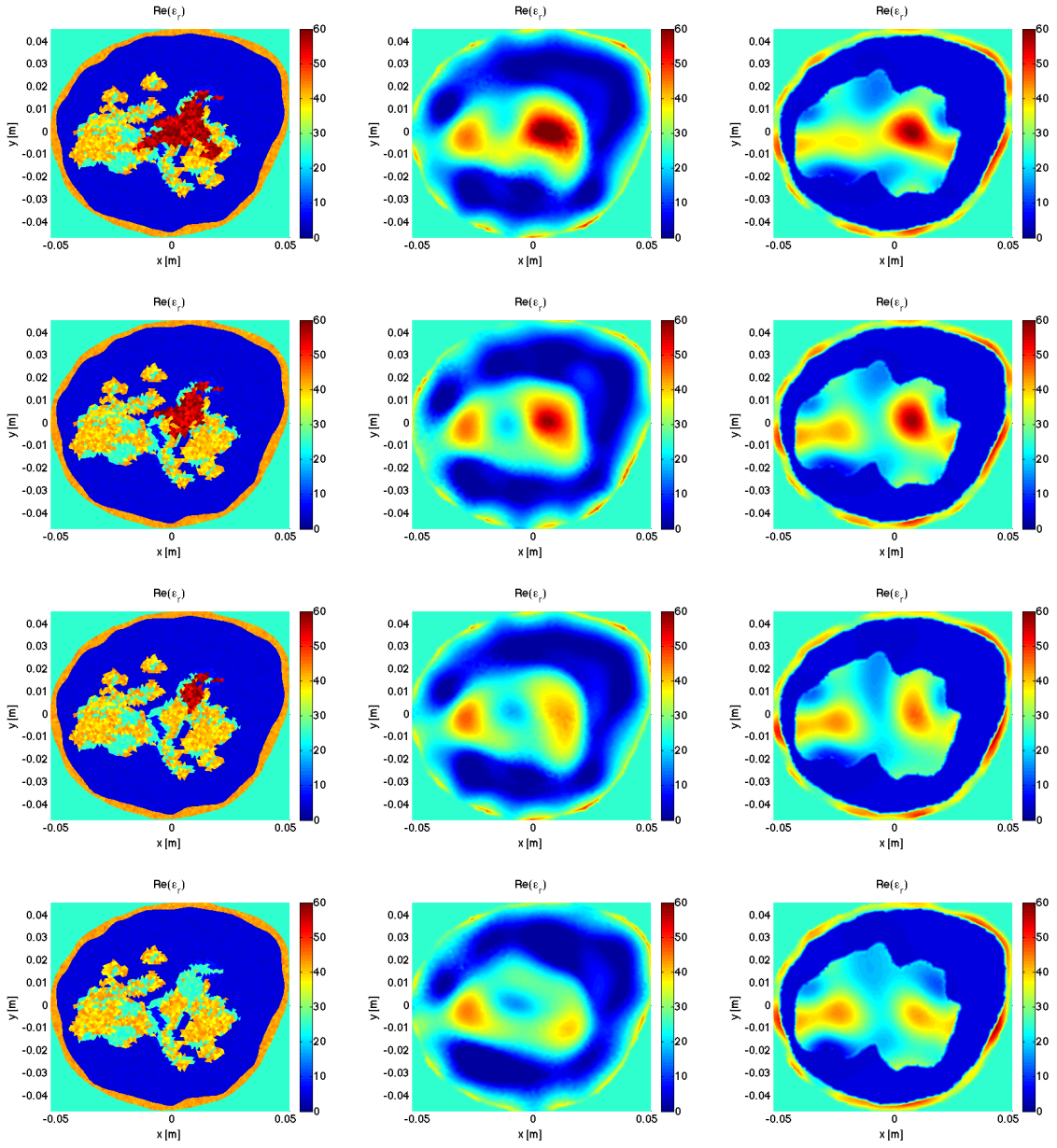

Figure 4.5: Left: Real part of model 1 phantom with decreasing tumour size. Middle: Blind reconstruction. Right: Reconstruction with prior information.

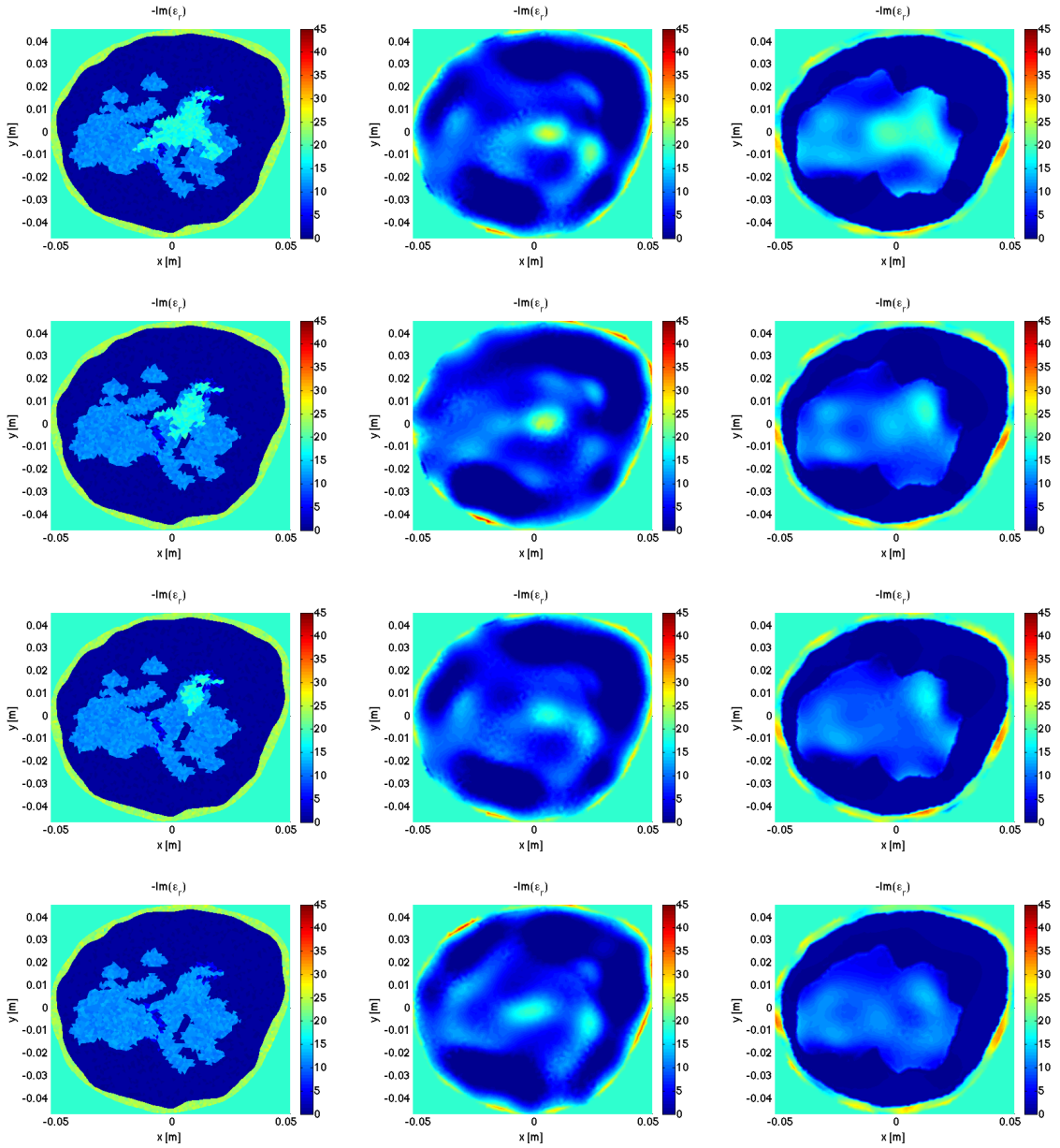

Figure 4.6: Left: Imaginary part of model 1 phantom with decreasing tumour size. Middle: Blind reconstruction. Right: Reconstruction with prior information.

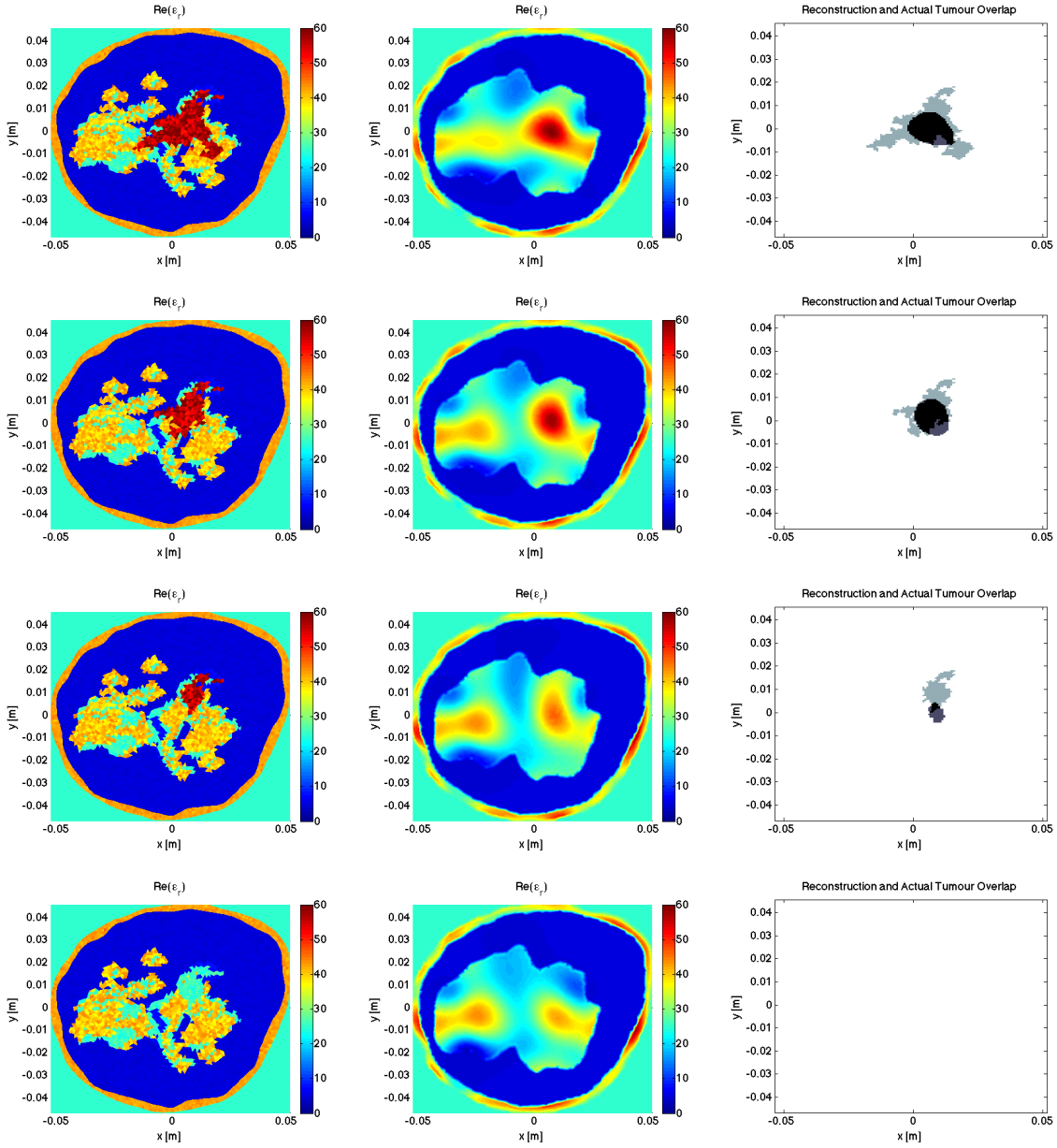

Figure 4.7: Left: Real part of model 1 phantom with decreasing tumour size. Middle: Reconstruction with prior information. Right: Actual tumour and reconstructed tumour overlap plot. Here light grey is the actual tumour, grey is the reconstructed tumour, and black is the region of overlap.

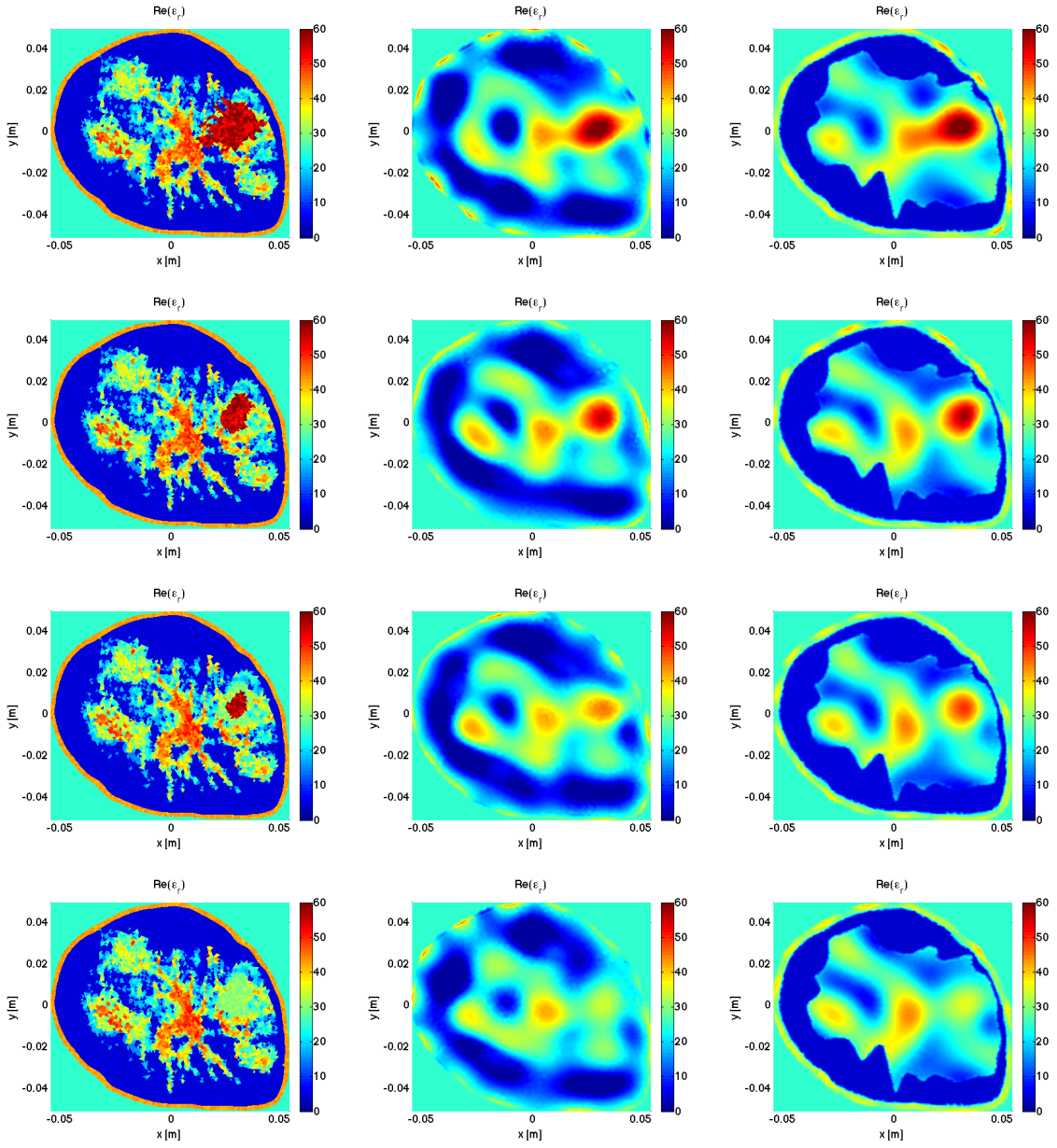

Figure 4.8: Left: Real part of model 2 phantom with decreasing tumour size. Middle: Blind reconstruction. Right: Reconstruction with prior information.

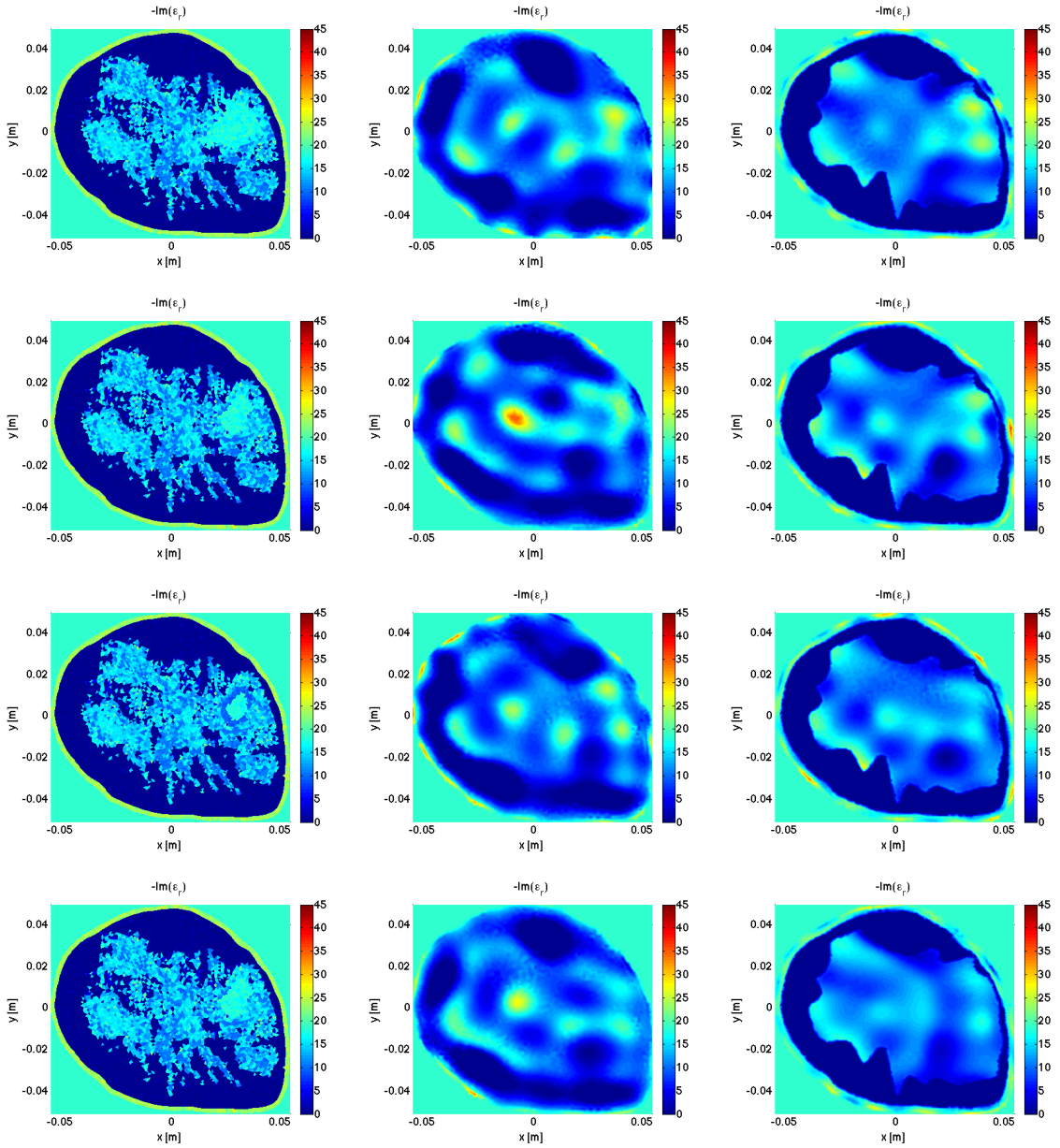

Figure 4.9: Left: Imaginary part of model 2 phantom with decreasing tumour size. Middle: Blind reconstruction. Right: Reconstruction with prior information.

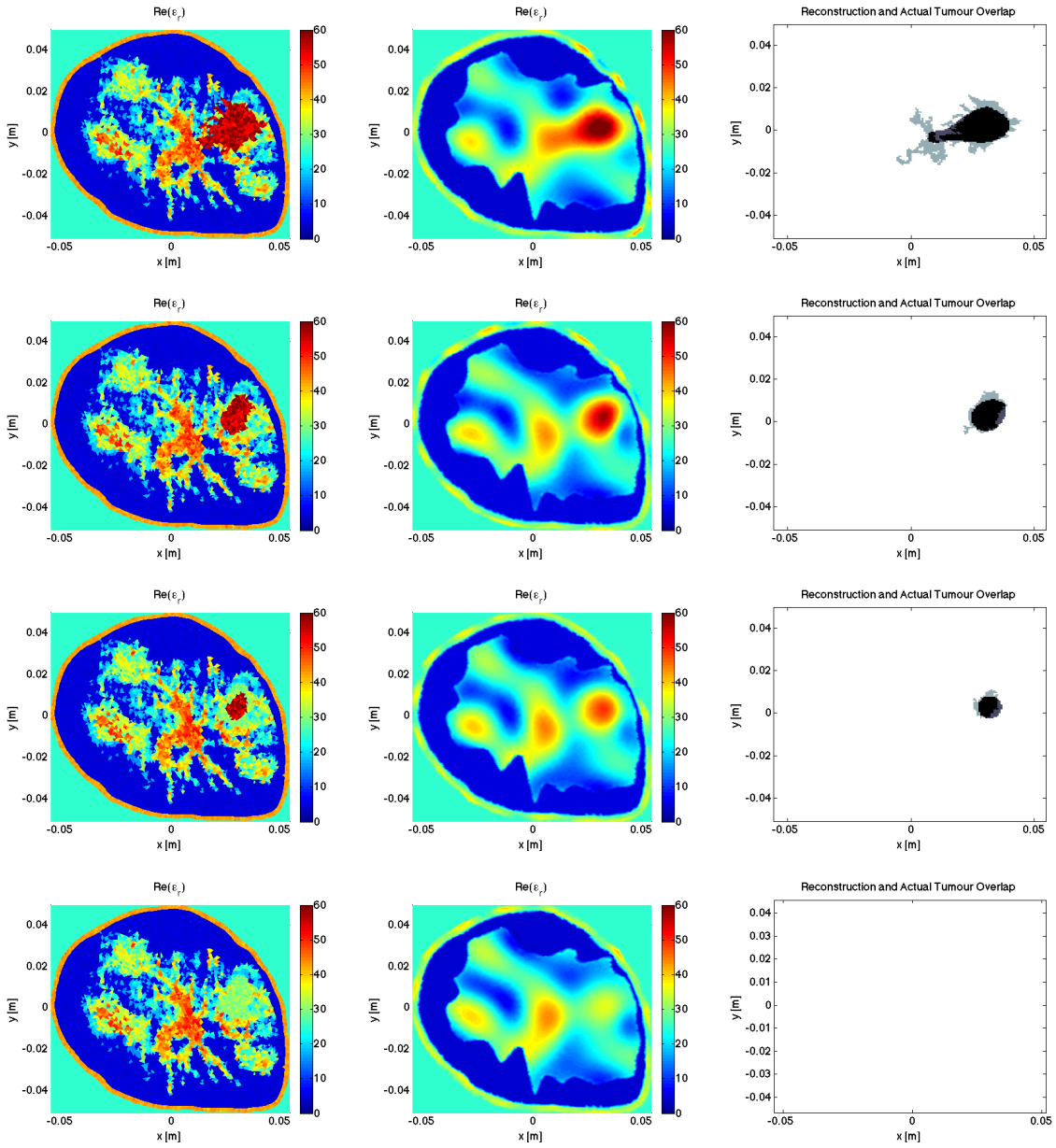

Figure 4.10: Left: Real part of model 2 phantom with decreasing tumour size. Middle: Reconstruction with prior information. Right: Actual tumour and reconstructed tumour overlap plot. Here light grey is the actual tumour, grey is the reconstructed tumour, and black is the region of overlap.

Prior Information	L_2
Blind	41.41%
Average Properties	41.32%
Skin Known	35.25%
Radar Derived Regions	20.22%

Table 4.3: 3D L_2 norms for different types of prior information.

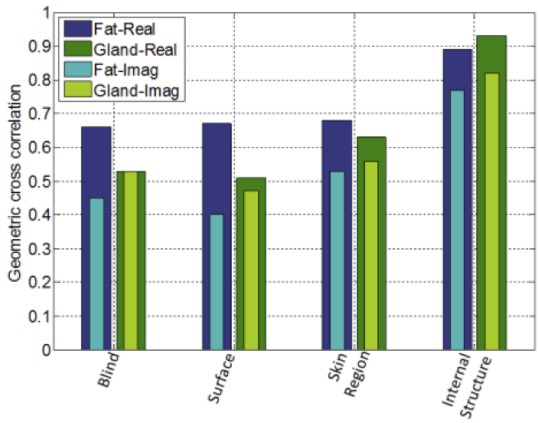

Figure 4.11: Geometric cross correlation of real and imaginary fat (blue/light blue) and glandular (green/light green) tissue regions for 3D model. Image used with permission from Dr. Douglas Kurrant, University of Calgary.

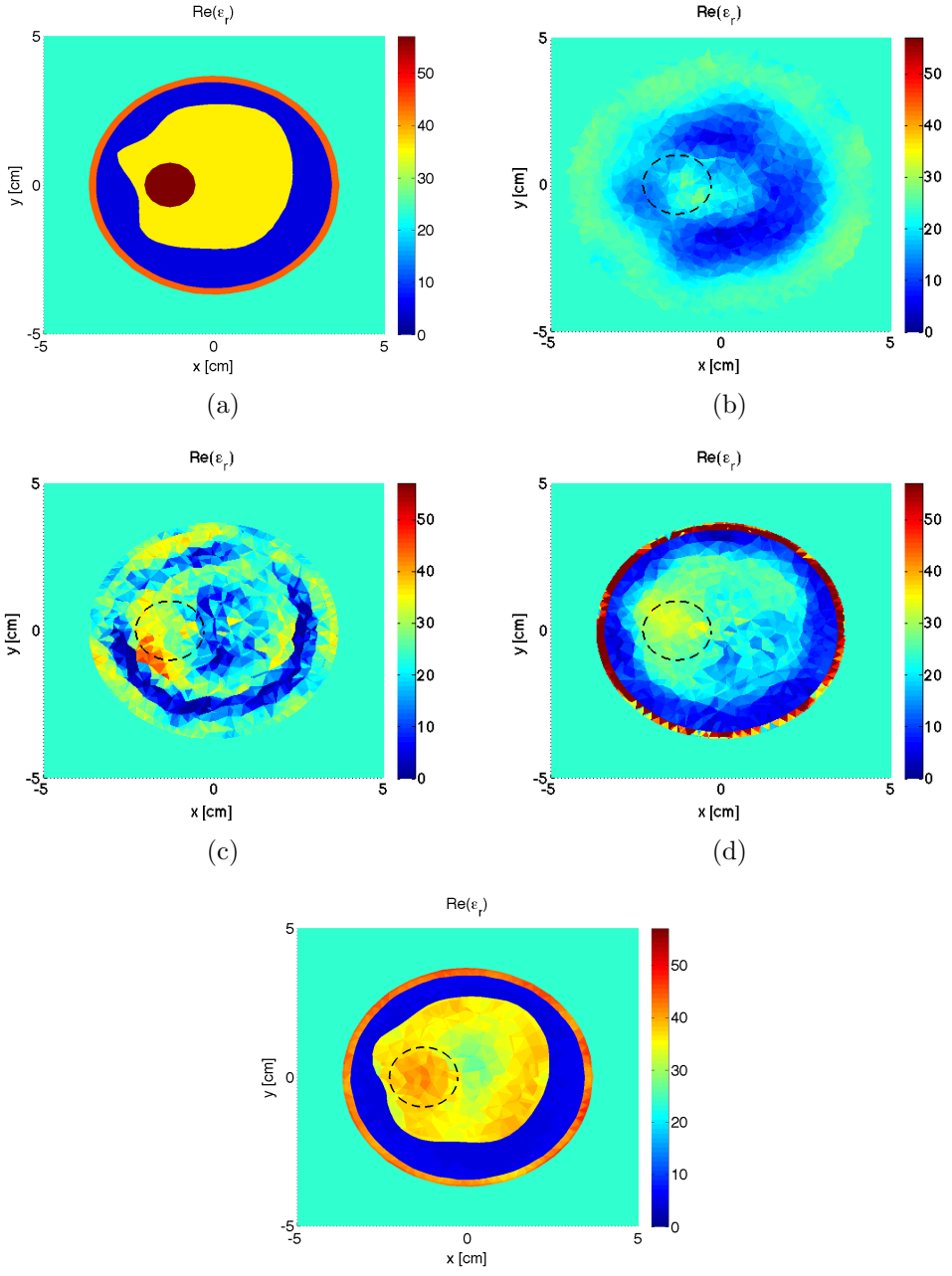

Figure 4.12: Real part of 3D z-slice reconstructions using increasing amounts of prior information. Images show (a) the 3D phantom, (b) blind reconstruction, (c) average property reconstruction, (d) average property and skin reconstruction and (e) radar region reconstruction.

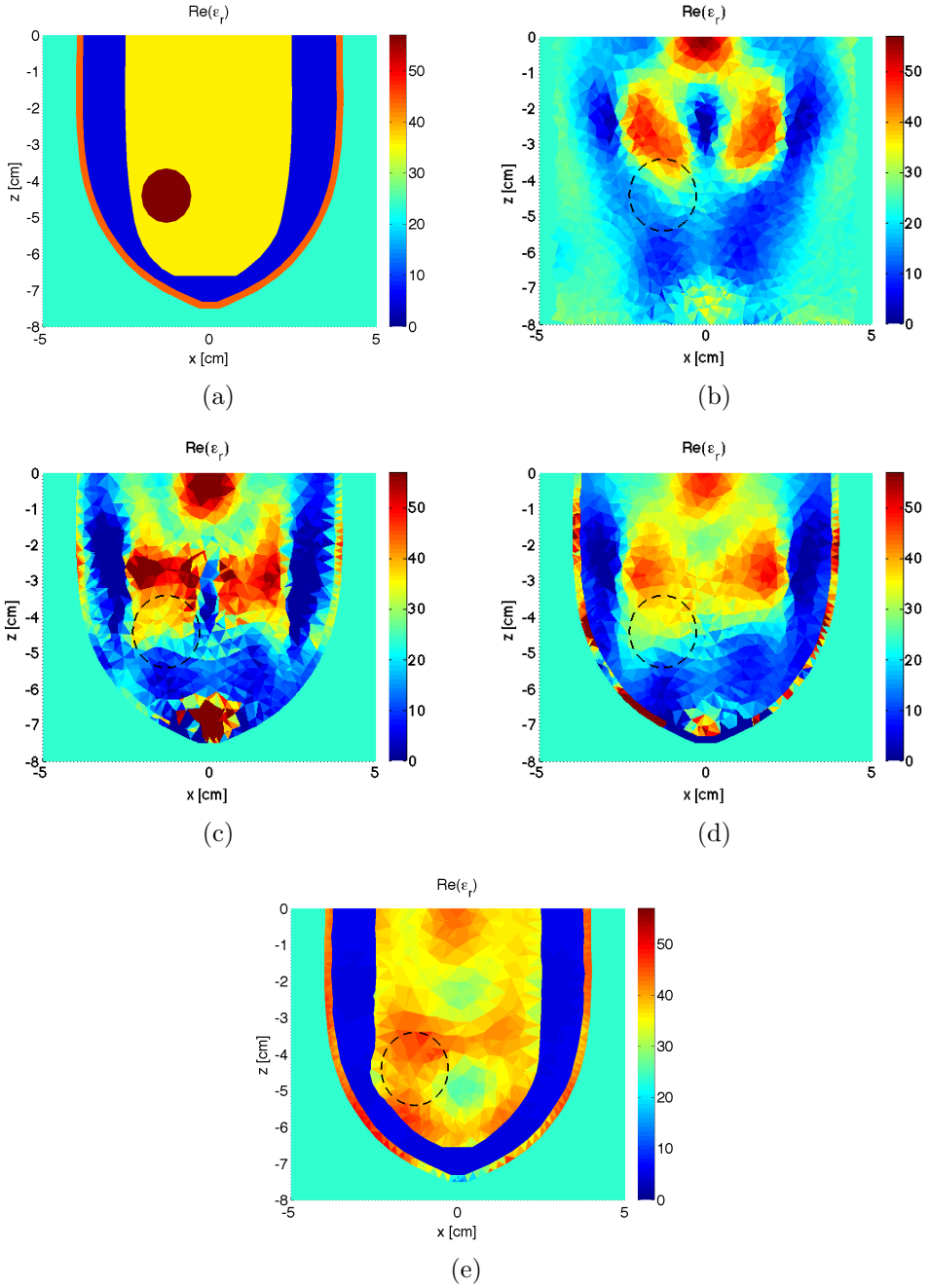

Figure 4.13: Real part of 3D y-slice reconstructions using increasing amounts of prior information. Images show (a) the 3D phantom, (b) blind reconstruction, (c) average property reconstruction, (d) average property and skin reconstruction and (e) radar region reconstruction.

Tumour monitoring in 3D

We have performed a preliminary analysis of the tumour monitoring potential of the 3D combined algorithm. The same thresholding technique used in the 2D case was applied to the real part of a 3D reconstruction, one of which contains a tumour and one in which no tumour is present. The results of the threshold detection are shown in Figure 4.14, where the tumour region is indicated with the dashed circle. The figure shows that, although we were able to detect some regions within the tumour that satisfy the thresholding criteria, it does not accurately represent the 3D phantom tumour.

Techniques for 3D tumour monitoring will be investigated as future work. The detection may be improved by increasing the amount of receivers around the location of the tumour, since we assume that we know the location of the tumour from an earlier scan. Another option may be to reduce the thresholding level, but this would have to be done is such a way that the choice is not ad-hoc, but represents a reasonable approximation of tumour tissue. Note the skin and artifact responses are still present in the 3D images.

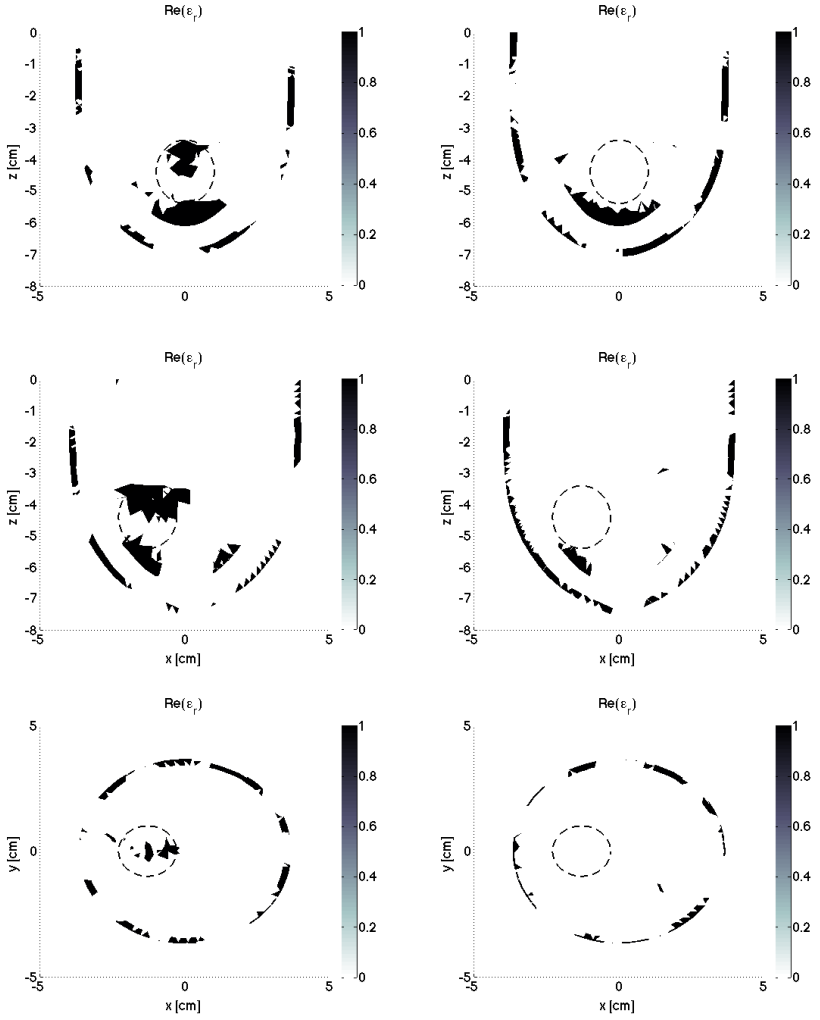

Figure 4.14: Thresholding detection method applied to 3D phantoms left: with a tumour, right: without a tumour.

Chapter 5

Immersion Medium Independent Inversion Algorithm

This chapter demonstrates that when using high quality prior information such as the radar-derived tissue regions presented in Chapter 3, the inversion is significantly regularized to the point where imaging can be done in any immersion medium. Results are presented for reconstructions that utilize a general numerical background, and show that a user defined numerical background permittivity can be used to regularize the problem and significantly improve the quality of microwave breast reconstructions.

The immersion medium in a MWI system is typically chosen to maximize interrogation energy into the breast. However, the technique and results presented in this chapter will show that FEM-CSI can be made independent of the physical background medium by introducing a numerical background permittivity into the contrast function. This independence from the physical medium allows for a considerable amount of flexibility when designing an experimental or clinical imaging system. For example, immersion fluid can be chosen based on factors such as ease of use and wavelength

within the medium, which dictates antenna placement and spacing in the imaging system.

Results are shown for a variety of immersion media. A novel march-on-background technique in which an OI is reconstructed from data collected in multiple immersion media is presented.

5.1 Matching Fluids in Microwave Imaging

The immersion medium, also referred to as a "matching fluid", "matching medium" or "immersion fluid", has a significant impact on the microwave breast imaging problem. The primary goal when choosing an immersion medium is to match the properties of the fluid to the properties of the breast in order to minimize reflections from the breast surface, and maximize interrogation energy. The matching of properties ensures that a tumour that is embedded in the breast has a maximum potential contribution to the overall scattering of the object. If the information received from the tumour is maximized, this provides a greater chance of accurately determining the tumour's properties and location. This is also true of the fibroglandular tissue, where optimal interrogation energy allows for the reconstruction of details within the breast, and potentially improves the delineation between the tumour and fibroglandular tissues.

There have been a number of studies investigating the impact of the matching fluid on reconstructions at microwave frequencies. For example, [46] studies the dependence of experimental forearm reconstructions on loss in the immersion medium. By slowly adding salt to water to increase its conductivity, it is demonstrated that reconstructions suffer for low and high loss fluids. In [47], immersion fluids with properties similar to that of breast tissues are evaluated for their effect on system performance

and breast imaging using microwave radar techniques. [2] suggests that in order to obtain the best images using microwave tomography, the matching medium should be patient specific - matching the average properties of the fat and fibroglandular tissues in the patients breast.

It is clear that the immersion medium plays an important role in the quality of reconstructed images. However, there are many competing factors to consider besides the interrogation energy when deciding on which medium to use. For example, the wavelength of the incident field and antenna type, size and dynamic range are all dictated by the complex permittivity of the immersion medium. These factors determine the resolution limits of the reconstruction, and the sensitivity to small scatterers in the OI. The antenna of choice must also be operable in the chosen immersion liquid. Antennas might be chosen based on their size, as smaller antennas could collect more independent data within the imaging chamber, reducing the under determinedness of the inverse problem.

Ease of use is an important factor when working with these fluids in a lab or clinical setting. The fluid should be environmentally friendly, easy to dispose of, and patient friendly in that it is non-toxic and easy to clean. Air ($\epsilon_b = 1 - j0$) is the ideal fluid choice for ease of use and patient comfort. However, it is a challenge to reconstruct images in this medium because of the high contrast between air and breast tissue. This high contrast also means that the breast surface will reflect a considerable amount of the incident radiation, reducing the amount of interrogation energy.

The following section shows how the combined radar/MWT algorithm motivated the use of FEM-CSI as an immersion medium independent algorithm. This algorithm allows us to make design decisions based on number of receivers and transmitters in

an imaging chamber, ease of use, etc., rather than on interrogation energy alone, because it utilizes a numerical background in order to reduce the contrast in the imaging domain, thereby making the inverse problem easier to solve.

5.2 Immersion Medium Independent Combined Algorithm

Chapter 4 showed that the quality of a FEM-CSI reconstruction depends on the amount and quality of the prior information used. Basic and easily obtainable prior information, such as restricting the imaging domain to the breast region, helps to mitigate the ill-posedness of the inverse problem. However, the use of high quality prior information such as the radar-derived regional map greatly improves reconstructed images. We have found that using high quality prior information in the numerical background has a unique benefit in that it allows the algorithm to reconstruct the breasts interior in immersion media ranging from air ($\epsilon_b = 1 - 0$), to water ($\epsilon_b = 79 - j4.5$), with varying losses.

Five commonly used (experimental and/or synthetic) immersion media are selected for this study: air, oil ($\epsilon_b = 5 - j1$), two water-glycerin solutions ($\epsilon_b = 24 - j18$) and ($\epsilon_b = 39 - j13$), and water. Inversions are performed in a completely blind scenario to provide a rigorous methodology to compare the images generated from this study. The only quantity known in this case is the permittivity of the immersion medium. The imaging domain is taken to be the entire computational domain. The results of these blind inversions are shown in Fig. 5.1.

The figure shows that when inverting in air, the breast location is not detected in the real part of the reconstruction, and there is a minimal detection in the imaginary

part. When inverting in oil, reconstructed features are present in both the real and imaginary part, but there is no distinct location of the breast itself or its constituent tissues. Neither of these reconstructions provide useful diagnostic information. The inversion in the glycerin solution 1 shows the breast location with a blurred edge. There is delineation between the fat, fibroglandular and tumour regions in both the real and imaginary reconstruction. While the location of the tumour is not accurate, it is significant that the reconstruction algorithm detects a tumour within the breast. This particular glycerin-water solution is used frequently in breast microwave imaging because of its close match the the average properties of breast tissue. The glycerin-water solution 2, and water on its own, produce unstable results, and while the location of the breast is determined, the images are spurious and contain no reliable information.

The lack of prior information and the large imaging domain in the blind images are unrealistic. Image domain restriction to a known region around the object of interest is very common in MWT, and this information can be obtained using approximations or by using a laser to find the exterior of the OI. The number of unknowns in the problem is vastly reduced by restricting the imaging domain to the location of the breast. Fig. 5.2 shows that this technique allows for a significant improvement in the quality of the reconstructions. The quality of these imaging domain restricted reconstructions is determined by the L_2 error norm, given in Table. 5.1.

In the previous case, reconstructions of the breast in the air and oil immersion media were not possible. With the imaging domain restriction, distinct tissue regions emerge in the real part for both of these immersion media. The specific tissue regions are apparent, including the tumour, which is accurately reconstructed in both dielectric property and location. The quality and similarity between these two recon-

structions is reflected in their L_2 error norm. Glycerin solution 1 provides the best reconstruction as determined by the L_2 norm. As in the other cases, the real part of the reconstruction delineates the tissues and provides an accurate tumour reconstruction. The blurriness present in the air and oil reconstructions are not apparent in this case, and there is much more uniformity within the individual tissue regions. The reconstructions in the glycerin solution 2 and in water once again produce an unstable result with no usable information. In all of these cases, the imaginary part of the reconstruction is not accurately reconstructed due to a lack of balancing between the real and imaginary contrast within the FEM-CSI code.

The next set of images to be considered utilizes the radar-derived prior information regions. These prior information regions are applied to the data collected in the various immersion media and are shown in Fig. 5.5. All of the images with prior information are high quality reconstructions. It is difficult to visually differentiate between the real parts of the reconstruction, but it is in the imaginary part that we see the most dramatic effect. Solutions from air, oil and both glycerin-water solutions show the tumour as two distinct dielectric objects. However the imaginary reconstruction in the water immersion medium shows a single mass at the tumour site, accounting for the improvement in the L_2 norm given in Table. 5.1. The tissue regions provided as prior information allow the FEM-CSI to converge to a similar, and accurate solution. In this case, the radar regions also provide enough regularization to balance the imaginary part of the complex permittivy, allowing tumour tissues and details within the fibroglandular region to appear. The L_2 error norms after the addition of the radar-derived prior show the opposite of what we observe in the blind case. The prior information not only stabilizes the solution in glycerin-water solution 2 and water, but the resulting reconstruction is a 7% improvement over the

previously best glycerin-water solution 1 in the glycerin solution 2 case and a 20% improvement in the case of water. The trend is interesting because these immersion media are displayed in order of decreasing incident wavelength. As wavelength gets shorter, the resolution of the image improves, as we are observing here. These results show that with enough high quality prior information, inversions should be possible in any reasonable immersion medium.

5.3 Immersion Medium Independent Imaging with FEM-CSI

The results presented so far have shown that both imaging domain restriction and high quality prior information allow imaging in immersion media with a large range of permittivity values. However, high quality prior information is not limited to the radar-derived regions that were presented in the previous section. In fact, any prior information that is incorporated into FEM-CSI in the form of an inhomogeneous numerical background is useful if it reduces the contrast in the imaging domain, thereby making it easier for CSI to converge to an accurate solution.

The flexibility of the inhomogeneous background in FEM-CSI allows the user to define a numerical background of their choice, with the hope of improving the resulting reconstruction. Before moving forward, it is helpful to reiterate the difference between the background types that have been discussed. Here ϵ_b is used to refer to the *physical*

	Air	Oil	Glycerin Sol 1	Glycerin Sol 2	Water
L_2	60.54%	56.98%	43.79%	132.02%	134.22%
L_2^{Prior}	48.73%	47.48%	57.84%	36.63%	23.71%

Table 5.1: L_2 norm errors for various immersion media, with and without a numerical radar region background.

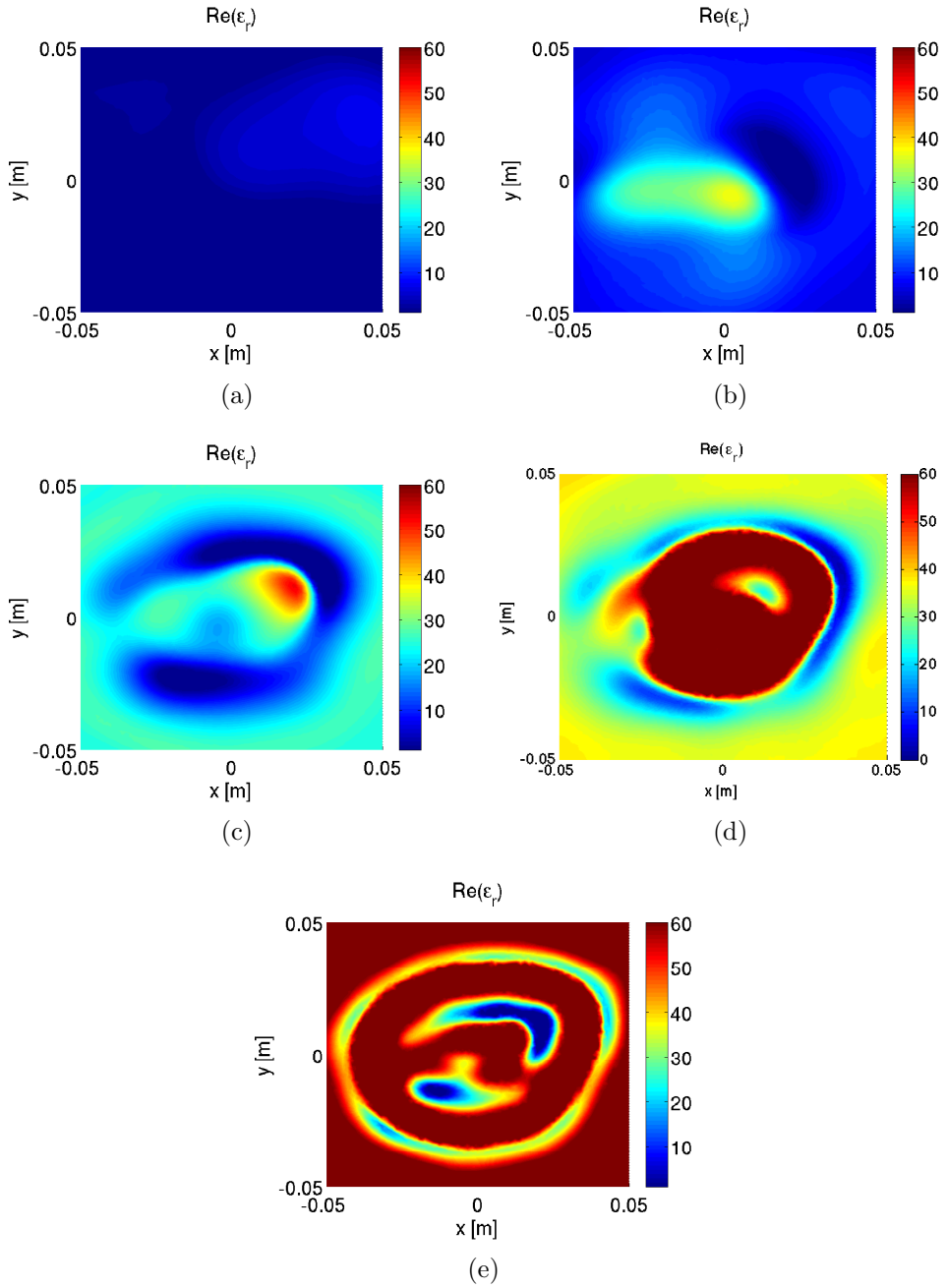

Figure 5.1: Real part of blind reconstructions in (a) air, (b) oil, (c) glycerin solution 1, (d) glycerin solution 2, and (e) water immersion media.

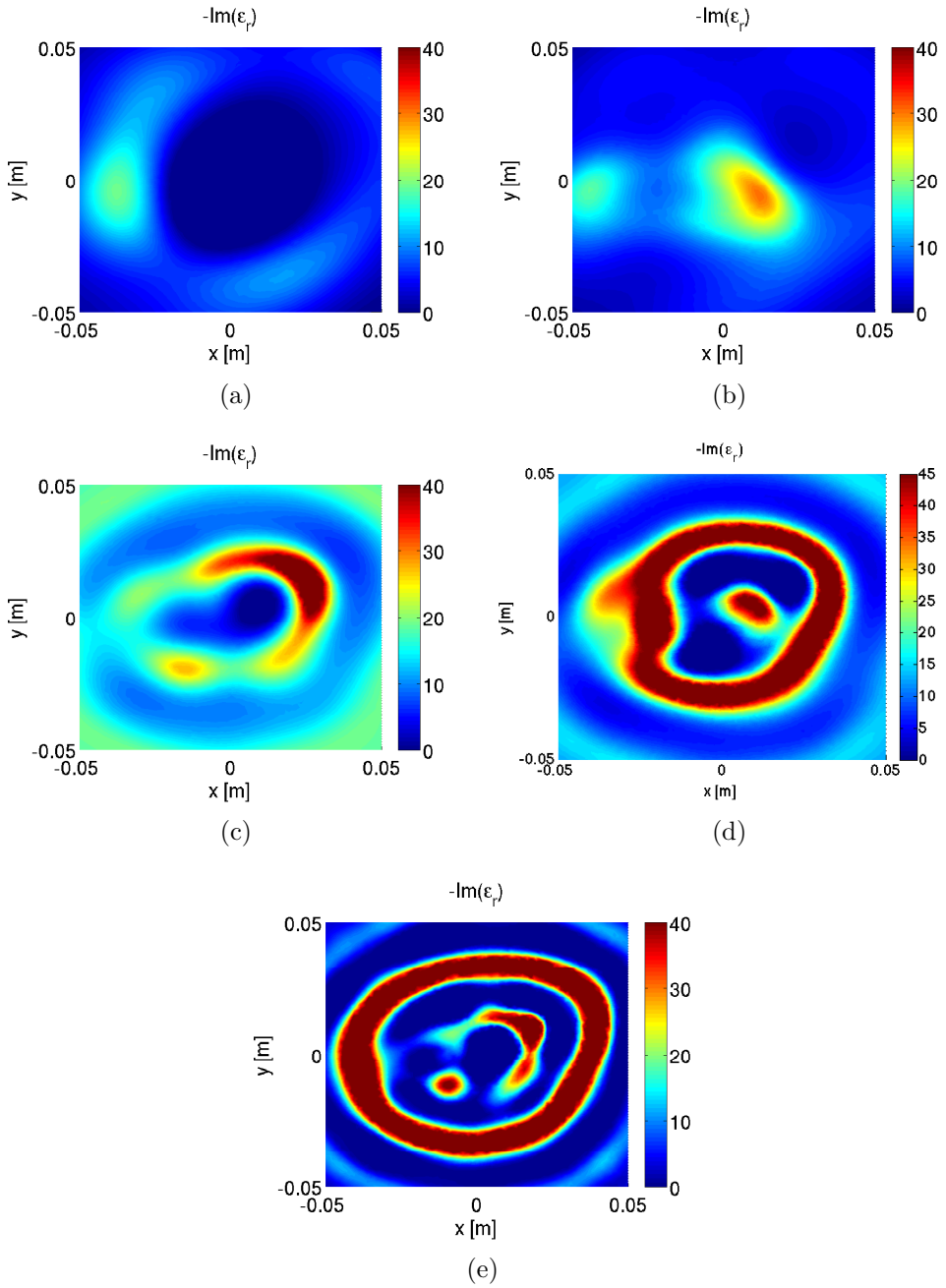

Figure 5.2: Imaginary part of blind reconstructions in (a) air, (b) oil, (c) glycerin solution 1, (d) glycerin solution 2, and (e) water immersion media.

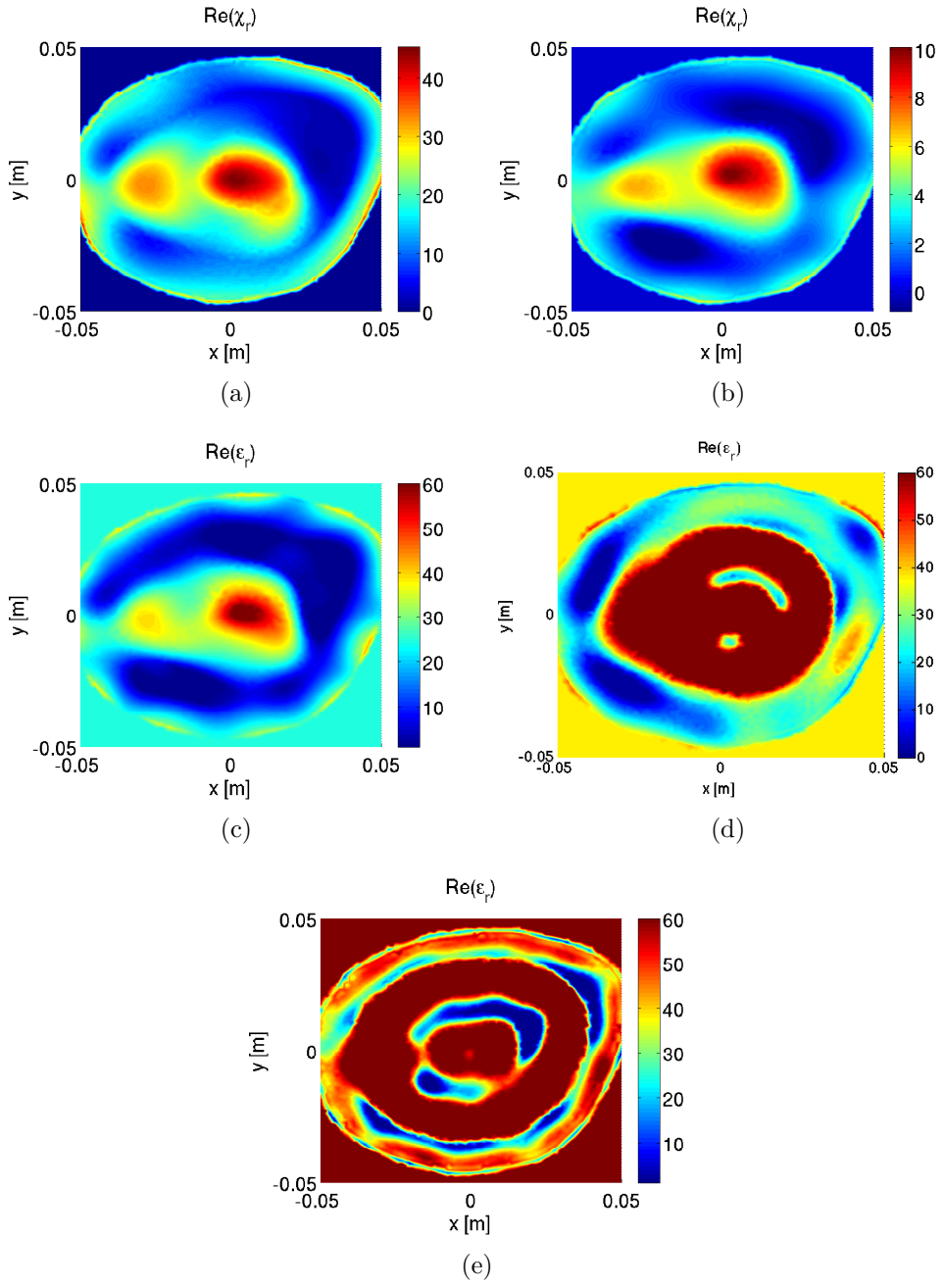

Figure 5.3: Real part of blind reconstructions with restricted imaging domain in (a) air, (b) oil, (c) glycerin solution 1, (d) glycerin solution 2, and (e) water immersion media.

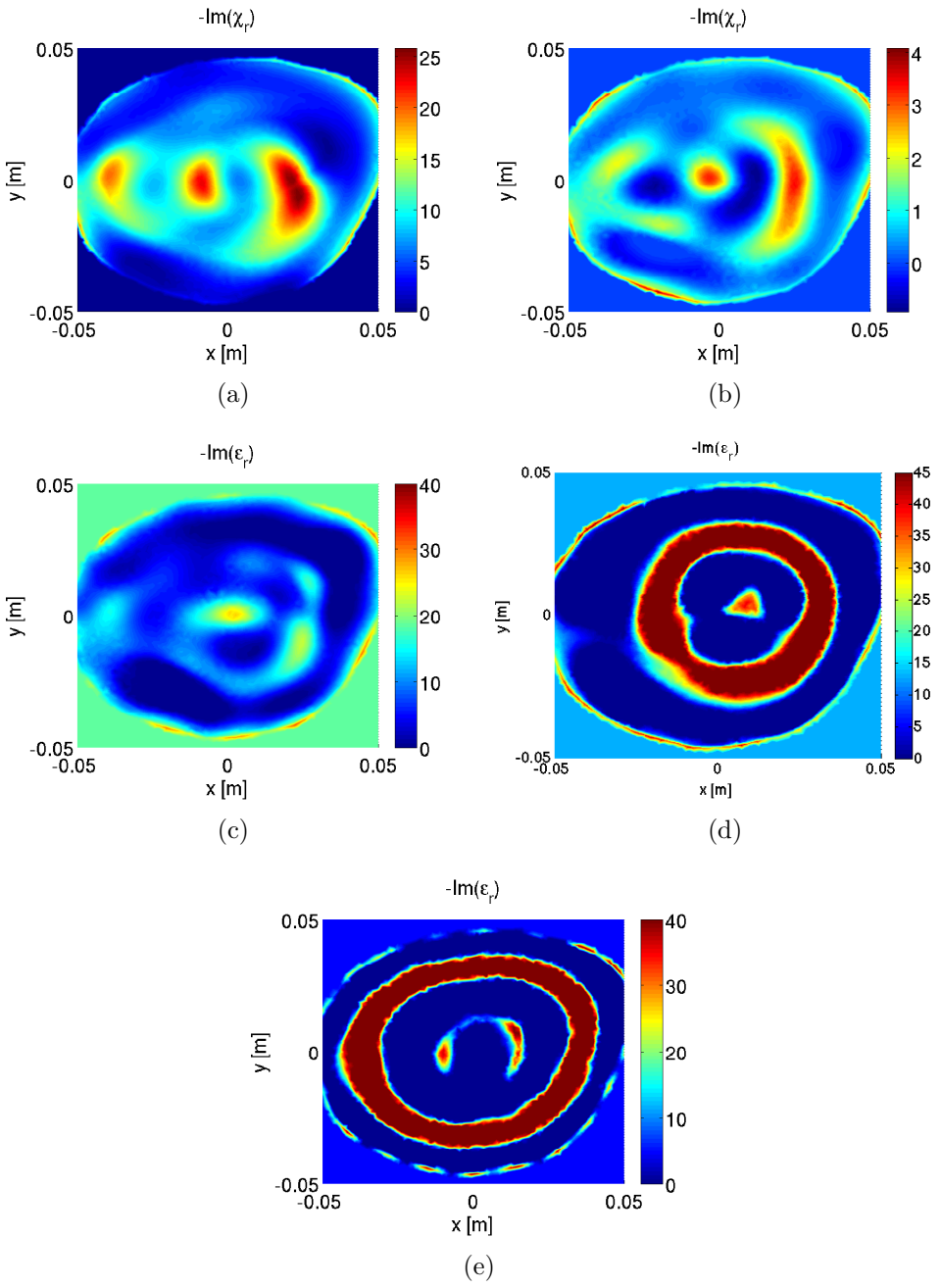

Figure 5.4: Imaginary part of blind reconstructions with restricted imaging domain in (a) air, (b) oil, (c) glycerin solution 1, (d) glycerin solution 2, and (e) water immersion media.

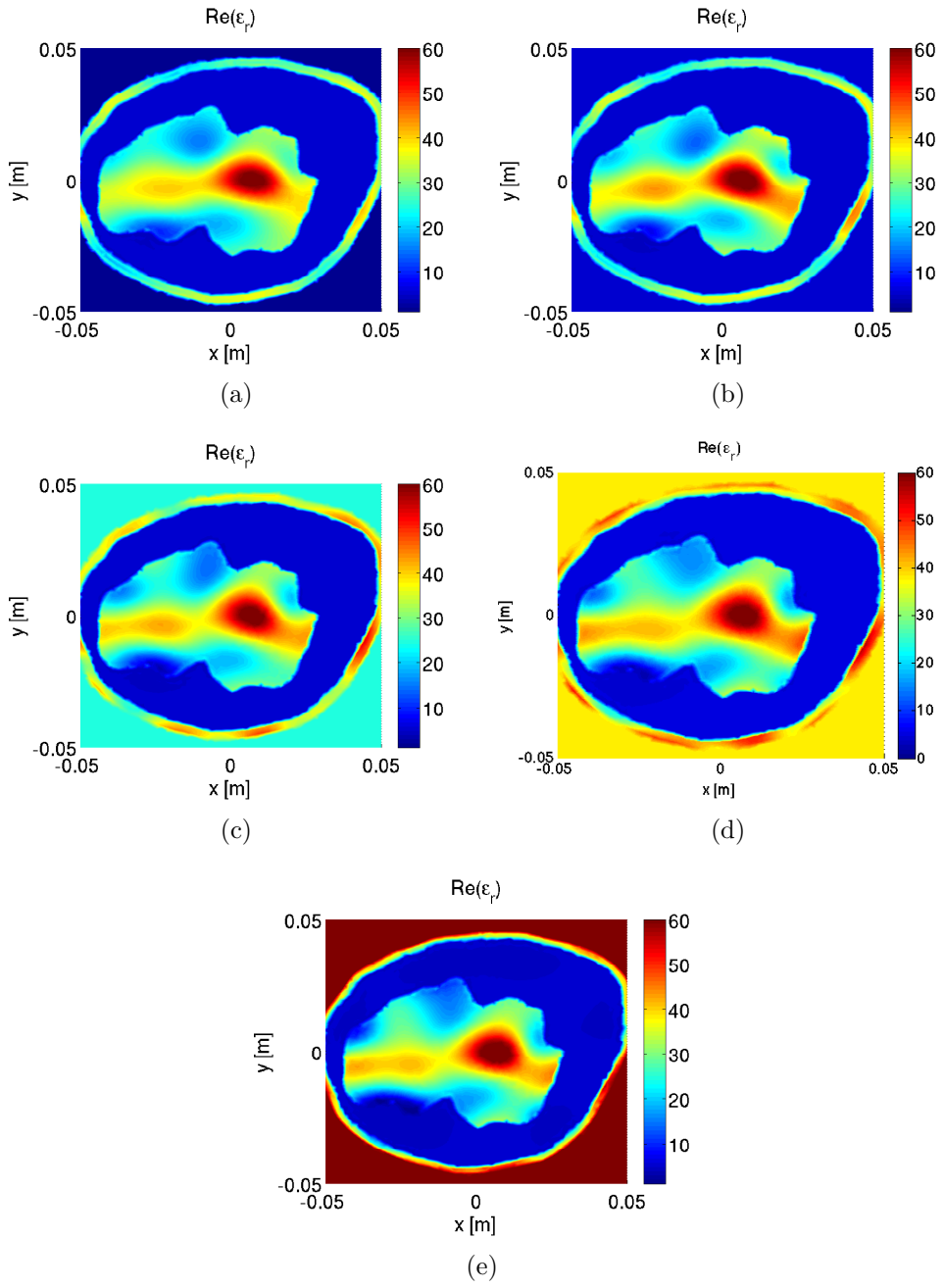

Figure 5.5: Real part of radar-region prior reconstructions with restricted imaging domain in (a) air, (b) oil, (c) glycerin solution 1, (d) glycerin solution 2, and (e) water immersion media.

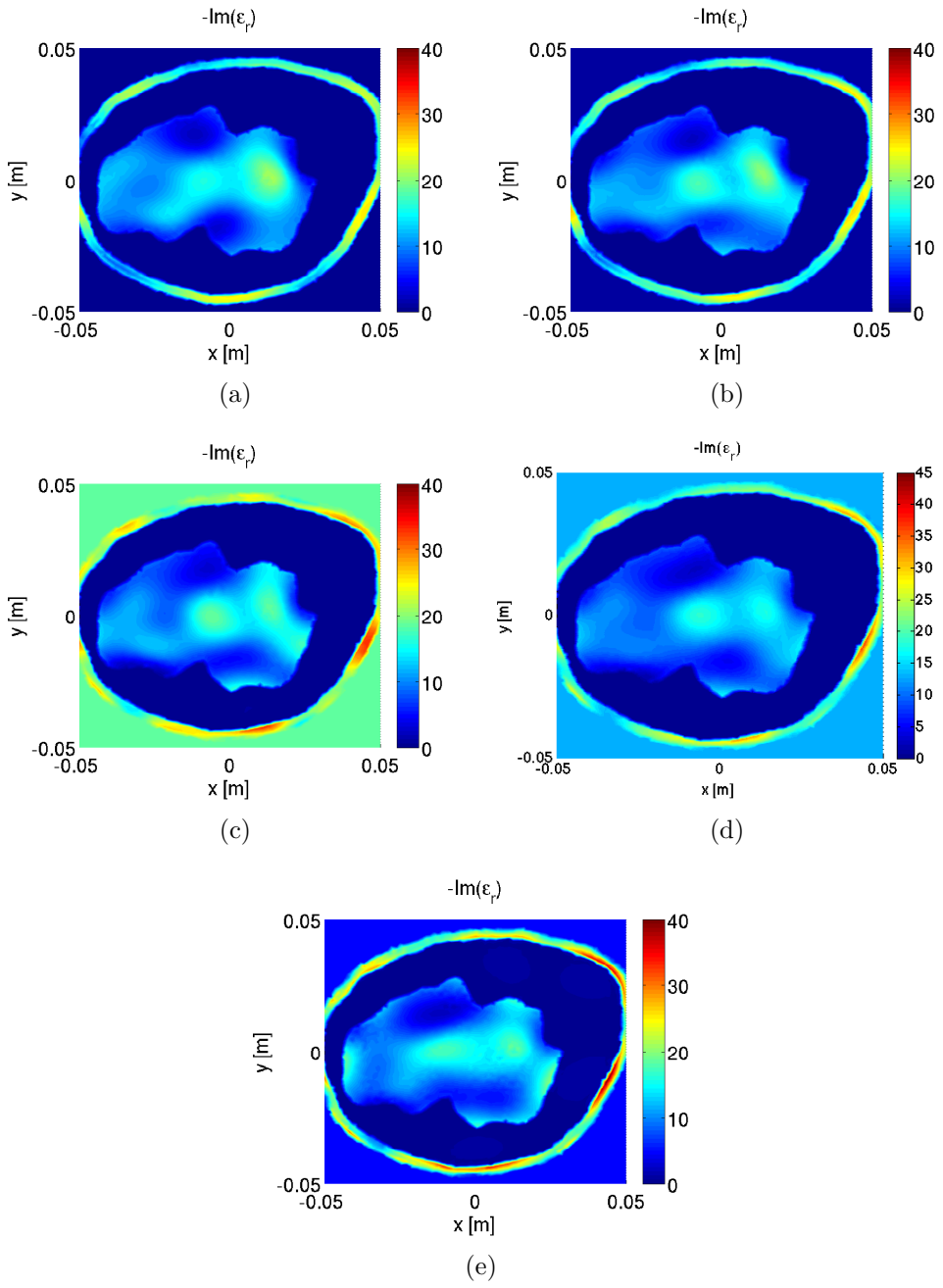

Figure 5.6: Imaginary part of radar-region prior reconstructions with restricted imaging domain in (a) air, (b) oil, (c) glycerin solution 1, (d) glycerin solution 2, and (e) water immersion media.

immersion medium in which the breast is submerged. As mentioned in the previous section, this background medium has a significant effect on many imaging parameters. However, ϵ_b has no effect on the inversion algorithm itself. FEM-CSI is able to invert using the immersion medium alone, where the contrast equation is given in Eq. 1.1. In the EIL's formulation of CSI, a a spatially varying numerical background $\epsilon_n(r)$ can be introduced into the contrast, as shown in Eq. 1.2. This numerical background can be uniform or inhomogeneous, and can be assigned any complex permittivity value, chosen by the user to optimize the reconstruction.

To demonstrate the independence of the inversion to ϵ_b, consider the Helmholtz equations governing the microwave imaging problem. Specifically we consider the TM case, where the electrical properties and fields are not varying in $\hat{z}$. The electric field in this formulation is z polarized and there are no transverse components in $x-y$. It is also assumed that the material is non-magnetic, that is $\mu_r = 1$.

For clarity, the equations for the contrast given in Eq. 1.1 and Eq. 1.2 can be rewritten such that,

$$\chi_b(\vec{r}) = \frac{\epsilon_r(\vec{r}) - \epsilon_b}{\epsilon_b} \tag{5.1}$$

is the contrast with respect to the physical background ϵ_b, and,

$$\chi_n(\vec{r}) = \frac{\epsilon_r(\vec{r}) - \epsilon_n(\vec{r})}{\epsilon_n(\vec{r})} \tag{5.2}$$

is the contrast with respect to a numerical background ϵ_n. The Helmholtz equations can now be written as:

$$\nabla^2 E^{sct}_{t,z}(\boldsymbol{r}) + k_b^2(\chi_b(\boldsymbol{r}) + 1)E^{sct}_{t,z}(\boldsymbol{r}) = -k_b^2\chi_b(\boldsymbol{r})E^{inc}_{t,z}(\boldsymbol{r}) \tag{5.3}$$

or

$$\nabla^2 E^{sct}_{t,z}(\boldsymbol{r}) + k_b^2(\boldsymbol{r}) E^{sct}_{t,z}(\boldsymbol{r}) = -k_b^2 E^{sct}_{t,z}(\boldsymbol{r}) w_{t,z}(\boldsymbol{r}). \tag{5.4}$$

Here t is the transmitter index, $k_b(\boldsymbol{r})$ is the background wavenumber, and $w_{t,z}(\boldsymbol{r})$ are the contrast sources such that $w_{t,z}(\boldsymbol{r}) = \chi_b(\boldsymbol{r}) E_{t,z}(\boldsymbol{r})$ where χ_b is the contrast with respect to the immersion medium, and E_{sct} and E_{inc} are the scattered and total fields respectively. The subscript b indicates that the corresponding variable is taken with respect to the immersion medium. Therefore, FEM-CSI would use these equations when solving for the contrast as given with respect to the physical background.

These equations can also be written with respect to a numerical background:

$$\nabla^2 E^{sct}_{t,z}(\boldsymbol{r}) + k_n^2(\chi_n(\boldsymbol{r}) + 1) E^{sct}_{t,z}(\boldsymbol{r}) = -k_n^2 \chi_n(\boldsymbol{r}) E^{inc}_{t,z}(\boldsymbol{r}) \tag{5.5}$$

or

$$\nabla^2 E^{sct}_{t,z}(\boldsymbol{r}) + k_n^2(\boldsymbol{r}) E^{sct}_{t,z}(\boldsymbol{r}) = -k_n^2 E^{sct}_{t,z}(\boldsymbol{r}) w_{t,z}(\boldsymbol{r}). \tag{5.6}$$

Here $k_n(\boldsymbol{r})$ is the numerical background wavenumber, and $w_{t,z}(\boldsymbol{r})$ are the contrast sources such that $w_{t,z}(\boldsymbol{r}) = \chi_n(\boldsymbol{r}) E_t(\boldsymbol{r})$ where χ_n is the contrast with respect to the numerical background. The subscript n indicates that the corresponding variable is taken with respect to the numerical background.

Equations 5.5 and 5.6 do not depend on the physical background ϵ_b, and consequently the FEM-CSI algorithm is completely independent of the complex permittivity of the immersion medium. This allows for the reconstruction of the breast interior in various immersion media, so long as adequate prior information is introduced to regularize unstable solutions and make use of limited interrogation data due

to excessive scattering from the surface of the OI.

The immersion medium continues to affect the overall imaging system performance, even with the use of a numerical background, because the obtainable interrogation energy arriving at the receivers from the inside of the breast depends on the electromagnetic match between the immersion medium and the breast's surface. However, the independence of the reconstruction algorithm with respect to the immersion medium provides us with the flexibility to choose system parameters that are influenced by other considerations, such as the wavelength in the surrounding medium, which affects the size and number of sensors that can occupy the imaging system.

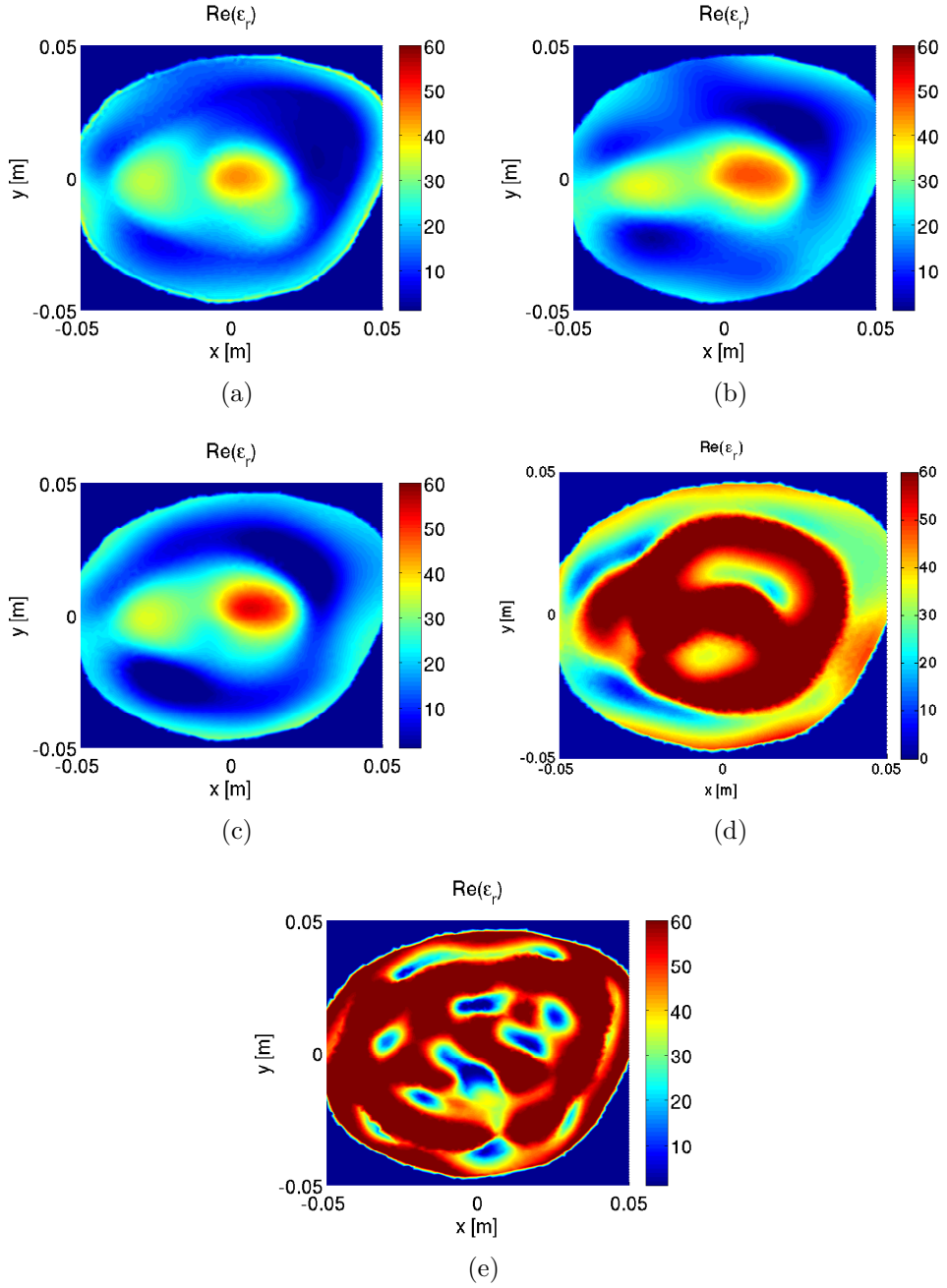

Figure 5.7: Real part of reconstruction with data collected in air immersion medium, inverted in (a) air numerical background, (b) oil numerical background, (c) glycerin solution 1 numerical background, (d) glycerin solution 2 numerical background, (e) water numerical background.

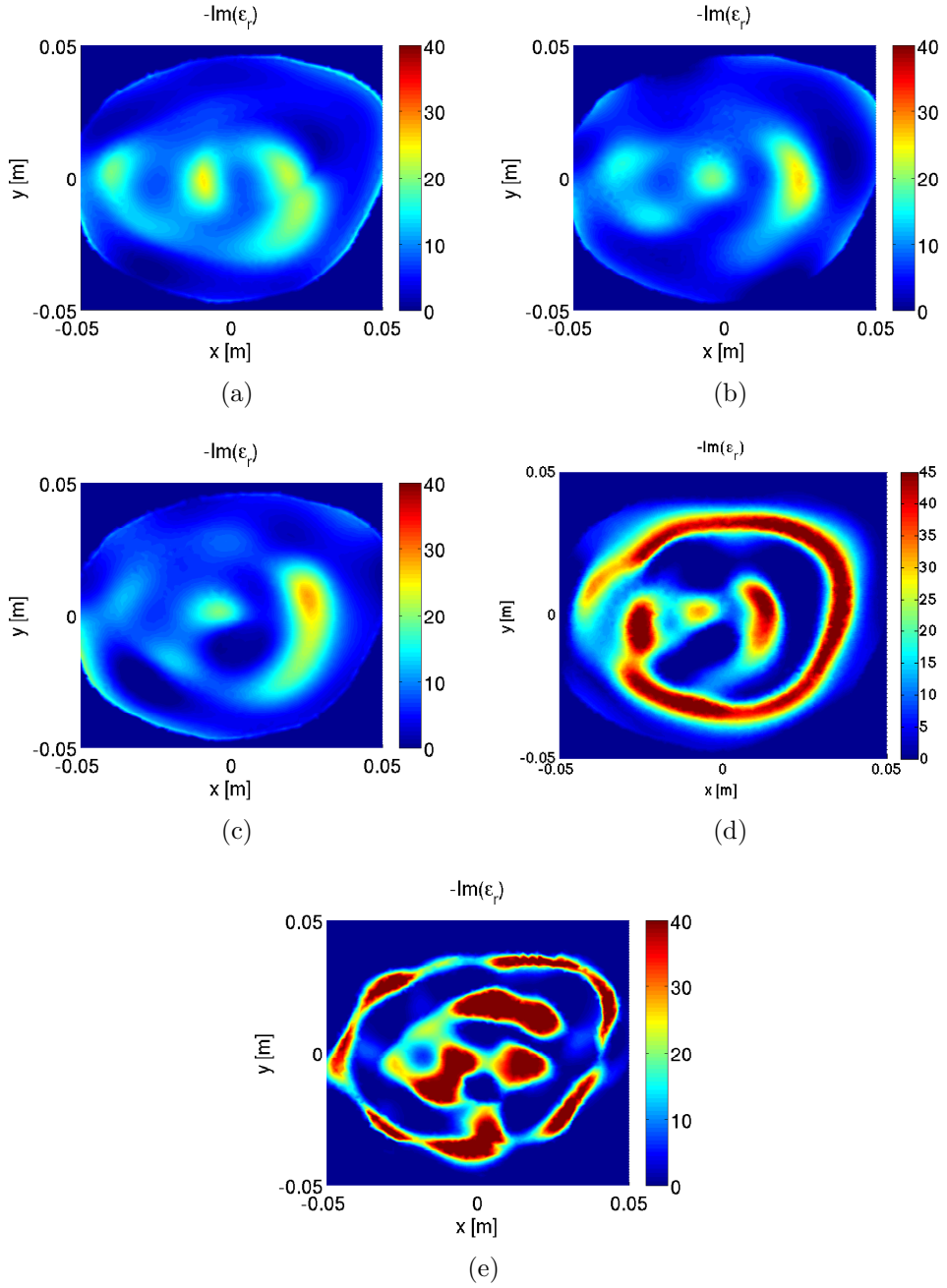

Figure 5.8: Imaginary part of reconstruction with data collected in air immersion medium, inverted in (a) air numerical background, (b) oil numerical background, (c) glycerin solution 1 numerical background, (d) glycerin solution 2 numerical background, (e) water numerical background.

5.4 General Numerical Backgrounds for Regularization

It is of interest to find a numerical background that sufficiently regularizes the inverse problem for MWI situations in which detailed interior prior information is not available. The ideal numerical background might not be the same for every clinical patient or every experimental or synthetic breast phantom, since the interior properties may vary, and therefore the complex permittivity required to reduce the contrast may also vary. We perform simulations in which the five immersion medium presented in Section 6.1, are used to collect data, but are inverted using a numerical background with different properties. For simplicity, the same permittivities were used in different combinations of physical and numerical backgrounds. Data are collected and inverted using the same circular imaging chamber and antenna configurations as in all of the previous chapters. The inversions are performed without the addition of noise. However, the inverse and forward meshes are different to reduce possible inverse crime effects.

Figures 5.7 to 5.16 show the real and imaginary parts of the FEM-CSI reconstruction, inverted in numerical backgrounds of air, oil, glycerin solution 1, glycerin solution 2 and water. The corresponding L_2 error norms are shown in Table 5.2. The discussion below focuses on the real part of the results, since the imaginary part does not reconstruct any diagnostically useful information due to poor balancing. The numerical background and imaging domain are both assigned to the region within the outer skin layer of the breast.

An air immersion medium is considered first, with results shown in Figure 5.7 and Figure 5.8. We observe similar results between numerical backgrounds of air

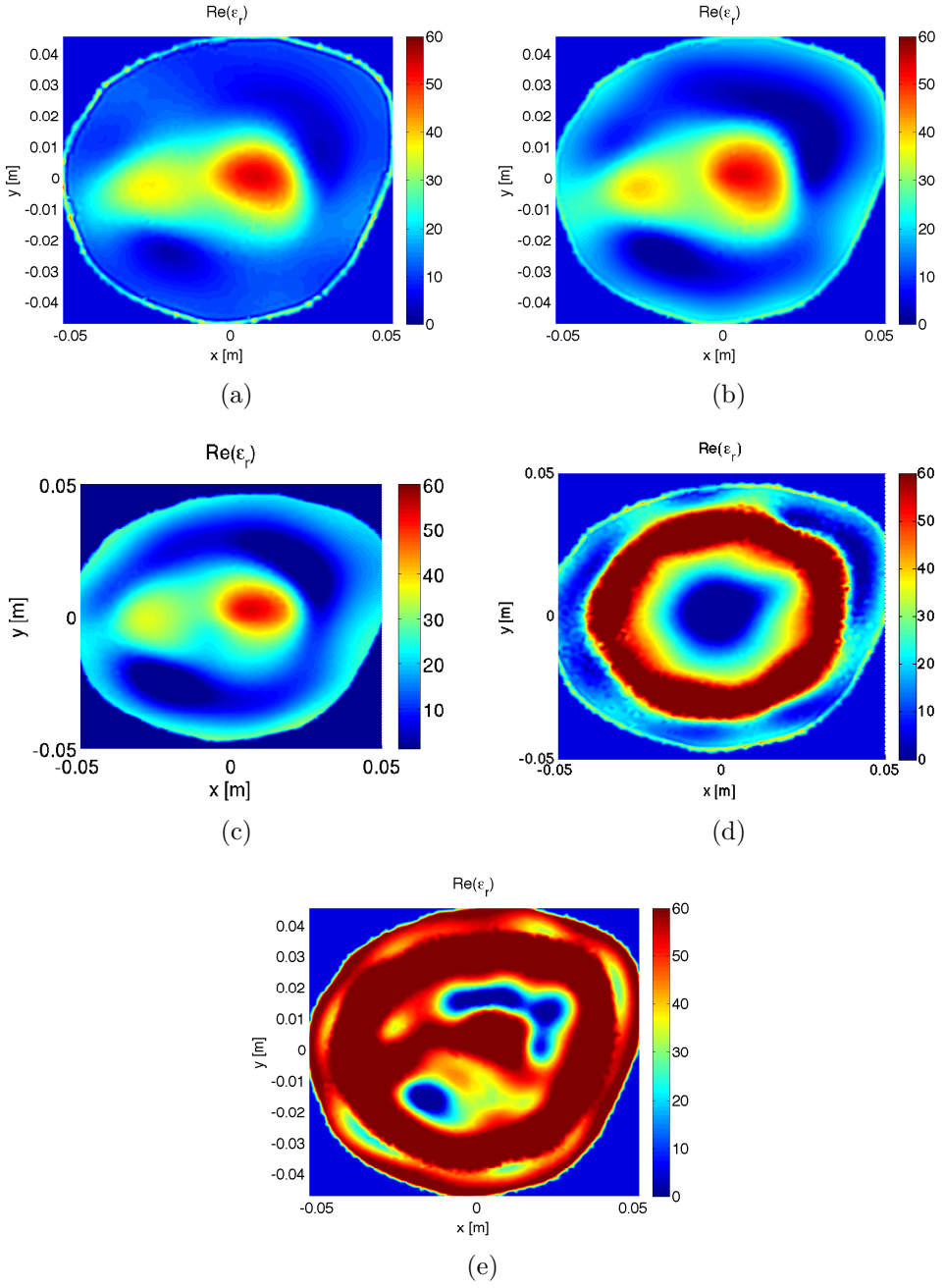

Figure 5.9: Real part of reconstruction with data collected in oil immersion medium, inverted in (a) air numerical background, (b) oil numerical background, (c) glycerin solution 1 numerical background, (d) glycerin solution 2 numerical background, (e) water numerical background.

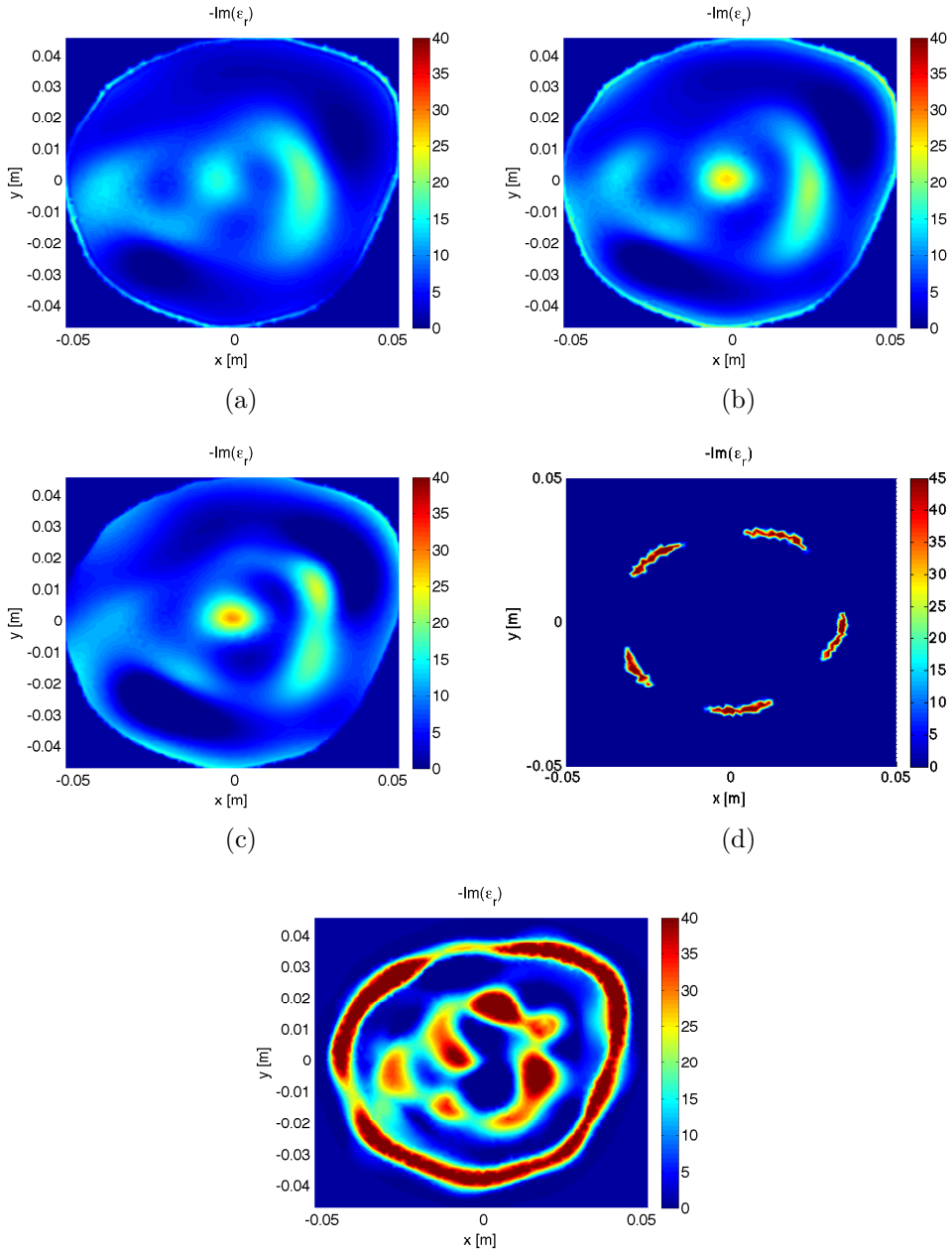

Figure 5.10: Imaginary part of reconstruction with data collected in oil immersion medium, inverted in (a) air numerical background, (b) oil numerical background, (c) glycerin solution 1 numerical background, (d) glycerin solution 2 numerical background, (e) water numerical background.

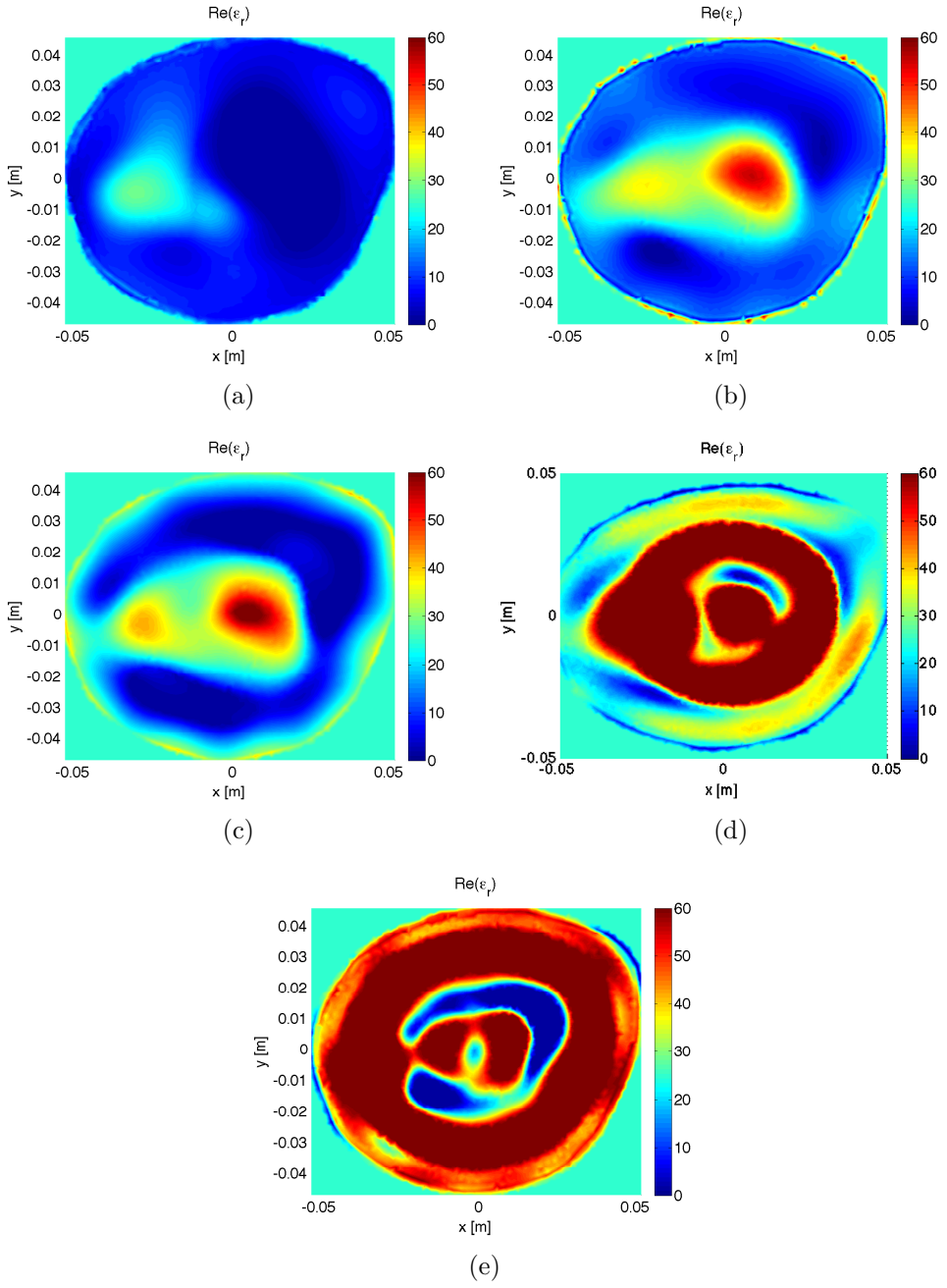

Figure 5.11: Real part of reconstruction with data collected in glycerin solution 1 immersion medium, inverted in (a) air numerical background, (b) oil numerical background, (c) glycerin solution 1 numerical background, (d) glycerin solution 2 numerical background, (e) water numerical background.

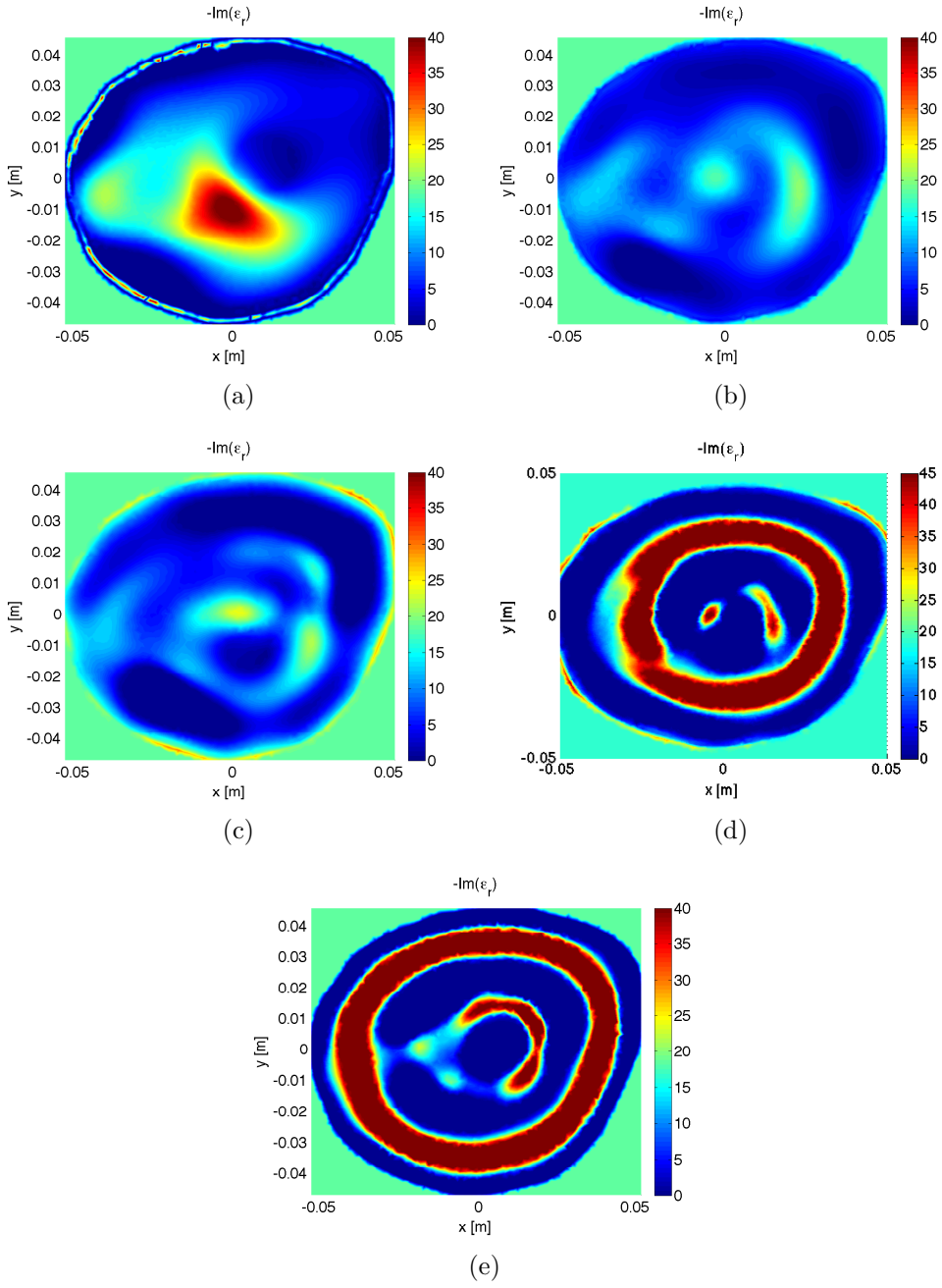

Figure 5.12: Imaginary part of reconstruction with data collected in glycerin solution 1 immersion medium, inverted in (a) air numerical background, (b) oil numerical background, (c) glycerin solution 1 numerical background, (d) glycerin solution 2 numerical background, (e) water numerical background.

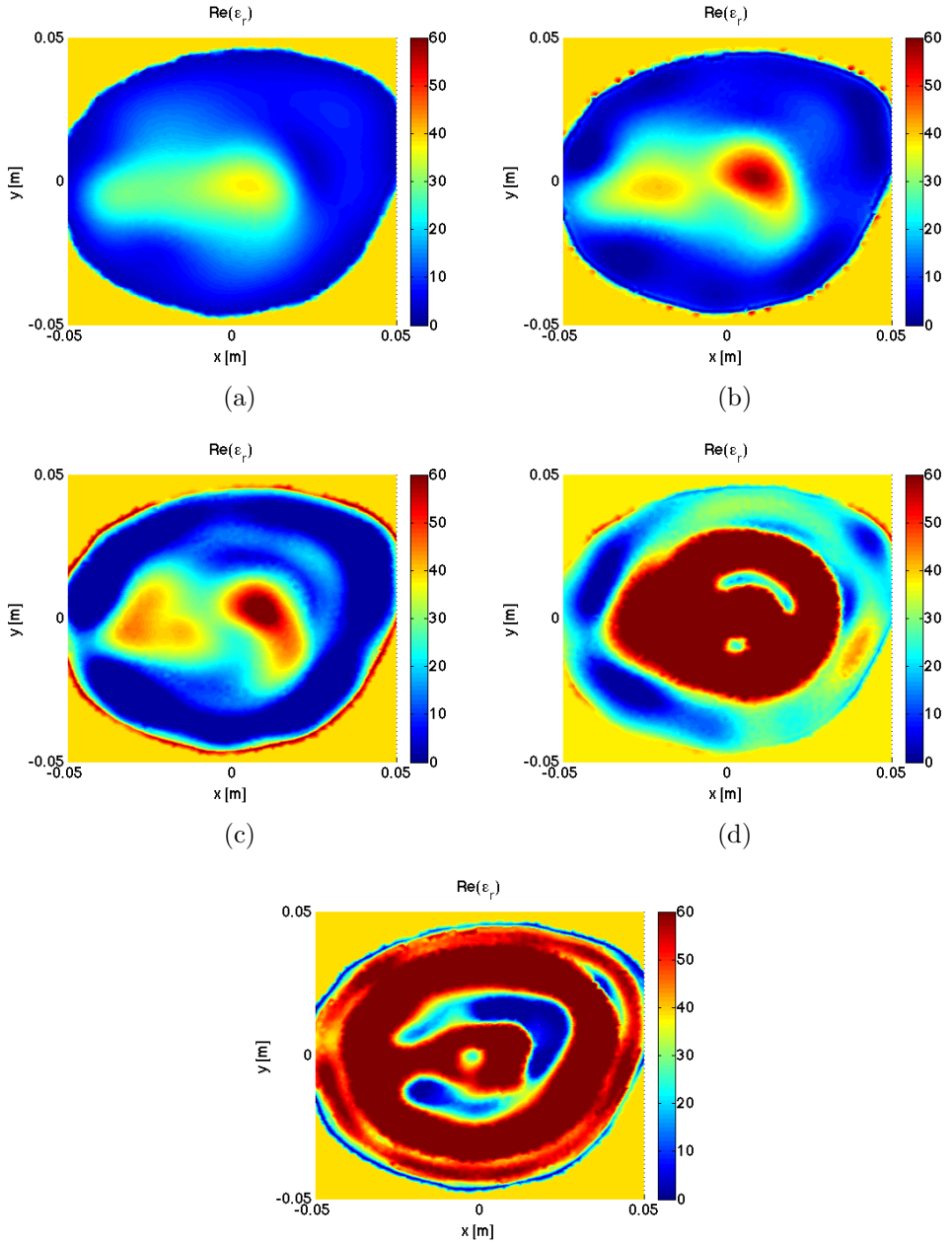

Figure 5.13: Real part of reconstruction with data collected in glycerin solution 2 immersion medium, inverted in (a) air numerical background, (b) oil numerical background, (c) glycerin solution 1 numerical background, (d) glycerin solution 2 numerical background, (e) water numerical background.

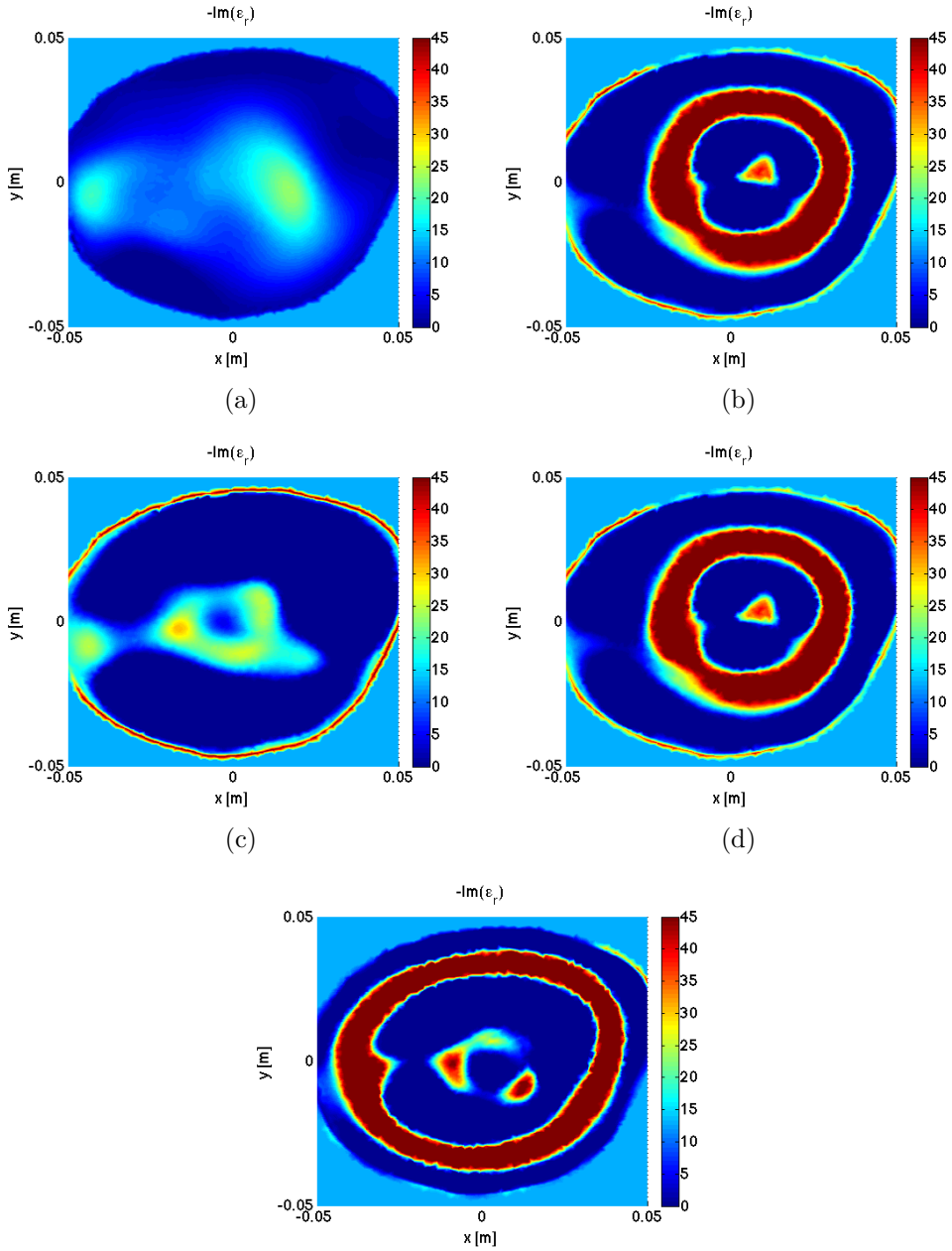

Figure 5.14: Imaginary part of reconstruction with data collected in glycerin solution 2 immersion medium, inverted in (a) air numerical background, (b) oil numerical background, (c) glycerin solution 1 numerical background, (d) glycerin solution 2 numerical background, (e) water numerical background.

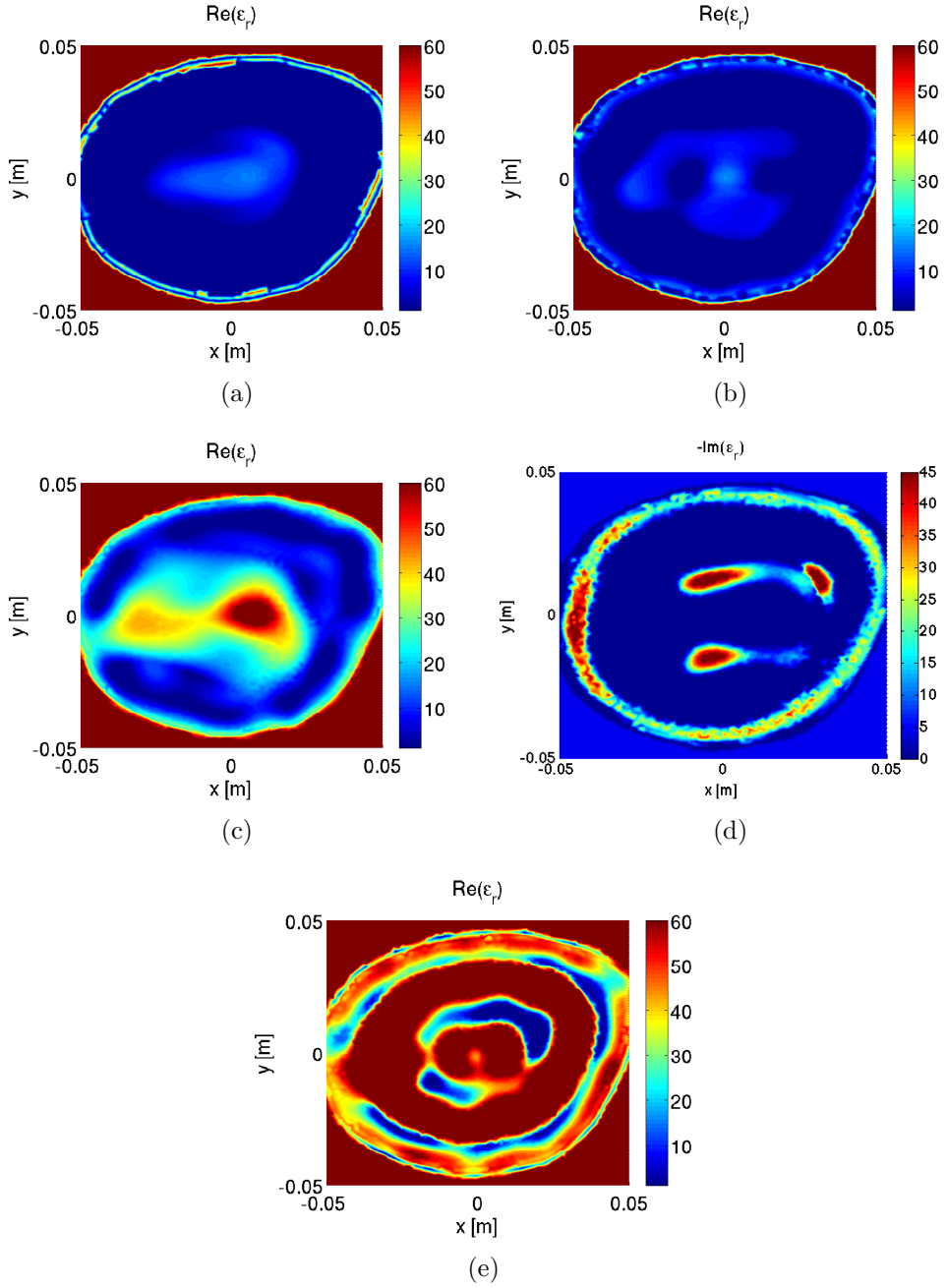

Figure 5.15: Real part of reconstruction with data collected in water immersion medium, inverted in (a) air numerical background, (b) oil numerical background, (c) glycerin solution 1 numerical background, (d) glycerin solution 2 numerical background, (e) water numerical background.

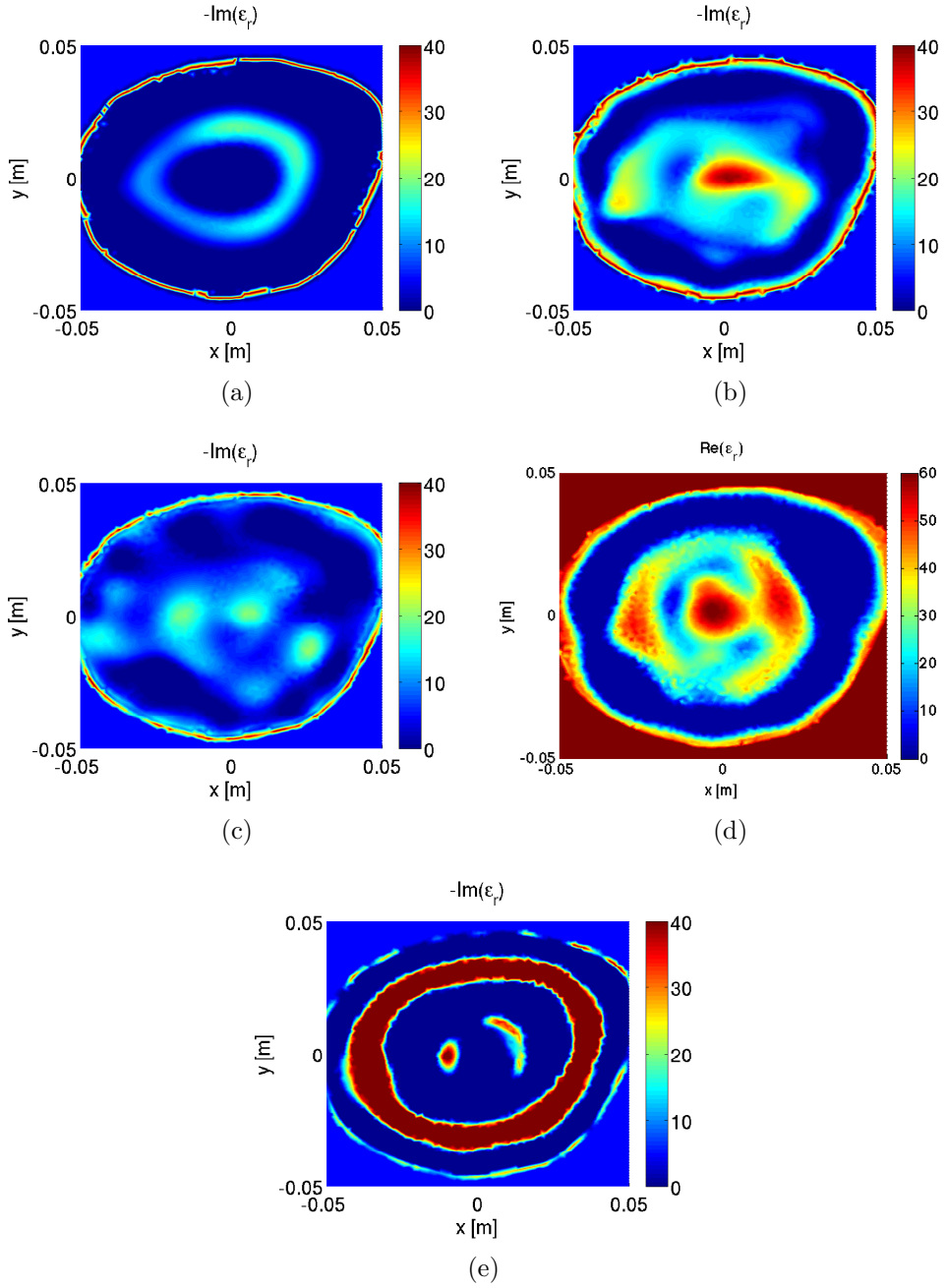

Figure 5.16: Imaginary part of reconstruction with data collected in water immersion medium, inverted in (a) air numerical background, (b) oil numerical background, (c) glycerin solution 1 numerical background, (d) glycerin solution 2 numerical background, (e) water numerical background.

and oil. This similarity is also reflected in the L_2 error norms, which is likely due to the similarity of the permittivity values of these two media. The reconstruction in the glycerin solution 1 numerical background is similar. However it better delineates the fat, fibrogandular and tumour regions, and reconstructs the tumour permittivity closer to the actual value. The glycerin solution 2 and the water numerical background produce an unusable result, although this is not reflected in the L_2 norms. Results in the oil and glycerin solution 1 immersion media, shown in Figure 5.9, 5.10, 5.11 and 5.11, produce very similar results to that of air, with the same trend for the air, oil, and glycerin solution 1 numerical background. The glycerin solution 2 and water inversions are also not diagnostically useful.

The principal result of this study presents itself when inversions are performed in physical immersion media of glycerin solution 2 and water. No reliable images are produced when inverting with numerical backgrounds of air, oil, glycerin solution 2 or water when using these immersion media. However, inverting using the glycerin solution 1 as a numerical background generates the most accurate reconstruction in terms of tissue region delineation and permittivity reconstruction within that region. In fact, in the case of the water immersion medium, the L_2 norms show that the inversion in the glycerin solution 2 numerical background only differs from the radar region prior case by 2.15%. This is likely due short wavelength of the incident field

ϵ_n, ϵ_b	Air	Oil	Glycerin Sol 1	Glycerin Sol 2	Water
Air	57.53%	60.53%	64.60%	57.11%	48.42%
Oil	58.45%	57.69%	58.91%	50.69%	33.15%
Glycerin Sol 1	59.28%	58.70%	55.24%	47.14%	25.86%
Glycerin Sol 2	164.08%	172.70%	169.86%	132.02%	33.00%
Water	206.16%	214.66%	209.56%	166.40%	106.00%

Table 5.2: L_2 Error norms for various combinations of immersion medium and uniform numerical background.

provided by the water immersion medium, combined with the closeness of glycerin to the average properties of the breast, which lowers the contrast within the breast significantly.

These results show that in most immersion media, reconstructions are possible as long as an optimal numerical background is used. This implies that microwave imaging system parameters can be chosen based on patient comfort, and the wavelength of the incident radiation.

5.5 March-On-Frequency and March-On-Background Techniques

The inverse MWI problem is ill-posed and contains many more unknowns in the imaging domain than there are collected field data at the receiver locations. This means that diverse data is required for an accurate reconstruction of the OI, and increasing that diversity often further improves the reconstruction. There are techniques that take advantage of data diversity, such as frequency-hopping or march-on-frequency, where reconstruction results at different frequencies are used as an initial guess for the next, and simultaneous frequency inversions that assume little change in permittivity of the OI over short frequency steps [48].

March-on-frequency techniques can be uniquely applied in FEM-CSI reconstructions by utilizing the inhomogeneous background. Figure 5.17 shows an example of such a technique, where the radar regional map is used as prior information. In this scenario, a blind reconstruction is performed on data collected at 1GHz. Data is then collected at 1.25GHz and is inverted using the result at the previous frequency as prior information. This is then repeated at 1.5GHz, where the solution of the

previous reconstruction is used as an inhomogeneous background. As the frequency increases, we obtain a higher resolution of fine structures within the breast - even resolving a small tumour that was undetectable at lower frequencies.

The immersion medium independent nature of the FEM-CSI algorithm presents a unique opportunity to diversify data. We introduce a march-on-background technique, in which data are collected from the same OI in different immersion media. The wavelength and interrogation energy of the incident radiation are dictated by the various immersion media, and a unique data set is collected in each one.

When using march-on-background, data are collected in a particular immersion medium and inverted in any numerical background. Data are then collected from the same OI in a different immersion medium, but the previous result is used as a numerical background when reconstructing the new image. This procedure can be done as many times as required to improve the reconstruction, keeping in mind that not every addition necessarily produces a better result, and often different combinations of media must be tried before seeing an improvement. Fortunately, there are many immersion media with large ranges of complex permittivity, making successful combinations likely. Figure 5.18 shows one of these combinations. Figure 5.18 a shows a reconstruction of the phantom in an oil immersion medium, with corresponding L_2 norm shown in Table. 5.3. This is an average result with limited resolution, but it does provide an indication that a tumour is present, and gives its general location. Figure 5.18 b shows the inversion in glycerin solution 2. This poor reconstruction

Immersion Medium	L_2
Oil	57.69%
Glycerin Solution 2	132.02%
March-on	46.03%

Table 5.3: Improvements using march-on-background technique

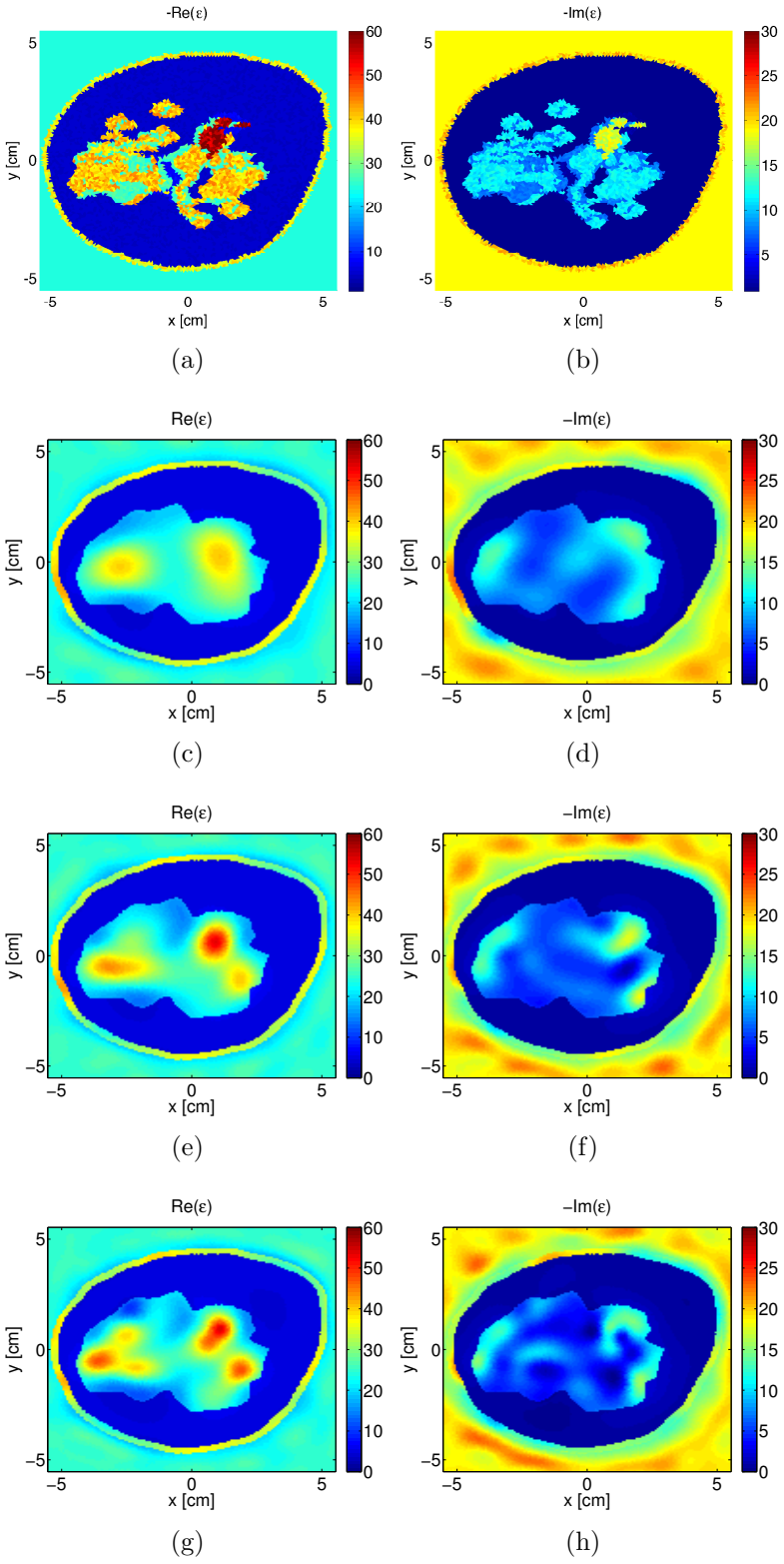

Figure 5.17: Model 2, March-on-frequency: (a), (b): numerical phantom, (c),(d): 1GHz, (e), (f) 1.25GHz, (g),(h): 1.5GHz

.

provides no diagnostic information and its L_2 norm reflects its poor quality.

Figure 5.18 c was obtained using the march-on-background technique. When inverting using the glycerin solution 2 immersion medium, the solution from the oil reconstruction is incorporated as a numerical background. This not only regularizes the solution, but it greatly improves the result over either of these immersion media used alone. Details in the shape of the tumour that were not previously detectable become apparent. This improvement is reflected in the L_2 norm.

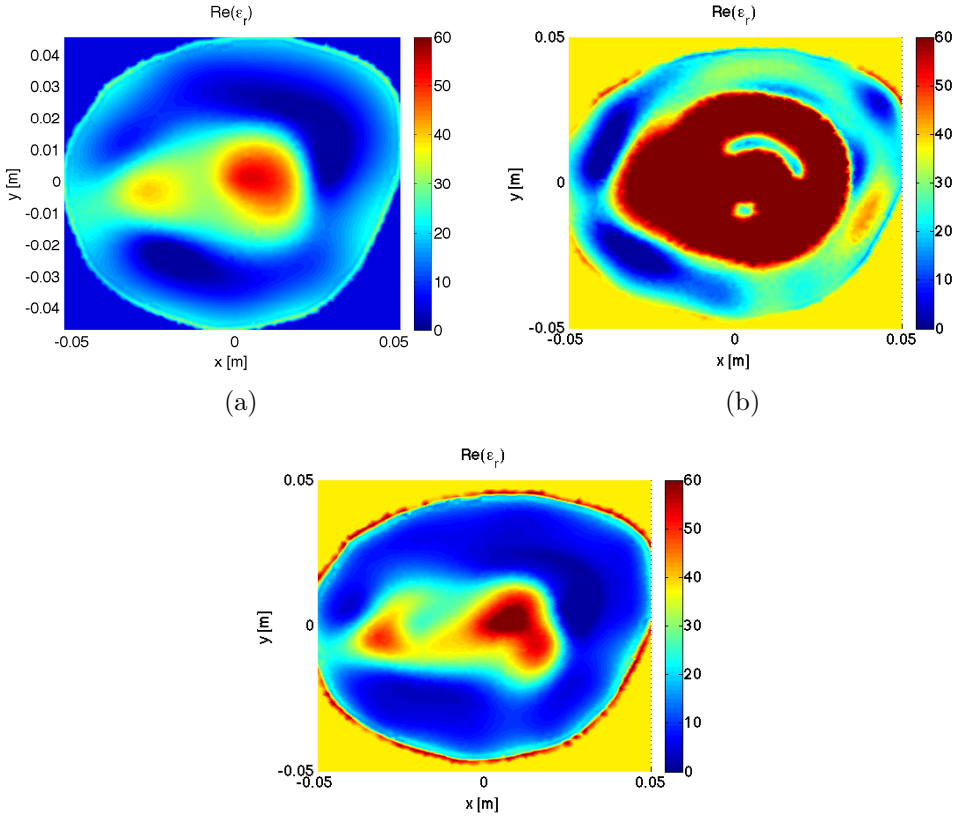

Figure 5.18: *March-on-background*: (a) blind inversion in oil, (b) blind inversion in glycerin solution 2 (c) reconstructing using march-on-background technique.

Chapter 6

Conclusions and Future Work

This thesis demonstrated the successful implementation and analysis of 2D and 3D microwave imaging techniques for breast cancer detection and monitoring. In summary:

- A simulated annealing algorithm was developed to locate prior information regions in experimental human forearm images, and motivated the need to obtain high quality prior information for biological OIs, particularly those that exhibit high contrasts.
- A combined radar-MWT algorithm was developed for breast imaging using numerical phantoms. The hybrid algorithm was tested extensively on realistic MRI derived numerical phantoms in 2D, and realistic, high-contrast, numerical breast models in 3D.
- The effect of prior information on inversion results was analyzed using synthetic data in 2D and 3D.
- The combined algorithm was applied to numerical phantoms with varying tu-

mour sizes in order to determine if these size differences could be detected. The successful detection of these differences show the algorithm to be a potential tool for tumour monitoring during cancer treatment.

- An immersion medium independent algorithm was introduced and demonstrated using 2D numerical breast phantoms.

- March-on-background and march-on-frequency techniques were used to show that diversity of data can increase reconstruction quality.

6.1 Future Work

The following items will be investigated as future work on this topic:

- Finite element inverse solvers with higher order basis functions will most likely be required for this work to continue. These solvers will increase the accuracy while reducing the number of elements in the mesh [49].

- Non-uniform MRI-based numerical phantoms have recently been supported by the 3D FEM-CSI code. Analysis of the presented techniques on more realistic datasets will be essential for proper analysis and characterization of our 3D reconstruction capabilities.

- Balancing of both real and imaginary variables, and the data and domain errors in both the 2D and 3D implementations of FEM-CSI could greatly improve the imaginary part of the reconstruction result. Complete confidence in the reconstruction results is not achieved without quality reconstructions in both parts of the complex permittivity.

- Experimental verification of the combined radar-MWT algorithm is currently underway. This process will be tested using several imaging systems with various boundary conditions at the EIL at the UofM. This study will utilize both 2D and 3D phantoms, imaging chambers and reconstruction algorithms. Simulations of the experimental setup and preliminary experimental results are promising.

- This work will be expanded into a multi-modality breast imaging study funded by a 3 year Canadian Breast Cancer Foundation grant. This grant, which is held by the University of Manitoba and the University of Calgary, will introduce ultrasound tomography and radar techniques into the imaging algorithm, and will develop an experimental system. The final year of this project will involve clinical trials.

Appendix A: List of Publications

Journal Publications

- D. Kurrant, A. Baran, J. LoVetri and E. Fear, Evaluating Impact of Errors in Prior Information on Microwave Tomography Image Quality, Medical Physics, 2016 (submitted)
- D. Kurrant, A. Baran, J. LoVetri and E. Fear, Impact of Detail in Prior Information on Microwave Tomography Image Quality, Medical Physics, 2016 (submitted)
- A. Baran, D. Kurrant, A. Zakaria, E. C. Fear, and J. LoVetri. "Breast Imaging Using Microwave Tomography with Radar-Based Tissue-Regions Estimation." Progress In Electromagnetics Research vol. 149, pp 161-171, 2014.
- A. Zakaria, A. Baran and J. LoVetri, Estimation and Use of Prior Information in FEM-CSI for Biomedical Microwave Tomography, IEEE Antenna Wireless and Propagation Letters, vol. 11, pp. 1606-1609, 2012.

Conference Publications

- D. Kurrant, A. Baran, E. C. Fear, and J. LoVetri. "Evaluating Impact of errors in Prior Information on Performance of Microwave Tomography", 17th International Symposium on Antenna Technology and Applied Electromagnetics, Montreal, QC, Canada, July 10-13, 2016.

- D. Kurrant, A. Baran, E. C. Fear, and J. LoVetri. "Iterative Refinement of Fibroglandular Region with Microwave Breast Imaging", Numerical Electromagnetic and Multiphysics Modeling and Optimization, Ottawa, ON, Canada, August 11-14, 2015.

- A. Baran, D. Kurrant, E. C. Fear, and J. LoVetri"Monitoring Breast Cancer Treatment Progress with Microwave Tomography and Radar-based Tissue-regions Estimation", 9th European Conference on Antennas and Propagation, Lisbon, Portugal, April 12-17, 2015.

- A. Baran, C. Kaye, A. Zakaria, J. LoVetri. "Investigation of Tumour Detection Using Contrast Agents and FEM-CSI in Biomedical Microwave Tomography", IEEE International Symposium on Antennas and Propagation and USNC/URSI National Radio Science Meeting, Orlando, FL, USA, July 7-13, 2013.

Appendix B: Mathematical Formulation

This appendix outlines the mathematical formulation for electromagnetic scattering and reconstructions using a numerical background medium. We begin with the differential form of Maxwell's equations,

$$\nabla \times \vec{\mathcal{E}}(\vec{r},t) = -\frac{\partial \vec{\mathcal{B}}(\vec{r},t)}{\partial t}, \tag{6.1}$$

$$\nabla \times \vec{\mathcal{H}}(\vec{r},t) = \frac{\partial \vec{\mathcal{D}}(\vec{r},t)}{\partial t} + \vec{\mathcal{J}}(\vec{r},t), \tag{6.2}$$

$$\nabla \cdot \vec{\mathcal{D}}(\vec{r},t) = \rho_v(\vec{r},t), \tag{6.3}$$

$$\nabla \cdot \vec{\mathcal{B}}(\vec{r},t) = 0, \tag{6.4}$$

where $\vec{\mathcal{E}}$ is the electric field intensity in [volts/metre], $\vec{\mathcal{D}}$ is the electric flux density in [coulombs/metre^2], $\vec{\mathcal{H}}$ is the magnetic field intensity in [amperes/metre], $\vec{\mathcal{B}}$ is the magnetic flux density in [webers/metre^2], $\vec{\mathcal{J}}$ is the electric current density in [amperes/metre^2] and ρ_v is the electric change density in [coulombs/metre^3]. These quantities are functions of position $\vec{r} = x, y, z$ and time t. Note that,

$$\vec{\mathcal{J}} = \vec{\mathcal{J}}_c + \vec{\mathcal{J}}_i \tag{6.5}$$

where $\vec{\mathcal{J}}_c$ describes medium's ability to conduct current and $\vec{\mathcal{J}}_i$ is due to impressed current sources.

The equations needed to describe the constituent relationships between the field

quantities and the medium in which the fields exist are,

$$\vec{\mathcal{D}} = \epsilon_0 \epsilon_r^{'}(\vec{r})\vec{\mathcal{E}}(\vec{r},t) \tag{6.6}$$

$$\vec{\mathcal{B}} = \mu_0 \mu_r(\vec{r})\vec{\mathcal{H}}(\vec{r},t) \tag{6.7}$$

$$\vec{\mathcal{J}}_c = \sigma(\vec{r})\vec{\mathcal{E}}(\vec{r},t). \tag{6.8}$$

Here ϵ_0 is the permittivity of free space in [farads/metre], $\epsilon_r^{'}$ is the real relative permittivity (unitless), μ_0 is the permeability of free space in [henrys/metre], μ_r is the relative permeability (unitless) and σ is the conductivity in [siemens/metre]. The medium considered is linear. Therefore, $\epsilon_r^{'}$, μ_r and σ are scalar quantities that do not depend on field strength.

The work presented in this thesis uses the time-harmonic form of Maxwell's equations with dependance $e^{j\omega t}$, where $j^2 = -1$ and the angular frequency $\omega = 2\pi f$ in [radians/second]. That is, the fields can be represented using complex quantities. For example, $\vec{E}$ is related to instantaneous $\vec{\mathcal{E}}$ by

$$\vec{\mathcal{E}} = \sqrt{2} Re(\vec{E} e^{j\omega t}). \tag{6.9}$$

The time-harmonic form of Maxwell's equations are then,

$$\nabla \times \vec{E}(\vec{r}) = -j\omega \vec{B}(\vec{r}), \tag{6.10}$$

$$\nabla \times \vec{H}(\vec{r}) = j\omega \vec{D}(\vec{r}) + \vec{J}(\vec{r}), \tag{6.11}$$

$$\nabla \cdot \vec{D}(\vec{r}) = \rho_v(\vec{r}), \tag{6.12}$$

$$\nabla \cdot \vec{B}(\vec{r}) = 0. \tag{6.13}$$

The relationships between the fields in time-harmonic form are written using complex quantities as,

$$\vec{D} = \hat{\epsilon}(\omega)\vec{E} \tag{6.14}$$

$$\vec{B} = \hat{\mu}(\omega)\vec{H} \tag{6.15}$$

$$\vec{J_c} = \sigma(\omega)\vec{E}. \tag{6.16}$$

Here $\hat{\mu}$ is the complex permeability of the medium, σ is the conductivity of the medium and $\hat{\epsilon}$ is the complex permittivity of the medium such that,

$$\hat{\epsilon}(\omega) = \epsilon^{'} - j\epsilon^{''} \qquad \text{or,} \tag{6.17}$$

$$\hat{\epsilon}(\omega) = \epsilon_0(\epsilon_r^{'} - j\epsilon_r^{''}). \tag{6.18}$$

We assume that our problem is free of charge ($\rho = 0$) and magnetic materials ($\mu = 1$) and derive a partial differential equation that involves only the electric field vector $\vec{E}$. $\vec{H}$ is eliminated from Equations 6.10 and 6.11 using the constituent relationships and the result is the Helmholtz equation given by,

$$\nabla \times \nabla \times \vec{E}(\vec{r}) - \omega^2 \mu_0 \epsilon_0 \epsilon_r(\vec{r}) \vec{E}(\vec{r}) = -j\omega\mu_0 \vec{J}_i(\vec{r}). \tag{6.19}$$

This equation is also known as the inhomogeneous vector wave equation. We define the complex relative permittivity as the bracketed term in Equation 6.18, that is,

$$\epsilon_r(\vec{r}) = \epsilon_r^{'}(\vec{r}) - j\epsilon_r^{''}(\vec{r}). \tag{6.20}$$

We assume that this term takes into account dielectric and conductive losses, including losses due to the dielectric strength of biological tissue as modelled by the Cole-Cole formula [50]. The corresponding electric contrast is defined as

$$\chi(\vec{r}) = \frac{\epsilon_r(\vec{r}) - \epsilon_n(\vec{r})}{\epsilon_n(\vec{r})} \tag{6.21}$$

where ϵ_n is the the complex numerical background permittivity.

Consider the imaging setup presented in Figure 1.3. The chamber is illuminated by a transmitter T and the field is measured at receiver points R. If there is no OI present, the field produced is referred to as the incident field $\vec{E}_t^{inc}$. This results in the vector wave equation,

$$\nabla \times \nabla \times \vec{E}_t^{inc}(\vec{r}) - \omega^2 \mu_0 \epsilon_0 \epsilon_r(\vec{r}) \vec{E}_t^{inc}(\vec{r}) = -j\omega\mu_0 \vec{J}_i(\vec{r}). \tag{6.22}$$

When the OI is present the equation becomes

$$\nabla \times \nabla \times \vec{E}_t^{tot}(\vec{r}) - \omega^2 \mu_0 \epsilon_0 \epsilon_r(\vec{r}) \vec{E}_t^{tot}(\vec{r}) = -j\omega\mu_0 \vec{J}_i(\vec{r}). \tag{6.23}$$

If the scattered field due to the OI is $\vec{E}_t^{sct} = \vec{E}_t^{tot} - \vec{E}_t^{inc}$, the vector wave equation governing the scattered field is

$$\nabla \times \nabla \times \vec{E}_t^{sct}(\vec{r}) - \omega^2 \mu_0 \epsilon_0 \epsilon_r(\vec{r}) \vec{E}_t^{sct}(\vec{r}) = -j\omega\mu_0 \vec{J}_i(\vec{r}). \tag{6.24}$$

This equation can be written in terms of the contrast $\chi(\vec{r})$ as

$$\nabla \times \nabla \times \vec{E}_t^{sct}(\vec{r}) - k_n^2(\vec{r})(\chi(\vec{r}) + 1)\vec{E}_t^{sct}(\vec{r}) = k_n^2(\vec{r})\chi(\vec{r})\vec{E}_t^{inc}(\vec{r}), \tag{6.25}$$

where k_n is the numerical background wavenumber. This can be rearranged to give

$$\nabla \times \nabla \times \vec{E}_t^{sct}(\vec{r}) - k_n^2(\vec{r})\vec{E}_t^{sct}(\vec{r}) = k_n^2(\vec{r})\vec{w}_t(\vec{r}) \tag{6.26}$$

where $\vec{w}_t(\vec{r})$ are the contrast sources defined as

$$\vec{w}_t(\vec{r}) = \chi(\vec{r})\vec{E}_t^{tot}(\vec{r}). \tag{6.27}$$

The contrast sources are scattering sources located inside the OI that produce $\vec{E}_t^{sct}$ in the background medium. We can rewrite the vector wave equation in operator notation as

$$\vec{\mathcal{H}}_n\{\vec{E}_t^{sct}\} = k_n^2(\vec{r})\vec{w}_t(\vec{r}). \tag{6.28}$$

Given the contrast sources $\vec{w}_t(\vec{r})$ and the numerical background wavenumber k_n^2, the inverse of this operator evaluates scattered field values in Ω. To solve inverse scattering problems for the electrical properties of the OI, field values are required on the measurement surface $\mathcal{S}$ where the receivers are located and inside the imaging domain $\mathcal{D}$. In order to obtain these values, we introduce two operators, $\vec{\mathcal{M}}_s$ which takes $\vec{E}_t^{sct}$ in Ω to the receiver points, and the imaging domain operator $\vec{\mathcal{M}}_D$ which provides the field values in the imaging domain $\mathcal{D}$. These operators, which contain

the inverse FEM operator $\mathcal{L}$ derived in [32], make up the FEM-CSI functional given in Equation 1.3.

Appendix C: Tumour Detection Using Contrast Agents and FEM-CSI

The well-known study by Lazebnik *et al.*, which characterized the ultra-wideband dielectric properties of excised breast tissue, revealed that the difference in permittivity between a malignant carcinoma and normal fibroglandular tissue is intrinsically low [4]. This discovery triggered investigations into the use of contrast agents in MWI [51] [52] [53]. The conceivable utility of contrast agents creates a unique way to use prior information in the FEM-CSI algorithm to detect breast tumours. This method is described in the following sections.

Phantoms

Phantoms were obtained from the University of Wisconsin breast phantom repository, which is a collection of MRI data of breasts with different classifications. The data are divided into classes one through four, where the class refers to the amount of fibroglandular tissue found in the breast. Class One is a breast that contains mostly adipose tissue, Class Two contains scattered fibroglandular tissue, Class Three contains heterogeneously dense fibroglandular tissue, and Class Four is very dense. The repository assigns to the breast phantoms the microwave dielectric properties reported in [4].

The phantoms are interpolated on to an FEM mesh and two circular tumours are added. These tumours have an initial dielectric value of $\epsilon = 59.97 - j19.82$ [4] and a radius of $r = 0.5$ cm. A low loss immersion medium with $\epsilon = 23.0 - j1.13$ is

used. The addition of a contrast agent is simulated by increasing the permittivity value of the tumours. In the conference paper, we conducted a theoretical study in which the permittivity was raised by 15%. However, we have since performed further investigations for realistic contrast agents that have been approved for clinical use. We have also examined the potential to image magnetic contrast agents.

Detecting Permittivity Changes with Prior Information

Forward data were collected from the initial phantom using a finite element forward solver. We then used the FEM-CSI algorithm to invert the data using no prior information other than upper and lower bounds of the known tissues. The result was a blind reconstruction of the breast, which typically does not contain any useful diagnostic information. The use of a contrast agent was simulated by increasing or decreasing the permittivity of the tumours. Forward data were collected from the phantom with the contrast agent, and the FEM-CSI algorithm was used to reconstruct the image of the breast. In this case, the initial blind reconstruction was used as prior information in the form of an inhomogeneous background. This method is demonstrated in Figure 6.1.

The difference between the two reconstructions is so small that it is not observable by in the permittivity images by eye. In order to detect the location of the tumours, we must look at the contrast $\chi(\vec{r})$, which was defined in Eq. 1.2. The image of the contrast shows that at the location of the tumours. While the contrast reconstruction does not reach the actual known contrast value, the accuracy in location demonstrates a successful tumour detection.

A similar procedure was followed to simulate the use of a magnetic contrast agent.

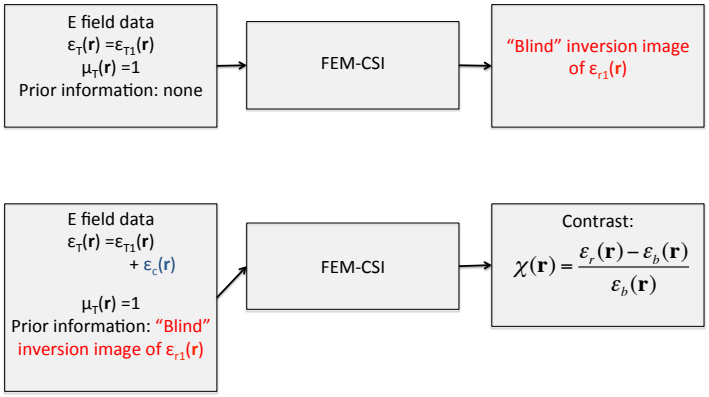

Figure 6.1: Flowchart describing contrast agent imaging using FEM-CSI.

When forward data were collected with a contrast agent present, the change was applied to the permeability of the tumours while the permittivity remained unchanged. The FEM-CSI algorithm was unable to directly solve for magnetic contrasts. However a change in the permeability of the tumours presents itself as a change in permittivity in the reconstruction, and the tumours were still detectable. This method is demonstrated in Figure 6.2.

Results and Conclusions

Figure 6.4 shows an initial test case that used a 15% increase for both a realistic class two breast phantom and a forearm phantom (a biological test case from our earlier study). Reconstructions from both phantoms show detectable tumours in the final contrast image.

Figure 6.4 shows a successful tumour detection for Class Two and Class Three

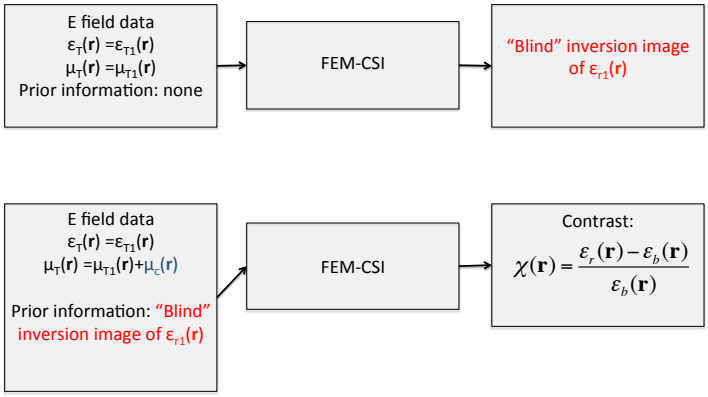

Figure 6.2: Flowchart describing magnetic contrast agent imaging using FEM-CSI.

breasts using carbon nanotubes (+22% in permittivity) as the contrast agent. Figure 6.4 a-d also shows a detection for a Class Four breast, although the algorithm has difficulty detecting the upper tumour, likely because it is imbedded in a patch of dense fibroglandular tissue. Figure 6.4 e-f shows contrast reconstructions using micro bubbles (−30% in permittivity) and g-h shows the reconstruction for a change in permeability from $\mu = 1$ to $\mu = 2$. Both of these contrast agents produce a reconstruction that contain artifacts, and it may be difficult to extract useful diagnostic information from them. Note that the magnetic case uses an unrealistically high permeability and was intended to test our ability to detect magnetic contrasts.

More realistic scenarios are currently being tested in the EIL by Mr. Cameron Kaye, who is investigating the use of magnetic nanoparticles as contrast agents in MWT. A high-order 2D inversion code that can simultaneously reconstruct electric and magnetic contrasts has been developed, as have algorithmic techniques for detecting the very small permeability changes introduced by the nanoparticles.

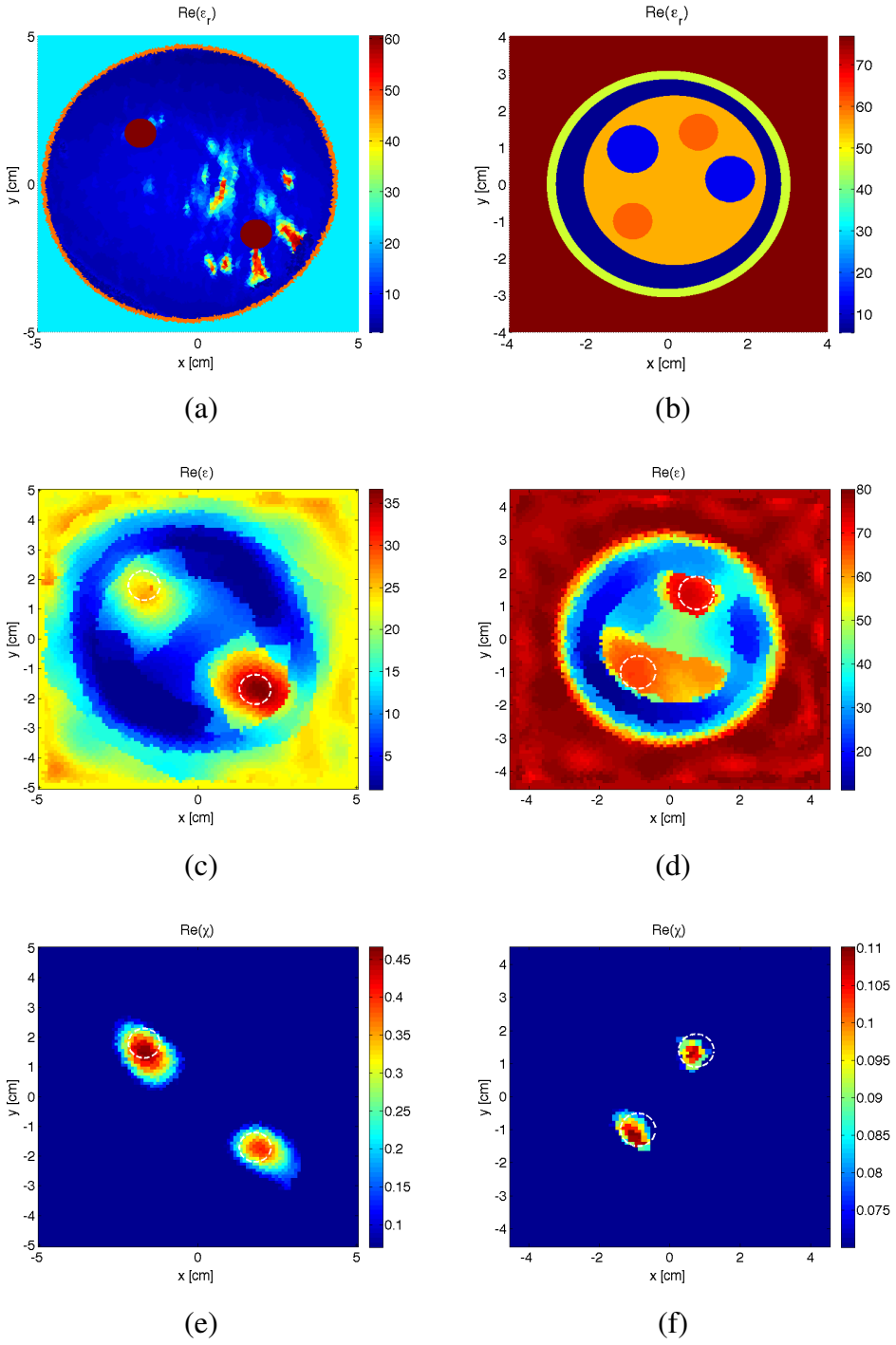

Figure 6.3: (a,c,e) Class One breast phantom, permittivity and contrast using +15% increase, and (b,d,f) forearm phantom, permittivity and contrast using +15% increase.

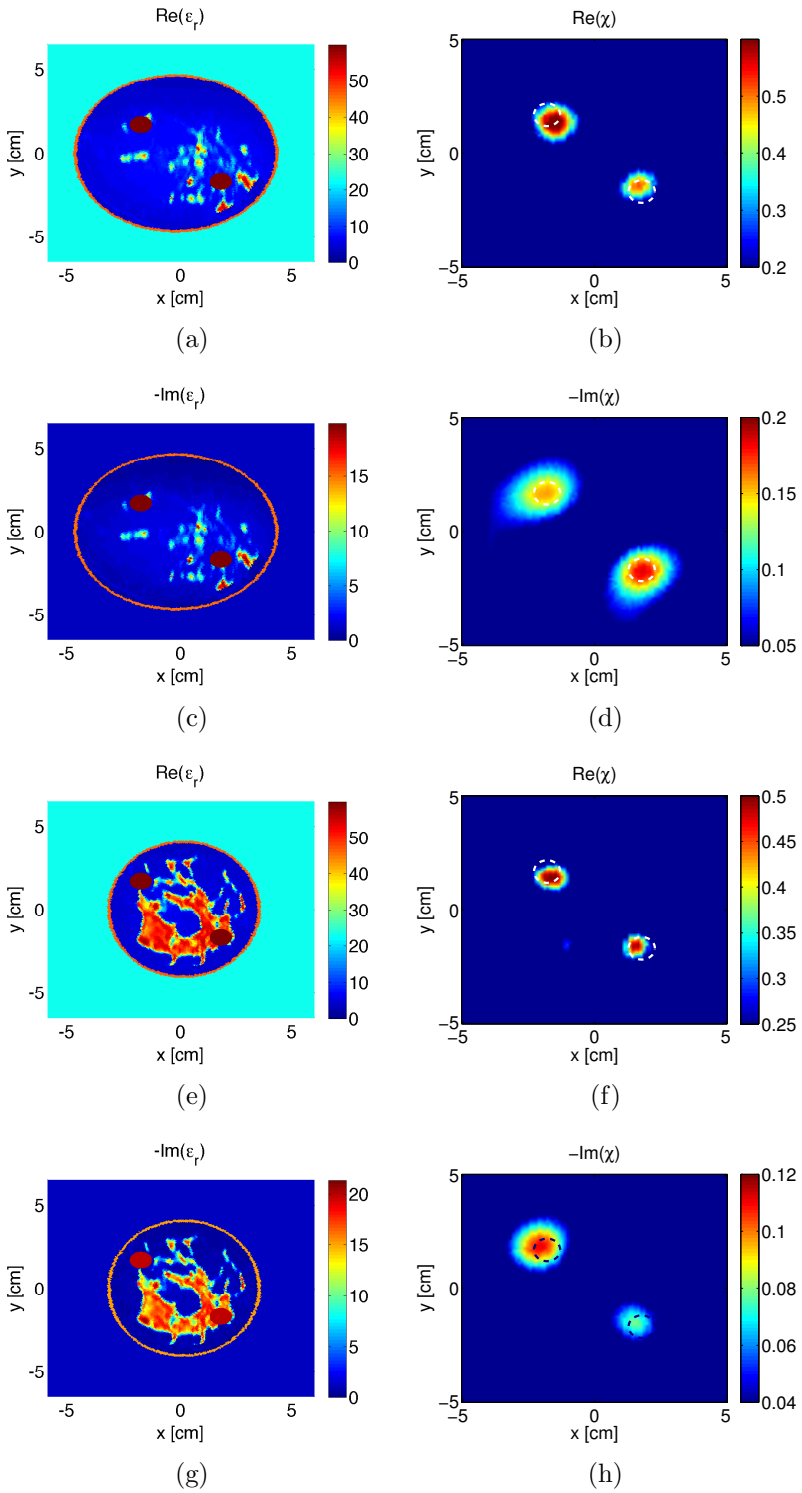

Figure 6.4: (a,b,c,d) Class Two breast phantom and reconstruction using carbon nanotubes, and (e,f,g,h) class three breast phantom and reconstruction using carbon nanotubes.

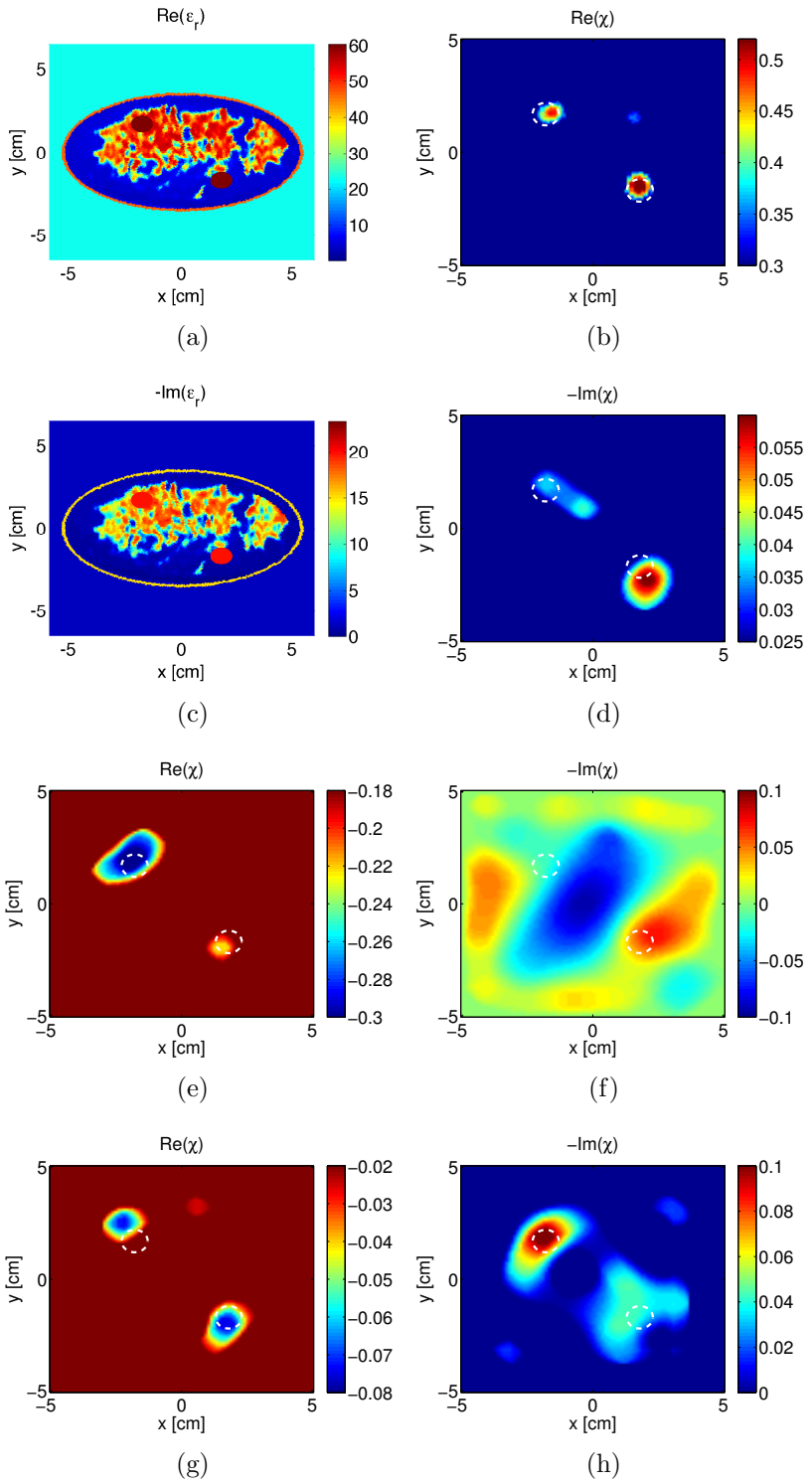

Figure 6.5: (a,b,c,d) Class Four breast phantom and reconstruction using carbon nanotubes, (e,f) reconstruction using micro bubbles, and (g,h) reconstruction using magnetic contrast agent.

References

[1] C. Gabriel, S. Gabriel, and E. Corthout, "The dielectric properties of biological tissues: III. Parametric models for the dielectric spectrum of tissues," *Physics in Medicine and Biology*, vol. 41, no. 11, pp. 2271–2294, Nov 2000.

[2] P. M. Meaney, M. W. Fanning, T. Raynolds, C. J. Fox, Q. Fang, C. A. Kogel, S. P. Poplack, and K. D. Paulsen, "Initial clinical experience with microwave breast imaging in women with normal mammography," *Academic Radiology*, vol. 14, no. 2, pp. 207–218, 2007.

[3] S. P. Poplack, T. D. Tosteson, W. A. Wells, B. W. Pogue, P. M. Meaney, A. Hartov, C. A. Kogel, S. K. Soho, J. J. Gibson, and K. D. Paulsen, "Electromagnetic breast imaging: Results of a pilot study in women with abnormal mammograms," *Radiology*, vol. 243, no. 2, pp. 350–359, 2007.

[4] M. Lazebnik, D. Popovic, L. McCartney, C. B. Watkins, M. J. Lindstrom, J. Harter, S. Sewall, T. Ogilvie, A. Magliocco, T. M. Breslin *et al.*, "A large-scale study of the ultrawideband microwave dielectric properties of normal, benign and malignant breast tissues obtained from cancer surgeries," *Physics in Medicine and Biology*, vol. 52, no. 20, p. 6093, 2007.

[5] E. C. Fear, X. Li, S. C. Hagness, and M. A. Stuchly, "Confocal microwave imaging

for breast cancer detection: Localization of tumors in three dimensions," *IEEE Transactions on Biomedical Engineering*, vol. 49, no. 8, pp. 812–822, 2002.

[6] S. C. Hagness, A. Taflove, and J. E. Bridges, "Fdtd modeling of a coherent-addition antenna array for early-stage detection of breast cancer," in *Antennas and Propagation Society International Symposium, 1998. IEEE*, vol. 2. IEEE, 1998, pp. 1220–1223.

[7] N. K. Nikolova, "Microwave imaging for breast cancer," *Microwave Magazine, IEEE*, vol. 12, no. 7, pp. 78–94, 2011.

[8] A. Fouda and F. Teixeira, "Ultra-wideband microwave imaging of breast cancer tumors via bayesian inverse scattering," *Journal of Applied Physics*, vol. 115, no. 6, p. 064701, 2014.

[9] E. Bond, X. Li, S. Hagness, and B. Van Veen, "Microwave imaging via space-time beamforming for early detection of breast cancer," *Antennas and Propagation, IEEE Transactions on*, vol. 51, no. 8, pp. 1690–1705, 2003.

[10] H. B. Lim, N. T. T. Nhung, E.-P. Li, and N. D. Thang, "Confocal microwave imaging for breast cancer detection: Delay-multiply-and-sum image reconstruction algorithm," *IEEE Transactions on Biomedical Engineering*, vol. 55, no. 6, pp. 1697–1704, 2008.

[11] X. Li, E. J. Bond, B. D. Van Veen, and S. C. Hagness, "An overview of ultra-wideband microwave imaging via space-time beamforming for early-stage breast-cancer detection," *IEEE Antennas and Propagation Magazine*, vol. 47, no. 1, pp. 19–34, 2005.

[12] G. N. Bindu, S. J. Abraham, A. Lonappan, V. Thomas, C. K. Aanandan, and K. Mathew, "Active microwave imaging for breast cancer detection," *Progress In Electromagnetics Research*, vol. 58, pp. 149–169, 2006.

[13] T. Henriksson, N. Joachimowicz, C. Conessa, and J.-C. Bolomey, "Quantitative microwave imaging for breast cancer detection using a planar 2.45 ghz system," *IEEE Transactions on Instrumentation and Measurement*, vol. 59, no. 10, pp. 2691–2699, 2010.

[14] T. Rubæk, O. S. Kim, and P. Meincke, "Computational validation of a 3-d microwave imaging system for breast-cancer screening," *IEEE Transactions on Antennas and Propagation*, vol. 57, no. 7, pp. 2105–2115, 2009.

[15] M. Klemm, I. Craddock, J. Leendertz, A. Preece, and R. Benjamin, "Experimental and clinical results of breast cancer detection using uwb microwave radar," in *2008 IEEE Antennas and Propagation Society International Symposium*. IEEE, 2008, pp. 1–4.

[16] M. Donelli, I. J. Craddock, D. Gibbins, and M. Sarafianou, "A three-dimensional time domain microwave imaging method for breast cancer detection based on an evolutionary algorithm," *Progress In Electromagnetics Research M*, vol. 18, pp. 179–195, 2011.

[17] A. E. Bulyshev, S. Y. Semenov, A. E. Souvorov, R. H. Svenson, A. G. Nazarov, Y. E. Sizov, and G. P. Tatsis, "Computational modeling of three-dimensional microwave tomography of breast cancer," *IEEE Transactions on Biomedical Engineering*, vol. 48, no. 9, pp. 1053–1056, 2001.

[18] A. Ashtari, S. Noghanian, A. Sabouni, J. Aronsson, G. Thomas, and S. Pisto-

rius, "Using a priori information for regularization in breast microwave image reconstruction," *Biomedical Engineering, IEEE Transactions on*, vol. 57, no. 9, pp. 2197–2208, 2010.

[19] S. Semenov, J. Kellam, B. Nair, T. Williams, M. Quinn, Y. Sizov, A. Nazarov, and A. Pavlovsky, "Microwave tomography of extremities: 2. functional fused imaging of flow reduction and simulated compartment syndrome," *Physics in Medicine and Biology*, vol. 56, p. 2019, 2011.

[20] S. Y. Semenov and D. R. Corfield, "Microwave tomography for brain imaging: Feasibility assessment for stroke detection," *International and Propagation*, vol. 2008, 2008.

[21] S. Egot-Lemaire, J. Pijanka, J. Sulé-Suso, and S. Semenov, "Dielectric spectroscopy of normal and malignant human lung cells at ultra-high frequencies," *Physics in medicine and biology*, vol. 54, no. 8, p. 2341, 2009.

[22] S. Semenov, V. Posukh, A. Bulyshev, T. Williams, Y. Sizov, P. Repin, A. Souvorov, and A. Nazarov, "Microwave tomographic imaging of the heart in intact swine," *Journal of Electromagnetic Waves and Applications*, vol. 20, no. 7, pp. 873–890, 2006.

[23] A. Zakaria, C. Gilmore, and J. LoVetri, "Finite-element contrast source inversion method for microwave imaging," *Inverse Problems*, vol. 26, no. 11, p. 115010, 2010.

[24] C. Geuzaine and J.-F. J.-F. Remacle, "GMSH: A 3-D finite element mesh generator with built-in pre- and post-processing facilities," *International Journal for Numerical Methods in Engineering*, vol. 79, p. 13091331, 2009.

[25] E. Fear, J. Bourqui, C. Curtis, D. Mew, B. Docktor, and C. Romano, "Microwave breast imaging with a monostatic radar-based system: A study of application to patients," *IEEE Transactions on Microwave Theory and Techniques*.

[26] T. M. Grzegorczyk, P. M. Meaney, P. A. Kaufman, R. M. di Florio-Alexander, and K. D. Paulsen, "Fast 3-d tomographic microwave imaging for breast cancer detection," *IEEE Transactions on Medical Imaging*, vol. 31, no. 8, pp. 1584–1592, 2012.

[27] J. D. Shea, P. Kosmas, S. C. Hagness, and B. D. Van Veen, "Three-dimensional microwave imaging of realistic numerical breast phantoms via a multiple-frequency inverse scattering technique," *Medical Physics*, vol. 37, p. 4210, 2010.

[28] Y. Wang and W. Chew, "An iterative solution of the two-dimensional electromagnetic inverse scattering problem," *International Journal of Imaging Systems and Technology*, vol. 1, no. 1, pp. 100–108, 1989.

[29] W. C. Chew, *Waves and fields in inhomogeneous media*. IEEE press New York, 1995, vol. 522.

[30] W. C. Chew and Y. M. Wang, "Reconstruction of two-dimensional permittivity distribution using the distorted Born iterative method," *Medical Imaging, IEEE Transactions on*, vol. 9, no. 2, pp. 218–225, 1990.

[31] A. Zakaria and J. LoVetri, "Application of multiplicative regularization to the finite-element contrast source inversion method," *IEEE Transactions on Antennas and Propagation*, vol. 59, no. 9, pp. 3495 –3498, Sept 2011.

[32] A. Zakaria, "The finite-element contrast source inversion method for microwave

imaging applications," Ph.D. dissertation, University of Manitoba, March 2012. [Online]. Available: http://hdl.handle.net/1993/5213

[33] A. Golnabi, P. Meaney, S. Geimer, and K. Paulsen, "Microwave imaging of the breast with incorporated structural information," in *Proceedings of SPIE*, vol. 7626, 2010, p. 76260P.

[34] C. Gilmore, A. Zakaria, S. Pistorius, and J. LoVetri, "Microwave imaging of human forearms: pilot study and image enhancement," *Journal of Biomedical Imaging*, vol. 2013, p. 19, 2013.

[35] A. Fhager and M. Persson, "Using a priori data to improve the reconstruction of small objects in microwave tomography," *IEEE Transactions on Microwave Theory and Techniques*, vol. 55, no. 11, pp. 2454–2462, 2007.

[36] A. Wirgin, "The inverse crime," *Arxiv preprint math-ph/0401050*, 2004.

[37] A. Zakaria, A. Baran, and J. LoVetri, "Estimation and use of prior information in fem-csi for biomedical microwave tomography," *Antennas and Wireless Propagation Letters*, 2012.

[38] A. Baran, D. J. Kurrant, A. Zakaria, E. C. Fear, and J. LoVetri, "Breast imaging using microwave tomography with radar-based tissue-regions estimation," *Progress In Electromagnetics Research*, vol. 149, pp. 161–171, 2014.

[39] S. Kirkpatrick, "Optimization by simulated annealing: Quantitative studies," *Journal of statistical physics*, vol. 34, no. 5-6, pp. 975–986, 1984.

[40] D. Bertsimas and J. Tsitsiklis, "Simulated annealing," *Statistical Science*, pp. 10–15, 1993.

[41] C. Gilmore, A. Zakaria, S. Pistorius, and J. LoVetri, "Microwave imaging of human forearms: Pilot study and image enhancement," *Journal of Biomedical Imaging*, vol. 2013, p. 19, 2013.

[42] D. Kurrant and E. Fear, "Regional estimation of the dielectric properties of inhomogeneous objects using near-field reflection data," *Inverse Problems*, vol. 28, no. 7, p. 075001, 2012. [Online]. Available: http://stacks.iop.org/0266-5611/28/i=7/a=075001

[43] E. Zastrow, S. Davis, M. Lazebnik, F. Kelcz, B. Van Veen, and S. Hagness, "Development of anatomically realistic numerical breast phantoms with accurate dielectric properties for modeling microwave interactions with the human breast," *Biomedical Engineering, IEEE Transactions on*, vol. 55, no. 12, pp. 2792–2800, Dec 2008.

[44] S. Y. Semenov and D. R. Corfield, "Microwave tomography for brain imaging: Feasibility assessment for stroke detection," *International Journal of Antennas and Propagation*, vol. 2008, p. 8, 2008.

[45] M. Asefi, G. Faucher, and J. LoVetri, "Surface-current measurements as data for electromagnetic imaging within metallic enclosures," *IEEE Transactions on Microwave Theory and Techniques*, Accepted April 2016.

[46] C. Gilmore, A. Zakaria, S. Pistorius, and J. LoVetri, "A study of matching fluids loss in a biomedical microwave tomography system," *submitted to Medical Physics, AAPM*, 2012.

[47] J. Sill and E. Fear, "Tissue sensing adaptive radar for breast cancer detection-

experimental investigation of simple tumor models," *Microwave Theory and Techniques, IEEE Transactions on*, vol. 53, no. 11, pp. 3312–3319, 2005.

[48] W. Chew and J. Lin, "A frequency-hopping approach for microwave imaging of large inhomogeneous bodies," *Microwave and Guided Wave Letters, IEEE*, vol. 5, no. 12, pp. 439–441, 1995.

[49] J. Jin, *The Finite Element Method in Electromagnetics*. New York: John Wiley and Sons, 2002.

[50] C. Gabriel, "Compilation of the dielectric properties of body tissues at rf and microwave frequencies." DTIC Document, Tech. Rep., 1996.

[51] A. Mashal, J. H. Booske, and S. C. Hagness, "Toward contrast-enhanced microwave-induced thermoacoustic imaging of breast cancer: An experimental study of the effects of microbubbles on simple thermoacoustic targets," *Physics in medicine and biology*, vol. 54, no. 3, p. 641, 2009.

[52] A. Mashal, B. Sitharaman, X. Li, P. K. Avti, A. V. Sahakian, J. H. Booske, and S. C. Hagness, "Toward carbon-nanotube-based theranostic agents for microwave detection and treatment of breast cancer: enhanced dielectric and heating response of tissue-mimicking materials," *Biomedical Engineering, IEEE Transactions on*, vol. 57, no. 8, pp. 1831–1834, 2010.

[53] G. Bellizzi, O. M. Bucci, and I. Catapano, "Microwave cancer imaging exploiting magnetic nanoparticles as contrast agent," *Biomedical Engineering, IEEE Transactions on*, vol. 58, no. 9, pp. 2528–2536, 2011.